

# Development of an instrumented mooring system for VFFS model testing

Focused on the sensor configuration and calibration procedure

S.H.M. van der Voort

Master Thesis  
MT.21.007.M.





# Development of an instrumented mooring system for VFFS model testing

**Focused on the sensor configuration and  
calibration procedure**

by

S.H.M. van der Voort

to obtain the degree of Master of Science  
at the Delft University of Technology,

Student number: 4444736  
Project duration: November 16, 2020 – December 3, 2021  
Thesis committee: Dr. ir. I. Akkerman, TU Delft, chairman  
Dr.-Ing. S. Schreier, TU Delft, daily supervisor



# Preface

About a year ago, I started my graduation project at the TU Delft. I am proud to present you this report as the final result. In the past year, I have worked hard to develop a new sensor for the towing tank at the TU Delft. I hope this sensor can contribute to much new research into very flexible floating structures to develop these type of structures. During my thesis, I gained a lot of knowledge about designing, fabricating and testing of a new sensor. Of course, not everything went smoothly, mainly during the first part of my thesis when I had to work from home quite some time. However, I really enjoyed testing and analysing the results of the sensor.

My thesis would not have been possible without all the help I received. First of all, a special thanks to my supervisor Sebastian for the guidance and all the discussion we had about my thesis. He was always available to think along when I needed it, and advised me not only with analytical feedback but also with the practical feedback. Furthermore, I would like to thank Peter and Jasper for thinking along with the design of the sensor and realising it. Moreover, I want to thank Pascal for fabricating all the parts that I needed for my setups. Also, thanks to Ido Akkerman for providing feedback about my thesis in the final stage. Finally, I would like to thank the BEP group that obtained measurement data for my preliminary approximation of the mooring forces.

For obtaining this report, I also want to thank my family and friends. Thomas, my parents and sisters, thank you for hearing all my (technical) challenges. And a special thanks to Thomas for proof-reading my thesis!

Enjoy reading!

*S.H.M. van der Voort  
Delft, December 2021*



# Abstract

Floating structures have developed significantly in recent years. As the world's population keeps on rising, land is becoming scarce and innovative solutions for efficient use of the earth's surface are being developed. The surface of the earth is covered for 70 percent by oceans and use of this water surface will contribute to ease the scarcity of land. Therefore in recent years, floating structures covering large areas have been developed, also called flexible floating structures.

Research into flexible floating structures is still limited, and to better understand these type of structures, new research is required. In this project the focus is set on the mooring system very flexible floating structures (VFFS). The interplay between the structure response and the mooring system of VFFS seems to function differently than for traditional 'rigid' structures such as vessels.

At the TU Delft, two towing tanks can be used to investigate the mooring system of VFFS, however first a reliable measuring system is required that is able to examine a specific part of the mooring system. For this project, we are interested in the mooring forces. Conventional setups that measure the mooring forces consist of large instruments, as these instruments only have a small effect on their investigated structure (vessels). VFFS typically have a small bending stiffness. Therefore, the response of VFFS is dominated by elastic deformations and differs from conventional rigid structures. For VFFS, these type of instruments will have a large effect on the structure motions and thus these conventional setups cannot be used. Therefore, a new measuring system is required that is able to conduct small scale experiments with VFFS.

To achieve a working system the following objective is formulated: *'Develop an instrumented mooring system for VFFS at model scale for the towing tank at the TU Delft and determine its accuracy'*.

In order to achieve the objective, a new concept is developed in this project. This concept resulted from an extensive concept development where all functions of the system were analyzed. With the use of a Morphological Chart and a Multi Criteria Analysis the best concept was selected. For this concept, it was determined that the focus should be on the sensor configuration and calibration procedure.

First, the optimal sensor configuration of the concept was specified by analysing the working principle of the concept. Second, the calibration procedure was further analyzed. From this analysis, three calibration procedures were developed: the single sensor calibration matrix, the full fixed calibration matrix and the full rotated calibration matrix. From literature and theory, it was not possible to determine in advance what calibration procedure should be selected, and therefore the performance of the procedures were verified with experiments. All calibration procedures were executed, whereafter the performance of the different procedures were compared. The two main considerations for the comparison were the accuracy and the usability of the procedures. After performing the comparison, the main conclusion was that the full upright calibration procedure is the optimal procedure.

To verify the concept under realistic conditions, an example application was performed in the towing tank No.1 at the TU Delft. By doing this, the concept has proven to be suitable to measure the mooring force and transform them into usable data.

In this project a new concept was developed into a working system. This system forms an excellent base for extensive research into the mooring system of VFFS, and is a good addition to the measurement instruments for the towing tank at the TU Delft. It is concluded that the system is able to measure the mooring forces and the direction. The accuracy of the system still has to be improved, and with additional research the working concept can be further developed.



# Contents

<b>1</b>	<b>Introduction</b>	<b>1</b>
1.1	Flexible floating structures . . . . .	1
1.2	Research development. . . . .	3
1.2.1	Design requirements . . . . .	4
1.2.2	Ethical importance . . . . .	4
1.3	Report structure . . . . .	4
<b>2</b>	<b>Background</b>	<b>6</b>
2.1	State of the Art literature . . . . .	6
2.1.1	Coupled mooring analysis . . . . .	6
2.1.2	Uncoupled mooring analysis. . . . .	7
2.2	Mooring force estimation . . . . .	8
<b>3</b>	<b>Concept development</b>	<b>11</b>
3.1	Morphological chart . . . . .	11
3.2	Multi Criteria Analysis . . . . .	12
3.3	Sensitivity analysis . . . . .	14
<b>4</b>	<b>Problem analysis</b>	<b>18</b>
4.1	Calibration theory. . . . .	18
4.2	Research question . . . . .	19
<b>5</b>	<b>Development of test setup</b>	<b>20</b>
5.1	Axial force sensor type . . . . .	20
5.2	Sensor frame . . . . .	20
5.2.1	Frame dimensions . . . . .	21
5.2.2	Axis system . . . . .	22
5.2.3	Sensor position . . . . .	23
<b>6</b>	<b>Calibration</b>	<b>25</b>
6.1	Single sensor calibration . . . . .	25
6.1.1	Theory single variable regression analysis . . . . .	25
6.1.2	Calibration setup . . . . .	29
6.1.3	Calibration experiments . . . . .	30
6.1.4	Results . . . . .	32
6.2	Frame calibration upright position . . . . .	36
6.2.1	Theory multi variable sensor. . . . .	36
6.2.2	Extended theory multi variable. . . . .	36
6.2.3	Calibration setup frame . . . . .	37
6.2.4	Calibration experiments . . . . .	38
6.2.5	Verification of calculation calibration matrix . . . . .	40
6.2.6	Results . . . . .	40
6.3	Comparison calibration matrices upright position . . . . .	44
6.3.1	Theoretical calibration matrix . . . . .	44
6.3.2	Single sensor calibration matrix . . . . .	46
6.3.3	Full upright calibration matrix . . . . .	46
6.3.4	Calibration matrices comparison upright position . . . . .	46
6.4	Frame calibration rotated position . . . . .	50
6.4.1	Theory rotation matrix . . . . .	50
6.4.2	Calibration setup rotated frame . . . . .	51
6.4.3	Calibration experiments . . . . .	52
6.4.4	Results . . . . .	53

6.5	Comparison calibration matrices rotated position . . . . .	56
6.5.1	Rotation matrix verification . . . . .	56
6.5.2	Calibration matrices comparison rotated position . . . . .	57
6.6	Discussion calibration matrix. . . . .	60
6.6.1	Pulley friction . . . . .	60
6.7	Conclusions calibration matrix . . . . .	63
<b>7</b>	<b>Example application</b>	<b>64</b>
7.1	Experimental procedure . . . . .	64
7.2	Experimental setup . . . . .	65
7.3	Experiments . . . . .	67
7.4	Results . . . . .	69
7.4.1	Rotation matrix . . . . .	69
7.4.2	Pretension . . . . .	69
7.4.3	Mooring force . . . . .	70
7.4.4	Discussion and Conclusions of example application . . . . .	73
<b>8</b>	<b>Discussion</b>	<b>74</b>
<b>9</b>	<b>Conclusions</b>	<b>76</b>
<b>10</b>	<b>Future work and improvements</b>	<b>78</b>
	<b>Bibliography</b>	<b>79</b>
<b>A</b>	<b>Concept development</b>	<b>82</b>
A.1	Morphological chart . . . . .	82
A.2	MCA. . . . .	83
A.2.1	Weight factors . . . . .	83
A.2.2	MCA graded . . . . .	84
<b>B</b>	<b>Calibration example</b>	<b>85</b>
<b>C</b>	<b>Test setup details</b>	<b>87</b>
C.1	Sensor frame drawings. . . . .	88
<b>D</b>	<b>Results</b>	<b>92</b>
D.1	Regression analysis single sensor 1 . . . . .	92
D.2	Regression analysis single sensor 2 . . . . .	95
D.3	Regression analysis single sensor 3 . . . . .	98
<b>E</b>	<b>Pulley system influence</b>	<b>101</b>
<b>F</b>	<b>Calculation flow diagram</b>	<b>104</b>
F.1	Calculation flow diagram of calibration experiments . . . . .	104
F.2	Calculation flow diagram of example application experiments . . . . .	105
<b>G</b>	<b>Data logbook &amp; Calibration scheme</b>	<b>106</b>

# Introduction

## 1.1. Flexible floating structures

Offshore floating structures have developed significantly in recent years. As the world's population keeps on rising, land is becoming scarce and innovative solutions for efficient use of the earth's surface are being developed. The surface of the earth is covered for 70 percent by oceans and use of this water surface will contribute to ease the scarcity of land. In recent years, floating structures covering large areas have been developed, these type of structures are called flexible floating structures. An example of one of the most famous flexible floating structure concept is the floating airport of Tokyo [16], figure 1.1.



Figure 1.1: Very large floating structure, a prototype of a floating airport in Tokyo [16]

Rigid floating structures (e.g. vessels) and flexible floating structures can be distinguished in terms of global response. In the article of Suzuki et al. [29] a proposed distinction is made by a characteristic length  $\lambda_c$  (Eq. 1.1), with the bending stiffness of a beam  $EI$  and the hydrostatic stiffness  $k_c$  of the support.

$$\lambda_c = 2\pi \left( \frac{EI}{k_c} \right)^{\frac{1}{4}} \quad (1.1)$$

If the length of the structure is smaller than the characteristic length  $\lambda_c$ , the response is predominated by rigid-body motions. Whereas the response of structures with a total length larger than the characteristic length is dominated by elastic deformations, see figure 1.2. Flexible floating structures typically have a small bending stiffness, resulting in a small characteristic length. Therefore, the response of flexible floating structures is dominated by elastic deformations and differs from conventional rigid structures. Flexible floating structures can be further divided by very large floating structures (VLFS) and very flexible floating structures (VFFS). VLFS have a flexible response on the global scale whereas VFFS also have flexible response on the local scale.

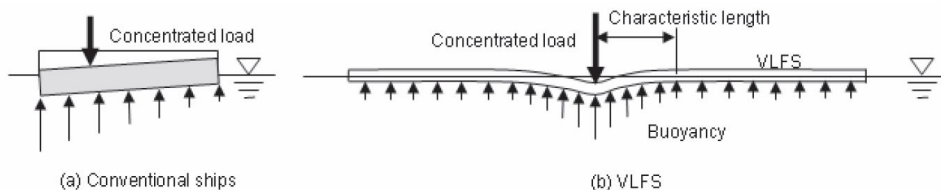


Figure 1.2: Global response of conventional structure and VLFS and VFFS, [29]

An important aspect of VFFS is the mooring system, that ensures the floating structure is kept in position. The mooring system for VFFS can deform the connection area of the structure with the mooring line. VFFS are designed with a small total height to increase the flexibility, and this small height causes the structures to float with minimal height above the water surface. If for example, a flexible floating structure at full scale rises 100mm above the water surface, a surface of  $10m^2$  can only withstand 1tonne of vertical load using the Archimedes' principle, before it fully submerges under the water surface. Just the mooring cable itself can easily create 1tonne of vertical loading to the structure, and therefore the effect of structure submerging can have a major influence. A large part of the structure can easily be pulled below the water surface at the position of the mooring line and water overwashing effects can worsen this effect. A floating structure which is flooded at a large area can cause unpredictable hydrodynamic forces and structure responses. As the mooring system is an important parameter of a VFFS, this interaction should be well understood.

To analyze the mooring system of VFFS and its interaction with the structure response, preferably well known experiments are used. For conventional floating structures such as semi-submersibles and spar structures, the interaction between the mooring system and the structure response is of less importance and can be uncoupled for experimental investigations, [18]. In this way, the structure response and the mooring analysis can be examined in separate experiments. In the experimental setups described in [15], [3], [2] and [19], catenary mooring systems are tested without the floating structure as they are uncoupled. Uncoupled analysis for conventional floating structures can be used, as the structure responses in the low frequency range are investigated. For conventional structures, second order wave forces are predominate, these wave forces are caused by wave groups which have a lower frequency as normal waves [32]. Additionally, the damping effects of the mooring system and risers can be neglected for these type of structures [18]. For VFFS, these assumptions can be questioned to be valid as VFFS can have high frequency motions as first order wave forces are predominate. These are caused by normal waves with a frequency of around 0.05Hz - 0.2Hz. Furthermore, VFFS do not have large additional buoyancy, therefore damping effects can have significant influences. As VFFS do not comply to all assumptions, this method cannot be used and a different method should be investigated. To see what the current status is of the experimental investigations of flexible floating structures, several researches are listed.

In literature different experiments are performed investigating flexible floating structures. Most of these articles are focused on VLFS which have a large freeboard compared to VFFS. For VLFS, no large structure deformations are observed due to the measurement instruments.

An example of research investigating a flexible floating structure is from Chen et al. [6]. In this research two flexible structures are simulated with a numerical model. The first structure consists of 12 interconnected floaters and the second structure is a flexible beam. Both the structures have a total length of 300m, width 60m, height 2m and draught of 0.5m. The numerical model assumes ideal fluids and the behaviour is modelled with velocity potentials. With this model the hydro-elastic responses of the structures are determined in the frequency domain. The article shows the importance of hydro-elasticity for analysing flexible floating structures. In this article, no further information is given about the mooring configuration, however it can be questioned what the influence of the mooring system is on the hydro-elastic response of the structure.

The influence of the mooring system on the structure response of a flexible floating structure is analyzed by Tajali and Shafieefar [30]. In this article a floating multi-body pier of 120m by 7m with a height of 1.8m and a draught of 1.2m with some arrangements of several pontoons is analyzed. The objective is to analyze the structure response, and this is investigated in the frequency domain. The main result of this article is a computational method to assess the hydrodynamic effect on a multi-body structure. Furthermore, it was concluded during the analysis that the mooring system affects the surge and sway motions and have less effect on the heave, pitch and roll motions. In this article only the heave, pitch and roll motions have been investigated, the effect of the mooring system on the structure response is therefore not further analyzed. However, this article shows the interaction between the structure response and the mooring system, and shows that this effect is even more significant for surge and sway motions.

Schreier and Jacobi [26] investigated the wave structure interaction of a VFFS. In an experimental setup, the motions of a VFFS (L 4.95m, B 1.02m, h 5mm) are recorded using digital image correlation. The structure is simply moored with long mooring lines connected at the waterline, to minimize mooring effects. The article concludes that for shorter waves a stronger hydroelastic interaction is observed.

The research of Ding et al. [10] investigated the internal forces of a multi-body flexible floating structure in an experimental setup. In this article, several semi-submersibles (L 0.6m, B 0.2m, h 0.02m) were connected in series as a chain-type floating platform, figure 1.3. With the connections between the semi-submersibles, independent rotations of the semi-submersibles are allowed. The complete assembly is moored with 4 mooring lines. These mooring lines consist of fishing lines and an extension spring. With this article the structural response of the complete assembly is determined with a numerical model and verified with the experimental tests. The authors conclude that the numerical and experimental results coincide well, therefore connector loads are calculated with the numerical model.

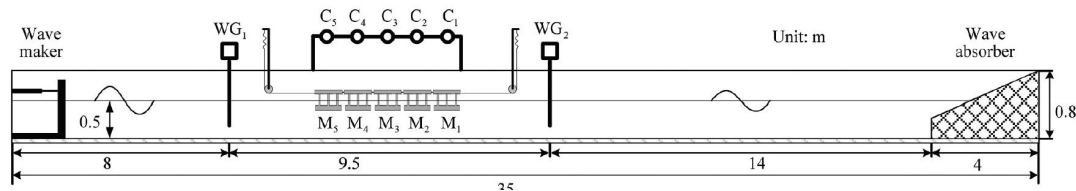


Figure 1.3: Side view of experimental setup of a chain-type floating platform in a wave flume, left the wave maker, right the wave absorber (beach) and in the middle the chain-type floating platform scale model consisting of 5 pontoons. Mooring lines above the water enables the platform to keep position. [10]

The loads on a flexible floating structure are further investigated by Trapani [31]. In this research several aspects of a VFFS consisting of PV-panels are analyzed. In chapter 3 of this article, the environmental loading conditions are examined. Wind, wave and current forces on the structure are estimated with a theoretical model including CFD (computational fluid dynamics) modelling. With this model a first approximation of the mooring force can be made. In section 2.2, this article is used to approximate the mooring force of flexible floating structures in a experimental setup.

Research described above gives an impression of the knowledge and experiments investigating flexible floating structures. In this research, the main focus is on the mooring system of flexible floating structures and the influence to the structure response. Although research has shown that the mooring system can have a significant effect on the structure response, there is still limited information about the actual influence of the mooring system. Therefore, more research is required to investigate this influence of the mooring system. Also, it was shown that the research described above is focused on VLFS. As these type of structures have a large freeboard, no significant impact of the instruments are observed. For VFFS, instruments most likely do a have significant influence.

## 1.2. Research development

To better understand the interplay between the structure response and the mooring system of very flexible floating structures new research is required. With new research the influence of the mooring system can be investigated and it can be determined if the following hypotheses are valid.

First of all, the mooring system for very flexible floating structures can deform the connection area of the structure with the mooring line. A floating structure which is flooded at a large area can cause unpredicted hydrodynamic forces and structure responses.

A second reason why the mooring system can have an effect on the structure response is that a mooring system can cause pretension in the flexible floating structure, whereby the flexible floating structure cannot follow the water surface freely and this can cause undesired structure responses.

To test these hypothesis and to obtain other data of flexible floating structures, first, a reliable measuring system is required able to measure mooring forces. Conventional setups that measure the mooring forces consist of large instruments, as these instruments only have a small effect on their investigated structures (vessels). For flexible floating structures, these type of large instruments will have large effect on the structure motions and thus these conventional setups cannot be used. Therefore, a new measuring system is required that is able to conduct small scale experiments with flexible floating structures. For this project the towing tank No. 1 at the TU Delft is available for designing a test setup that is able to measure mooring forces of flexible floating structures. In order to investigate small effects on the structure, it is necessary to have a setup that can measure forces with high accuracy. The setup should be able to measure small deviations of mooring forces to test all types of parameters such as

structure properties and wave conditions. This results in the following objective for this project:

***"Develop an instrumented mooring system for VFFS at model scale for the towing tank at the TU Delft and determine its accuracy".***

### 1.2.1. Design requirements

The system that will be developed should meet the following requirements:

- The system should be able to measure the mooring forces of a flexible floating structure in wave loading conditions. The mooring force should be known in all components, this means that the magnitude and the direction of the mooring force should be measured. With the mooring force known in all directions, it can be investigated how the different components evolve during wave loading conditions.
- The system should be able to measure the mooring force with a known accuracy. In the ITTC code [13] different classifications for the load cell accuracy are elaborated. For the system of this project it is assumed that a classification of 'precision' will be sufficient, as this implies an accuracy of around 0.1%FS - 0.3%FS. With this accuracy it is assumed that small deviations in the measurements, that should be visible, can be observed.
- The system should be able to test scale model flexible floating structures. As the system will be designed for the towing tank at the TU Delft, an approximation of the dimensions of the structures can be made. The system should be able to test flexible floating structures with a width up to 1m and a length up to 5m. The required measurement range of the force measurement system will be determined according this requirement in section 2.2.

### 1.2.2. Ethical importance

Designing an instrumented mooring system for flexible floating structures will contribute to the development of these type of structures. As mentioned before, flexible floating structures are getting more and more attention due to the growing problem of scarcity of land and flexible floating structures can help solve this problem. To ensure these type of structures can withstand the rough conditions of the open ocean and are safe to use, the structures should be validated. A new setup that is able to measure the mooring forces of flexible floating structures can serve as a basis for lots of new research into the mooring system of flexible floating structures. Researchers can use the test setup for experiments with different types of mooring systems and flexible floating structures and measure the mooring forces with high accuracy. It can also be combined with other experimental setups that can measure the motions of a flexible floating structure, e.g. the measurement device described in Schreier and Jacobi [26]. With this combination of measurement devices, it is possible to investigate the interaction between the motions and the mooring forces of a structure.

For researchers, it should be clear what they can expect of the setup and they should be able to check if the setup is suitable for their purpose. The setup should therefore be designed and tested to determine the usability and the limitations. Furthermore, researchers considering using the setup should have a clear overview of the calibrations and experiments that are required in order to achieve their experimental results. And most importantly, the setup should provide a robust and reliable system.

## 1.3. Report structure

To achieve a working design, the process is structured in chapters:

In chapter 2, background information about experiments and mooring force estimations are summarized. This information is later used for concept development and the detailed development of the system. Chapter 3 describes the concept development. Before the research questions are determined, a concept is selected. This concept is selected with the use of a morphological chart, which creates a range of possible concepts. The concepts are graded with a multi criteria analysis, in which the concepts are judged on how they match the criteria. In chapter 4, the selected concept in chapter 3 is further analyzed. In this chapter, a problem analysis is performed. In order to end up with a working design, several challenges need to be solved for this specific concept. This is combined in a set of

---

research questions. In chapter 5, the detailed design of the concept is elaborated. What materials, sensors and dimensions are used for the design. Chapter 6 describes the calibration procedure for the sensor. For each procedure it is explained what experiments are required and the results of the experiments are elaborated. Chapter 7 describes an example application of the sensor. With this example the performance of the sensor is tested in realistic conditions. The sensor frame is installed in the towing tank No. 1 at the TU Delft and standard wave conditions are applied.

# 2

## Background

This chapter elaborates on the background knowledge. The background knowledge is obtained from literature and a summary of this literature study is presented in this chapter. First, experimental setups that are developed for floating structures are discussed and their main conclusions and recommendations are elaborated. Secondly, the forces on flexible floating structures are estimated. To meet the accuracy requirement of the objective, it should be examined what forces can be expected. Finally, experimental uncertainties due to measuring procedures and instruments are presented. Performing measurements introduces uncertainties and this procedure to obtain the uncertainties is elaborated according to a standardized procedure.

### 2.1. State of the Art literature

The purpose of this thesis is to develop a new instrumented mooring system for flexible floating structures, since it is concluded in the introduction that conventional experimental setups are not suitable for testing flexible floating structures. These setups consist of large instruments that will significantly effect the flexible floating structure motions. However, experiments for the mooring systems of conventional 'rigid' floating structures have already been developed and these setups can provide relevant knowledge. Currently, more and more 'rigid' floating structures are installed at offshore location, such as, floating windturbines and FPSO's. Mooring systems for these kind of structures are tested and verified in small scale experiments. And as mentioned in the introduction, uncoupled experiments with only the mooring system of a construction are conducted. As these types of 'rigid' structures will have different structure responses, these experimental setups cannot be implemented immediately, however useful solutions in these setups can be adopted. In this section interesting experimental setups for floating structures are elaborated, first coupled experimental setups, and second uncoupled experimental setups.

#### 2.1.1. Coupled mooring analysis

In the articles of Loukogeorgaki et al. [17], Xu et al. [33], Peña et al. [22] and Dessi and Minna [9], small scale experimental setups of complete floating structures including the mooring system are evaluated. The article of Loukogeorgaki et al. [17], evaluates a moored floating breakwater. A total of three large pontoons (L 1m, W 0.2m, H 0.07m) are connected to each other and 8 mooring lines are used for fixation. The connections between the pontoons are equipped with strain gauges to measure the axial and shear forces. Two of the eight mooring lines are equipped with an axial waterproof load cell, these mooring lines are assumed to be most loaded during experiments. The goal of this article is to assess the structure response (connectors internal forces and mooring lines tensions) due to wave loading. Interesting conclusions of this article are the influence of the wave height, period and direction on the structure response. Additionally, it is mentioned that snap loads due to slack in mooring lines can cause high mooring loads. In this experimental setup no direction of the mooring lines are determined, only the axial loads in these lines are measured.

A similar experimental setup is described in Xu et al. [33]. In this article a semi-submersible platform is

evaluated with a similar mooring configuration. The goal of this article is to obtain the dynamic motions and mooring forces of the semi-submersible in irregular waves and compare those with a fully coupled numerical model. It was concluded that dynamic motions and mooring forces are predicted accurate with the numerical model. And for this model the mooring forces are only measured as the axial load of the mooring line without the direction.

The last two other articles Peña et al. [22] and Dessi and Minna [9], describe similar experimental setups. The mooring forces are measured in these setups with axial load cells without direction. And both articles conclude that the mooring loads are an important parameter that is not easily measured. In the articles of Shen et al. [27], Qin et al. [23] and Rosa-Santos et al. [25] different types of experimental setups are described. The first two articles evaluate net structured cages. These circular shaped constructions are investigated for their structure responses. Shen et al. [27], modelled a complete setup with mooring lines to the bottom of the tank, whereas, Qin et al. [23], modelled the mooring system with horizontal lines above the water. In both articles mooring forces are measured with axial load cells and the motions of the structures floating ring is measured with accelerometers. Both the articles determine the influence of wave conditions on the structure response, and do not investigate the direction of the measured axial forces.

The last article of Rosa-Santos et al. [25], describes a different approach of measuring the mooring forces. In this article a moored vessel in a port is experimentally investigated. A small scale port is constructed and a vessel is moored with two types of mooring systems: tension mooring lines and fenders. Especially the tension mooring line is of interest for this project. As can be seen in figure 2.1, the tension in the mooring line is measured with a strain gauge plate. This way of measuring the tension forces can be interesting as no heavy objects are introduced in the mooring line.

### 2.1.2. Uncoupled mooring analysis

In the experimental setups described above it can be seen that determining the direction of the mooring force is not examined in the setups. With the direction of the mooring force, more insights can be obtained about different contributions to the total mooring force.

As described in chapter 1, the mooring system and the behaviour of a floating 'rigid' structure can be uncoupled. Due to this uncoupling, several studies are established into a catenary mooring system. They are widely used for the mooring system of offshore structures. Catenary mooring systems have the advantage that they reduce the peak loading due to environmental loading conditions as they provide a slack in the horizontal constrains of the structure. Since catenary systems are widely used, several studies have been performed targeting this system. In the small scale experimental setups by Kitney and Brown [15], Barrera et al. [3], Azcona et al. [2] and Morooka and Tsukada [19], the tension in the mooring lines are measured with an axial load cell and in some setups the movement of the mooring lines are recorded as well. For most setups, mooring lines are modelled with flexible wires or chain and extra springs are added to replicate the properties of the tested catenary mooring line at full scale. Axial forces in the catenary cable are measured with load cells at the attachment point to the oscillator, see figure 2.2.

Different from the other experimental setups, the mooring force in the article of Kitney and Brown [15] is measured above the water. In this setup the mooring line is directed upwards at the anchor point with a pulley system. At the position where the mooring line comes above the water, an axial load cell is integrated in the mooring line. For the other experimental setups, the mooring force is measured at the connection point of the structure with an integrated axial load cell below the water surface.

In the articles of Barrera et al. [3] and Azcona et al. [2], not only the axial mooring forces are measured, but also the motions of the mooring line are measured with motion tracking cameras. Markers along

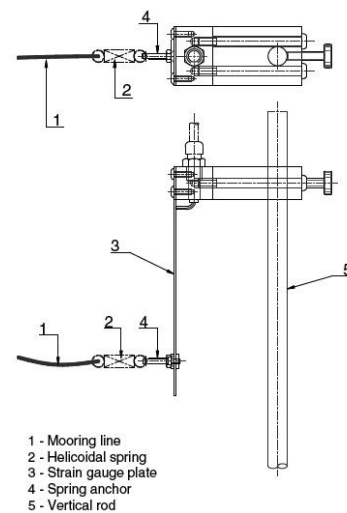


Figure 2.1: Instrumented mooring line to measure tension forces; top: top view, bottom: side view. [25]

the mooring line are recorded during experiments. Spatial plots visualize the motion of the mooring line at the marker positions. In the article of Morooka and Tsukada [19], the acceleration of the mooring line is recorded. With micro-accelerometers, acceleration of the mooring line at the marker positions are measured during experiments and visualized in plots.

The research by Zhang et al. [35] investigated a taut and taut-slack mooring line. The setup of this experiment is similar to the setup of Kitney and Brown [15], however in the setup of Zhang pretension is added in the mooring line and two load cells are included. With this setup the snap loads that are caused by slack are investigated. From this article it can be seen that snap loads should be carefully investigated, since these loads can cause line breakage or load cell overloading.

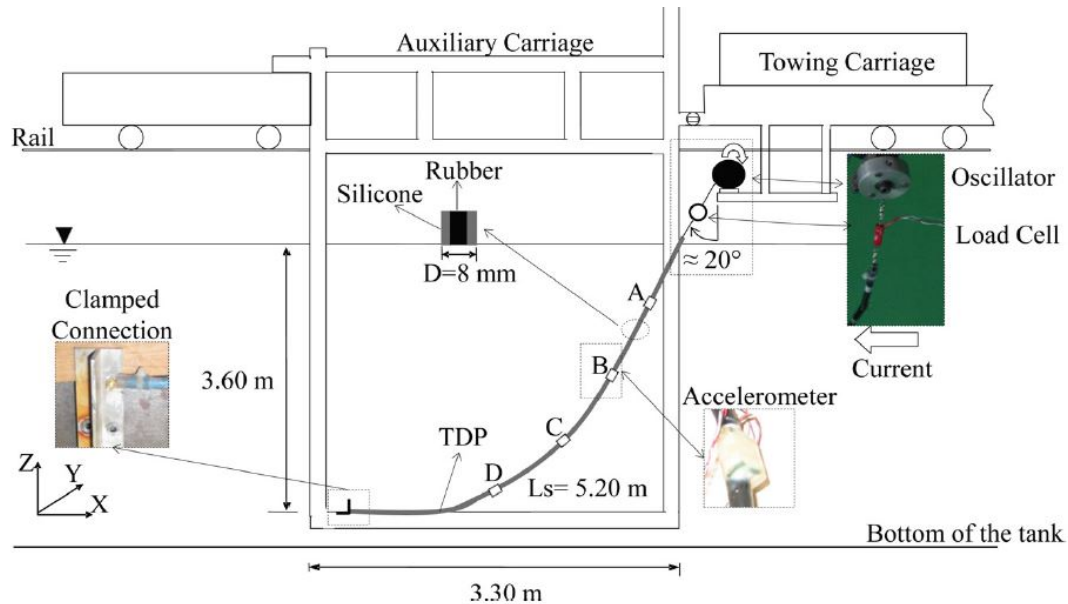


Figure 2.2: Experimental setup for catenary mooring system, mooring line clamped at tank bottom and oscillated at the top. Accelerometers along the mooring line record motions and the load cell at the top records tension, Morooka and Tsukada [19].

## 2.2. Mooring force estimation

For the development of the instrumented mooring system it is important what order of magnitude of mooring forces are expected. With an estimation of the mooring forces, the system can be designed accordingly. To estimate what magnitude of mooring forces can be expected during experimental tests in the towing tank, two articles are further analyzed.

In preliminary experiments of Bruinsma et al. [4], mooring forces of a flexible floating structure are determined. This research was focused on the wave-induced drift of thin, flexible floating plates and performed experimental tests with these type of structures (L 2m, B 1m, h 1.3mm up to 8.2mm). The flexible plate was held on place by fishing lines until the desired wave profile was reached and the plate was released. At the anchor point at the front of the structure, a load cell was included to measure the horizontal forces in the fishing line. The load cell consisted of multiple strain gauges on a bending beam. During the first period when the structure was held in place, the horizontal forces were recorded. The raw data of this force measurement were not further analyzed by Bruinsma et al., and thus not documented. However, for this project a first estimate of the type of force profile can be obtained and therefore the authors provided the data for this project. For the design of a test setup it is important to get an idea of the magnitude of the mooring forces, and with these test results this first approximation can be made. The tested structure is a representative size of structure for the setup that is designed in this project, as the structures meets the dimensional requirements of this project. In figure 2.3 a force measurement is presented of Bruinsma et al.. The force increases until it reaches a steady constant static force including a dynamic part, with green the static wave induced mooring force is indicated and red indicates the total wave induced mooring force, static + dynamic. Next to these wave induced mooring forces, tension forces can be observed in the measurements as the lower value of the static wave induced mooring force. From these experimental results the hydrodynamic forces on a

flexible floating structure can be approximated, for all the experiments the static and dynamic forces are averaged. For the plates with a height of 1.3mm the static force is  $\approx 0.1\text{N}$  and with the dynamical part  $\approx 0.3\text{N}$ . The plates with a height of 8.2mm create a maximum static force of  $\approx 0.3\text{N}$  with dynamical part of  $\approx 0.6\text{N}$ . The maximum pretension introduced in the mooring line is 2.5N. With this first approximation, the instruments of the setup can be designed accordingly. With the use of these test results, it is expected that similar sized flexible floating structures can be tested as well as some smaller or bigger structures, taken into account the limits of the sensors. This means that for bigger structures possibly smaller environmental loading conditions can be applied or the sensor range should be increased.

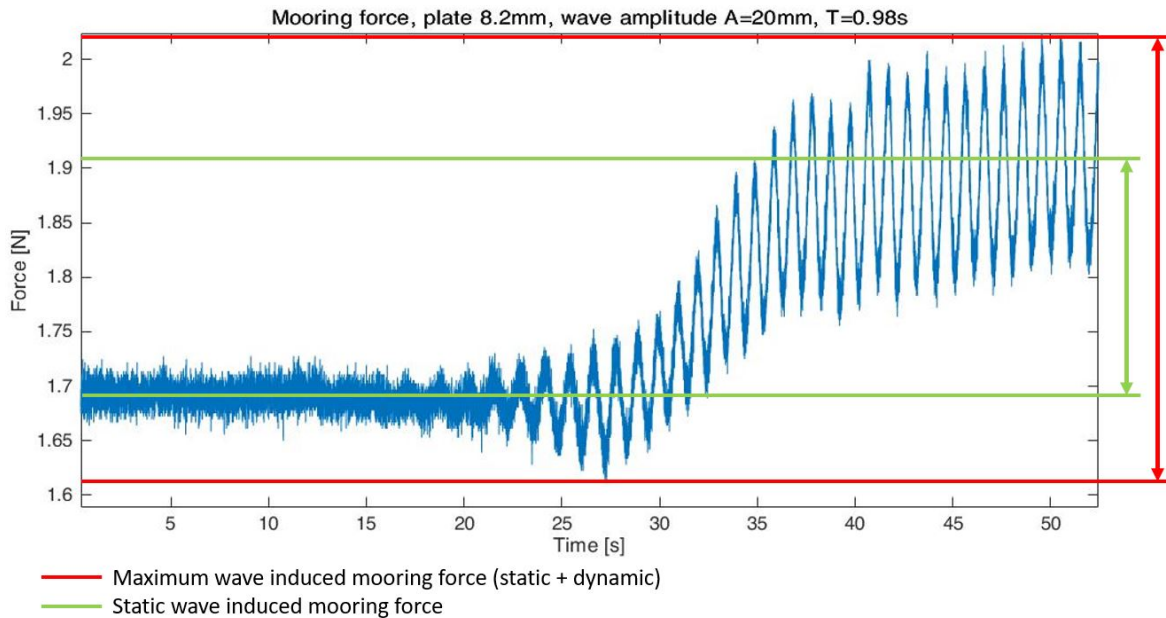


Figure 2.3: Force measurement results of a thin flexible floating structure (8.2mm thick) in wave loading conditions [4]. Green interval: static mooring force, red interval: maximum mooring force (static + dynamic).

In the article of Trapani [31], the mooring force of a flexible floating structure is approximated at full scale. A structure of 200m x 600m x 5mm with  $E=2.29 \cdot 10^9$  Pa is used with the wave conditions  $A=7.4\text{m}$  and  $\lambda=212.2\text{m}$ . In table 3-2 of this article the horizontal mooring force per square meter is calculated for challenging operational conditions. The total force is split up into different components: wind, tide, tension and wave forces. From their analysis they showed that the wind and tide components are dominating forces. The setup that will be designed in this project will only investigate wave loading conditions. As wave loading conditions are neglected in the article of Trapani, this article is not used to estimate of the mooring forces for our system.

Next to the two articles mentioned above, a simple estimation of the mooring forces for flexible floating structures can be estimated by the orbital wave velocity. For this approximation the Airy wave theory is used. Airy wave theory is a linear theory for the propagation of waves. The estimation will be calculated for the small scale structure in wave loading conditions used in the experiments of Bruinsma et al.. In this experiment a structure of 2m x 1m was used, with waves of wavelength  $\lambda=1.5\text{m}$  and wave amplitude  $A=20\text{mm}$  and a waterdepth of  $d=1.25\text{m}$ . With these wave conditions, deep water approximation can be applied. It is assumed that the structure covers half a wave length, resulting in the largest orbital wave velocity over the complete structure. The maximum horizontal orbital velocity ( $\hat{u}_x$ ) is than with the wave frequency  $\omega$ , and the wave number  $k$  shown in Eq. 2.1, 2.2 and 2.3 [12].

$$\hat{u}_x = \omega A \frac{\cosh k(d+z)}{\sinh kd} \quad (2.1)$$

$$\omega = \sqrt{gk} \quad (2.2)$$

$$k = \frac{2\pi}{\lambda} \quad (2.3)$$

The floating structure is positioned at the water surface, therefore the horizontal orbital velocity is calculated for  $z=0$ . This results in a maximum horizontal orbital velocity of  $\hat{u}_x=0.128$  m/s. The orbital wave velocity causes skin friction at the flexible floating structure. This skin friction is approximated with Eq. 2.4, with water density  $\rho_w=1000$  kg/m<sup>3</sup>, surface area structure  $A_s=2$ m<sup>2</sup>, drag coefficient structure  $C_{d,w}$  and orbital velocity  $\hat{u}_x=0.128$ m/s.

$$F_{drag} = \frac{1}{2}\rho_w C_{d,w} A_s \hat{u}_x^2 \quad (2.4)$$

The drag coefficient of the structure in water is not known and should be approximated. This approximation is performed by the boundary layer procedure described in [5]. First, it is determined if the boundary layer is laminar or turbulent with the Reynolds number:

$$Re_L = \frac{VL}{\nu} \quad (2.5)$$

With velocity  $V=\hat{u}_x$ , length structure  $L=2$ m and kinematic viscosity of water at 20°C  $\nu=1.003 \cdot 10^{-6}$  m<sup>2</sup>/s, the Reynolds number for this boundary layer is  $2.55 \cdot 10^5$ . The transition from laminar to turbulent flow is at a Reynolds number of  $10^6$ , therefore the boundary layer is laminar. For the skin friction of a single plate with laminar flow, the drag coefficient can be approximated with [5]:

$$C_{d,w} = \frac{0.664}{\sqrt{Re_L}} = 0.0013 \quad (2.6)$$

With the drag coefficient estimated, the total drag force on the flexible floating structure due to the orbital wave velocity is  $F_{drag}=0.022$ N. This estimation is relative small compared to the measurement results of Bruinsma et al.. Other factors causing horizontal forces are therefore more dominant.

The mooring force on a flexible floating structure is now estimated in different ways. From these estimations, we can approximate the required force sensors to be able to measure the mooring forces. As these approximation can be used for designing the system, care should be taken. First of all, in the results of Bruinsma et al. large fluctuations between different experiments with similar conditions were observed. Especially the pretension in the mooring line fluctuated for different experiments. Secondly, from theoretical knowledge it is not exactly known what components cause the forces due to wave loading. Orbital wave velocity introduces a drag force, however this component is small compared to the measured results in the experiments of Bruinsma et al., [4], where similar conditions were used. The setup that will be designed should therefore be based on the estimations of Bruinsma et al., while keeping in mind the uncertainty of these results.

# 3

## Concept development

In the previous chapters, literature about flexible floating structures and relevant information are stated. The next step in the process of developing a new concept for testing flexible floating structures, is developing different concepts. As the test setup should accommodate several functions, different concepts can be created. The method used for developing new concepts is the Morphological chart. With the Morphological chart new concepts are created, which suffice to all the required functions. The concepts created with the Morphological chart are assessed with a multi criteria analysis (MCA). This method is used to determine which concept is most optimal for achieving the objective, by grading the concepts for different criteria.

### 3.1. Morphological chart

The morphological chart (MC) is a concept generation technique. With this technique problems are analyzed by generating solutions for each problem, these problems are called (sub)functions [7]. For the instrumented mooring system that will be designed in this project, the functions of the system can be divided into six functions.

First of all, the structure should be moored to the fixed surface of the towing tank to ensure the structure to keep position. This problem can be divided into two functions: anchor position and mooring lay-out. Anchor position, the structure should be held on place with mooring lines. This mooring system can be designed with anchors at the side or at the bottom of the test facility. Mooring lines at the bottom of the tank will imitate a full scale structure better than a setup with anchors at the side. Mooring lay-out, mooring should held the structure on place. This can be achieved with two or four mooring lines. The advantage of four mooring lines is better stability of the structure, however pretension is introduced with four mooring lines.

Secondly, the system should be able to measure the forces on the structure. The system should not only measure the forces in the mooring lines, but also the direction of the force/mooring line. For this problem four functions can be divided: force measurement position, force measurement instrument, load cell and angle measurement system. Force measurement position, the goal is to obtain the hydrodynamic forces on a flexible floating structure, force sensors and other sensors are required to obtain these. The position of the sensors have an influence on the behaviour of the structure, and can disturb the free behaviour of the structure. Three positions of the sensors are therefore investigated; at structure, at anchor, and along mooring line. Force measurement instrument, to measure the decomposed forces on a flexible floating structure, instruments are required. For these measurements multi-axial load cells are required or a combination of load cells with an angle measurement system. Load cell, on the market several different types of load cells are available. The solutions for this function are the different working principles of load cells. The multi-axial load cell is able to determine three components of a mooring line, this can also be achieved in a sensor with three axial load cells. Angle measurement, in the industry different methods for angle measurements are available. The method suitable for the concept should be investigated concept specific. Therefore no further subdivisions are listed of angle measurement systems. After the concept is chosen more investigation is required into the angle measurement system.

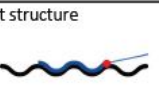
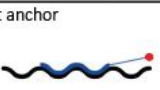
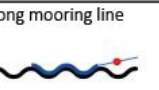
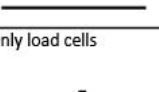
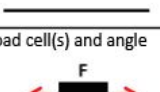
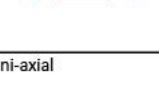
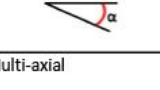
		Solutions →		
		1	2	3
← (Sub) functions	1. Anchor position	Fixed at surface 	Fixed at bottom 	
	2. Mooring lay-out	Two at front 	Two at front + Two at back 	
	3. Force measurement position	At structure 	At anchor 	Along mooring line 
	4. Force measurement instrument	Only load cells 	Load cell(s) and angle 	
	5. Load cell	Uni-axial 	Multi-axial 	
	6. Angle measurement (optional)	Electronic angle measurement	Optical angle measurement	

Figure 3.1: Morphological chart, method to create concepts for a instrumented mooring system for flexible floating structures

For the system described in this study, an instrumented mooring system, the functions are presented in figure 3.1, and to fulfil the functions of the system, all possible solutions for each function are collected. The addition of all possible solutions to the functions completes the overview in figure 3.1.

The next step is to combine solutions of all functions into new concepts. The combinations for the development of concepts are visualized in figure A.1. A short version of the created concepts is shown in figure 3.2. In this figure, different components of the concepts are illustrated. Blue: the outline of the towing tank, gray: the flexible floating structure, black line: the mooring line, Orange/yellow: force measurement instruments. The complete overview of all concepts is presented in figure A.2.

### 3.2. Multi Criteria Analysis

The concepts created with the MC should be evaluated to select a concept. This evaluation is done with the use of a multi criteria analysis (MCA), [28]. With a MCA, argued decisions can be made for complex problems. First the criteria of the system are determined, these criteria are strongly related to the objective of this study. After that, the weight factors for the criteria are determined with the use of mutual ratios. Next, a grading rubric is set to evaluate all concepts according to the same conditions after which the concepts are graded with this grading rubric. Finally, a sensitivity analysis is performed in order to check the reliability of the MCA results.

The first step of the MCA is determining the criteria. The performance of the concepts can be judged with the use of these criteria. Furthermore, it should be carefully investigated what makes a concept

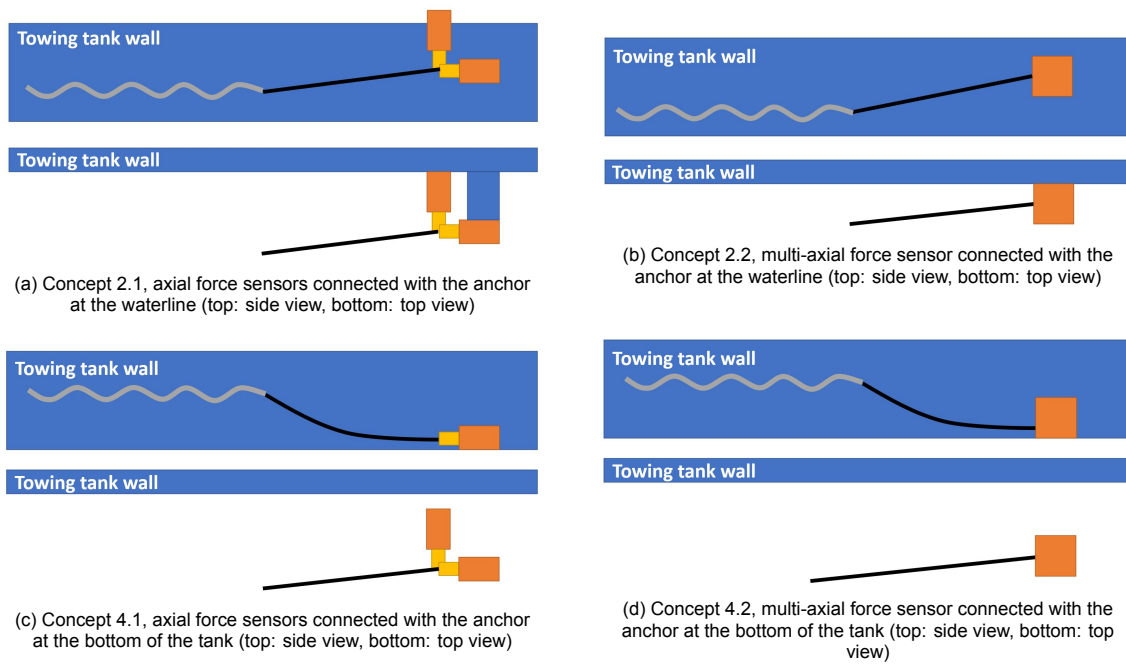


Figure 3.2: Short version of concepts created with the MC. In each figure the top figure is a side view and the bottom figure is a top view of the setup in the tank. The flexible floating structure is illustrated in gray and the force measurement instruments in orange and yellow

suitable for the system and capture this in the criteria. The criteria of the system are determined after exploring the objective of this project. A reliable system is required that can measure the forces on a flexible floating structure, and the factors that determine the performance of the system are listed. Next to the criteria related to the performance of the system, criteria related to the feasibility of the system are listed as well. Lastly the criteria can be structured in groups, called a criteria value tree, this will provide a structured overview of the criteria. The criteria determined for this study are presented in figure 3.3.

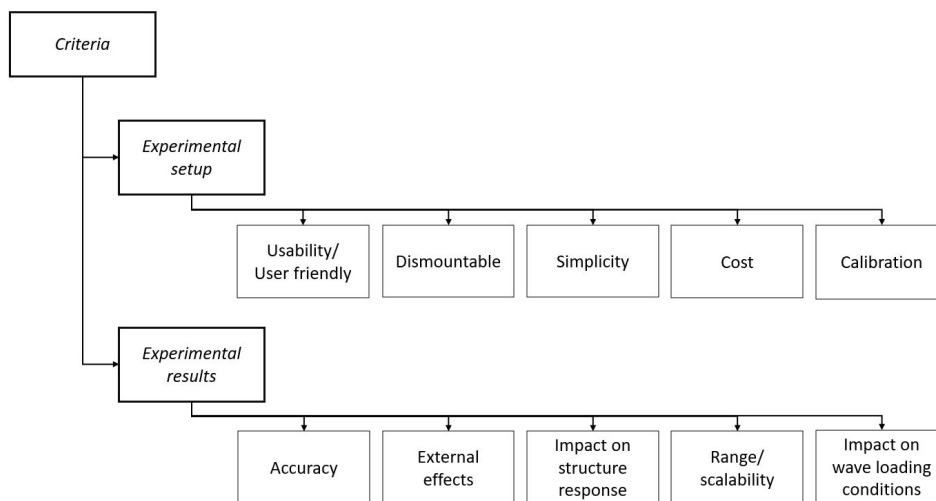


Figure 3.3: Criteria value tree, important criteria to determine the potentials of a concept

For the performance of the system, the criteria are not all equally important. The relative importance of all criteria are determined with the mutual ratio, elaborated in A.2.1. These mutual ratios are then transferred into weight factors for each criteria. The weight factors are elaborated in Appendix A.1.

With the criteria and the weight factors determined, the next step is to set a grading rubric. A grading rubric ensures consistent grades for the concepts. The grading rubric is shown in figure 3.5. For some criteria the conditions for the grades are further elaborated:

- **Accuracy** - The accuracy of the concepts are approximated by analysing the the accuracy of a single mooring line. The required accuracy of force sensors and angle measurement sensors are determined to achieve an load cell grade 'precision' according [13]. For this grade an accuracy of around 0.1%FS - 0.3%FS is required, [13]. With the use of a simple 2D example, the required measurement instruments are determined to achieve an accuracy of 0.1%FS, see figure 3.4. First concepts with only force sensors, for these concepts the forces are measured directly and therefore an accuracy of 0.1%FS is required. For the concepts that include both an angle measurement system and a force sensor, the angle measurement systems should measure the angle with an accuracy of 0.01degrees, to obtain the same accuracy in case a similar force sensor with an accuracy of 0.1%FS is used. From the industry it can be observed that force sensors with an combined accuracy of 0.1%FS are widely available, whereas an angle measurement system with an accuracy of 0.01degrees is not common. In this stage of concept development, this observation is used to distinguish the accuracy of two types of measurement systems. A measurement instrument with only load cells requires less expensive and accurate instruments than a measurement instrument with angle and force sensors.

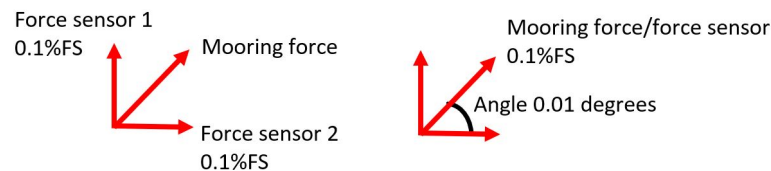


Figure 3.4: Accuracy approximation, left: concepts with only load cells, right: concepts with load cell and angle measurement instrument

- **External effects** - For each concepts mooring forces are measured at a different position. The position along the mooring line determines what additional forces are measured. A measurement system measuring forces directly at the structure will have small external effects. A measurement system along or at the end of the mooring line will measure forces of the mooring line due to wave loading, these are graded as average external effects. Lastly, there are concepts where the measurement system is placed at the bottom of the tank, in this case mooring line effects due to friction to the bottom and the weight of the line are also included, these are graded as large external effects.

In the final step of the MCA grades are given to all concepts with the use of the grading rubric. In figure 3.6 the short version of the MCA is shown, the complete MCA can be found in Appendix A.3. From these figures it can be seen that concept 2.1 and 2.2 get the highest score. These concepts consist of simple setups to obtain the required measurements. The two concepts both score low for the criteria 'impact on wave loading conditions', as they both have measurement instruments in the waterline. Instruments in the waterline will cause the wave loading conditions to be disturbed and additional effects in the measurement. During the detailed development of the system, this problem will be further analyzed to minimize the undesired effects.

### 3.3. Sensitivity analysis

The final step in selecting a concept is the sensitivity analysis. With this analysis the results of the MCA are verified. A sensitivity analysis investigates the influence of input parameters on the output parameters, this is done by altering the input parameters randomly [8]. For the MCA described in this study the input parameters are the weight factors and grades, and the output parameters are the concepts score. For the sensitivity analysis the weight factors are randomly changed by multiplying the weight factor with 0.5 or 1.5. The grades are randomly changed by adding or subtracting 1 point. In figure 3.8 the results of the sensitivity analysis (SA) are presented. First the influence of the concept score are presented, second the influence of the weight factors and in third the influence of the concept

Criteria	Weight	Grading requirements		
		0	1	2
<i>Experimental results</i>				
Accuracy	0.15		Result of angle and force measurement instruments	Result of only force measurement instruments
External effects	0.16	Large effect, mooring line hydrodynamic and friction/other effects	Average effect, mooring line hydrodynamic effects	Small effect, measurement at structure
Impact on structure response	0.18	Instruments at the structure	Instruments along the mooring line	No instruments on the structure nor along the mooring line
Range/scalability	0.11	Fixed range	Scalable range with full setup change	Scalable range with instrument change
Impact on wave loading conditions	0.13	Instruments in the waterline	Small equipment in the waterline	No instruments in the waterline
<i>Experimental setup</i>				
Usability/User friendly	0.07	Combination of different instruments	Combination of several similar instruments	Single instrument
Dismountable	0.02	Undismountable, system to be stored as a whole	Partly dismountable, system to be stored in pieces	Good dismountable, system to be stored complete disassembled
Simplicity	0.04	Use of several different instruments	Use of several similar instruments	Use of single instrument
Cost	0.09	Many expensive instruments	Many inexpensive instruments/few expensive instruments	Few inexpensive instruments
Calibration	0.05	Complete setup calibration	Partly assembled calibration	Pre assembling calibration

Figure 3.5: Grading rubric for MCA, grading conditions to ensure consistent grading of concepts

	Accuracy	External effects	Impact on structure response	Impact on wave loading conditions	Range/scalability	Usability/user friendly	Dismountable	Simplicity	Cost	Calibration	Total score
Weight factor	0.15	0.16	0.18	0.11	0.13	0.07	0.02	0.04	0.09	0.05	
Concept 2.1	2	1	2	2	0	1	2	1	2	1	1.42
Concept 2.2	2	1	2	1	0	2	2	2	1	2	1.38
Concept 4.1	2	0	1	2	2	1	2	1	2	1	1.34
Concept 4.2	2	0	1	2	2	1	2	2	1	1	1.29

Figure 3.6: Short version of the MCA, graded concepts with final scores

score and weight factors are presented. The histogram shows the percentage that a concept scores highest for the MCA for a specific sensitivity input parameter and the box plot shows the spread of the total score of a concept for a specific sensitivity input parameter. The edges of the box represent the 25<sup>th</sup> and the 75<sup>th</sup> percentile, the outer edges the minimum and maximum values without outliers and the markers represent the outliers. The outliers are determined as the scores 1.5 times the interquartile (between the 25<sup>th</sup> and the 75<sup>th</sup> percentile). From the SA it can be observed that the concept score has large influence on the MCA, however 80% of time concept 2.1 or 2.2 scores highest. The influence of the weight factor is relative low. In most cases concept 2.1 scores highest similar to the results of table 3.6. The combined influence of the concept score and weight factor is similar to the results of the influence of only the concepts score, as this influence is highest.

From the SA it can be concluded that concept 2.1 or 2.2 scores best for the MCA. Concept 2.1 and 2.2 differ from each other with the force measurement instrument, concept 2.1 uses a combination of axial load cells to measure multi axial force and concept 2.2 uses a prefabricated multi axial load cell. With a combination of axial load cells the range of each individual load cell can be changed, whereas this is not possible for a prefabricated multi axial load cell. The flexibility of the range of each individual load cell can be useful to investigate different mooring and instrument configurations, for this reason concept 2.1 will be used during the detailed design of the setup, figure 3.7.

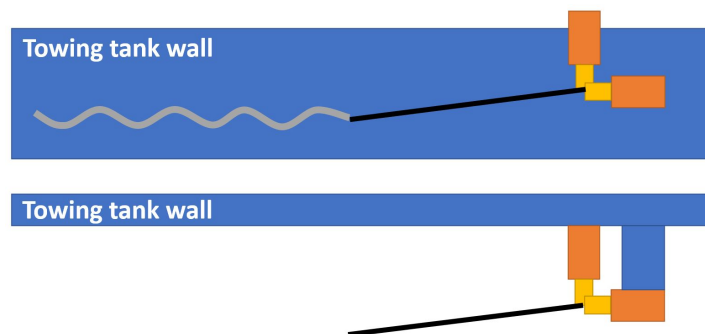
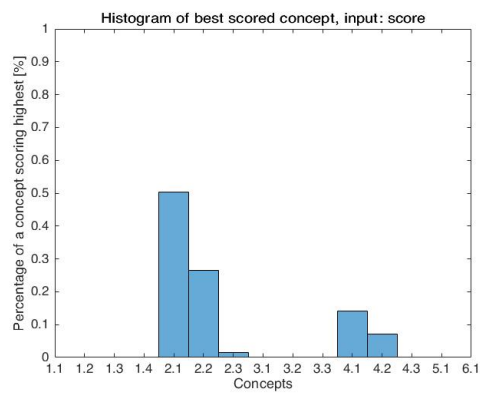
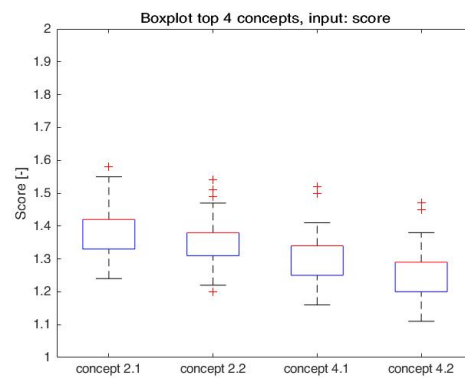


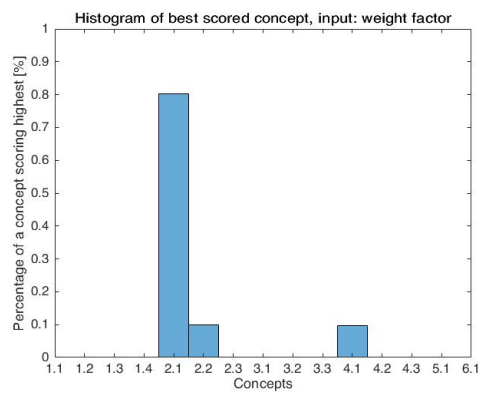
Figure 3.7: Concept 2.1, concept selected from the concept development



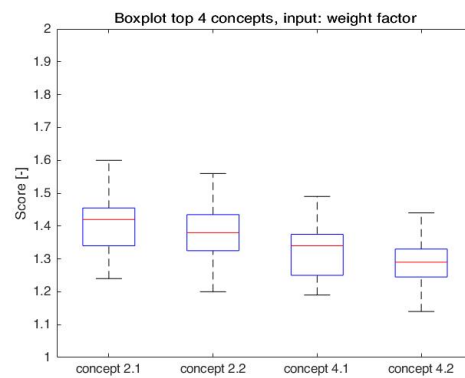
(a) Histogram of highest scoring concept for the sensitivity of concept score



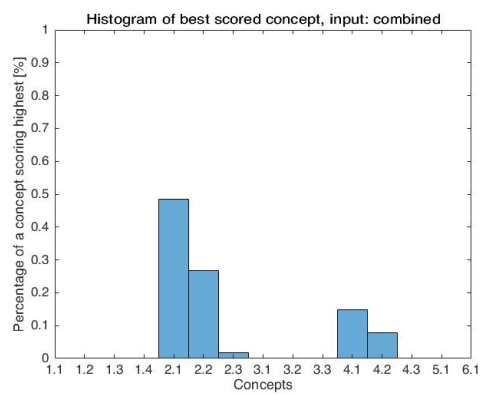
(b) Box plot of the best four scoring concepts, presenting the influence of the concept score



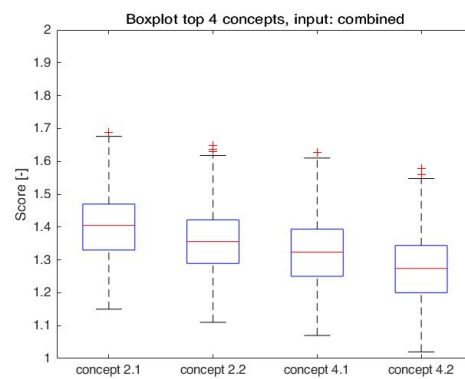
(c) Histogram of highest scoring concept for the sensitivity of weight factor



(d) Box plot of the best four scoring concepts, presenting the influence of the weight factor

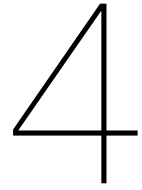


(e) Histogram of highest scoring concept for the sensitivity of concept score and weight factor



(f) Box plot of the best four scoring concepts, presenting the influence of the concept score and weight factor

Figure 3.8: Sensitivity analysis of the MCA, the influence of the input parameters (concept score and weight factor) are investigated



## Problem analysis

In the objective it is mentioned that a new instrumented mooring system for flexible floating structures is required, since it was concluded that conventional test setups for mooring force measurements are not directly usable. Conventional test setups use large sensors directly on the structure which is not possible for flexible floating structures, as the sensors will influence the free motions of the structure too excessively. Therefore, in the previous chapter a new concept is selected to measure the mooring forces of flexible floating structures. To achieve valuable results from the experiments, the system should meet the requirements described in section 1.2.1. The system must be able to measure forces with high accuracy (0.1%FS – 0.3%FS), [13]. With high accuracy it is possible to measure small deviations due to changing circumstances, and this is essential. Additionally, the system must be able to measure the direction of the mooring force. With the known direction of the mooring force it is possible to determine all components, and with these components more results can be collected about the forces.

For the chosen concept it is important to understand what challenges should be investigated in this project. In current research, mostly the axial mooring forces are measured. Measuring the mooring forces in all components will therefore require new research. Equally important is the calibration procedure. This procedure is not investigated thoroughly in current research, and should therefore be investigated. With knowledge about the influence of the calibration experiments, it can be determined upfront what calibrations are required and also the amount of calibrations that are required. Before the research questions are determined, a closer look has to be taken into the theoretical background of the calibration procedure. The common used calibration theory and a proposed optimized procedure are explained briefly, in chapter 6 the calibration theory is explained more extensively. These two calibration procedures are important to formulate the research questions.

### 4.1. Calibration theory

Calibrating a linearly dependent sensor is performed with a linear regression analysis. With this analysis, an expression is developed that describes the behavior of a variable of interest.

In literature, two articles describe a linear regression analysis for calibrating a linear dependent sensor, 28th ITTC [1], Rawlings et al. [24]. In the article of Rawlings et al. [24] the regression analysis is extended to a multi variable regression in matrix form which is required for the sensor in this project. For this reason, this article is used for the brief explanation of the regression analysis.

As stated above, a linear regression analysis develops an expression that describes the behaviour of a dependent variable (Y), assuming that the behaviour is linear. Variables that are thought to provide information of the variable Y, are incorporated into the model as predictor variables. These variables are called independent variables (X). For the force sensors used in our sensor the variable Y is the measured voltage and the independent variable X is the weight applied on the sensor. For a single sensor the linear model only consists of one dependent variable Y and one independent variable X. To apply a linear regression analysis, several observations are required for the dependent variable Y. These observations can be plotted for the dependent variable Y against the independent variable X. With this scatter, the functional relationship between the variables X and Y can be approximated with

the equation of a straight line, ([24]):

$$Y_i = \beta_0 + \beta_1 X_i \quad (4.1)$$

Where  $i$  denotes a particular observation,  $\beta_0$  is the intercept at  $X_i=0$  and  $\beta_1$  is the slope of the line. As the data points are not in a straight line, there is no exact solution for the regression parameters  $\beta_0$  and  $\beta_1$ . For the solution of these parameters the 'best' estimation is determined. Finally the regression equation for a single variable sensor is, ([24]):

$$\hat{Y}_i = \hat{\beta}_0 + \hat{\beta}_1 X_i \quad (4.2)$$

Where  $\hat{Y}_i$ ,  $\hat{\beta}_0$  and  $\hat{\beta}_1$  are the 'best' approximation for the linear dependent variable. For the sensor of this project, a total of three force sensors are used. Combining three sensors, causes interaction between the sensors. And this interaction causes thereafter that the dependent variable  $Y$  is not dependent on a single variable  $X$ , but it becomes dependent on three variables  $X$ , ([24]):

$$Y_i = \beta_0 + \beta_1 X_{i1} + \beta_2 X_{i2} + \beta_3 X_{i3} \quad (4.3)$$

For the calibration procedure this means that a multi regression analysis is required to calibrate the complete sensor. However, in practice, the calibration procedure is often simplified, where the interaction between different sensors are neglected to simplify the calibration procedure. With this simplification, only the regression slope  $\beta_1$  is scaled accordingly and  $\beta_2$  and  $\beta_3$  are neglected. From literature, it is not clear in which case this simplification is feasible and therefore this should be investigated. This is especially interesting, because a small example shows that this simplification can cause significant errors, see appendix B. An extended explanation of the linear regression analysis can be found in chapter 6.

## 4.2. Research question

To get a working design, requirements of the setup are determined as well as the challenges of the selected concept. To meet the requirements and answer the main challenges, the following research question and sub-questions are formulated:

*"How does the accuracy of the proposed system depend on its sensor configuration and the calibration procedure and how can the accuracy be optimized to acceptable levels?"*

To answer the main research question, two sub-questions are formulated. With these sub-questions various aspects of the system are analyzed separately, and will contribute to answering the main research question.

- *What is the effect of the force sensor configuration on the accuracy and what is the optimal configuration taken into account the accuracy and the usability?*

The force sensor of the proposed concept is a multi-axial force sensor, and will be build out of multiple force sensors. As the uncertainty of the measurements should be reduced below acceptable levels, it is important to identify the influence of the sensor configuration on the measured uncertainty. When this influence is known, the configuration can be optimized to achieve an accuracy within acceptable levels.

- *What are feasible calibration procedures and what is the accuracy of each procedure?*

The multi axial sensor can be calibrated according different calibration procedures. To identify which calibration procedure should be selected, the influence on the accuracy is investigated as well as the usability of different calibration procedures.

## Development of test setup

In this chapter the design of the sensor setup is elaborated. In chapter 3, concept 2.1 was chosen as the best option for this setup. For the detailed design of the sensor, force sensors are selected and the dimensions of the additional frame is determined. This process is described in this chapter.

### 5.1. Axial force sensor type

In chapter 2, the mooring force was approximated to be around 2.5N. With this approximation, force sensors can be selected for the sensor. As the mooring force was approximated with a small amount of data, a large safety factor of 3 is applied to determine the required force sensor type. With this safety factor, the force sensors should have a range up to 7.5N. Although, there are plenty of force sensors available which have a range up to 7.5N, yet bigger force sensors with a range up to 20N are selected. In the lab at the TUDelft, the smallest available force sensors have a range up to 20N. And due to long delivery times, these force sensors were selected. Moreover, this test setup is a first attempt to identify the required materials, configuration and procedures. Therefore, it is not required to collect the exact materials. This project will investigate a first attempt of the sensor and recommends afterwards what specific materials are required.

The sensors available in the workshop at the TUDelft are Zemic type 1HM miniature sensors. These sensors have a maximum range of 20N, a sensitivity  $1.0 \pm 0.15$  mV/V and a maximum deflection of 0.25mm. More specification of the sensor can be found in [34]. Axial force sensors are sensitive for forces in a single direction, in other directions the sensors are designed to be not sensitive.

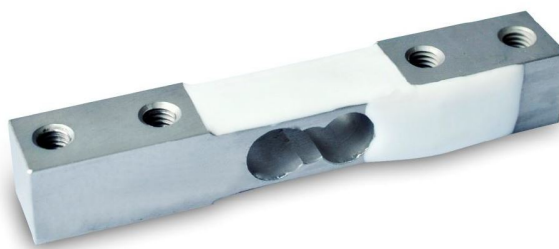


Figure 5.1: Zemic 1HM miniature sensor, axial force sensor, [34]

### 5.2. Sensor frame

An important requirement of the sensor setup is that it should be able to measure a force in three directions. For the selected concept 2.1, this is achieved by using three force sensors. To support these three force sensors, a frame is required. This frame should be able to support the sensors in the correct position and should be stiff to prevent unpredictable deflections. The positions of the sensors are chosen in a way that all sensors are orthogonal to each other. This means that the sensitive direction of each sensor is pointing in the x, y or z direction of an axis system. In figure 5.2, an overview of the

sensor frame is shown. The force sensors are connected to the frame and with connection plates and threaded rods, the force sensors are connected to a single point. At this point, a connection block connects the threaded rods and a mooring line can be attached. The threaded rods ensure that the force in the mooring line is transferred to the force sensors, on top of that it ensures that the force sensors are mostly loaded in their sensitive direction, as threaded rods are stiff in their axial direction and flexible in the lateral directions.

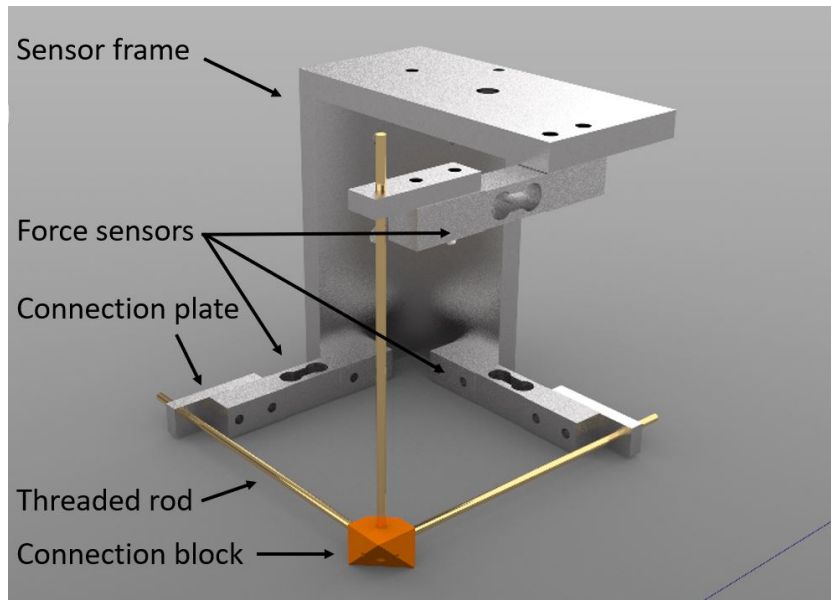


Figure 5.2: Rendered image of the sensor frame, items indicated

### 5.2.1. Frame dimensions

The dimensions of the frame are determined by the required length of the threaded rods. Threaded rods are stiff in their axial direction and have a low bending stiffness. These characteristics ensure that the force sensors are mostly loaded in their sensitive direction. Axial force sensors are designed to measure loads in a single direction, the sensitive direction. Forces and moments in other directions can cause unexpected measurement results, and thus these forces and moments should be reduced to a minimum. With the use of Euler Bernoulli equations, the length of the threaded rods is determined. First, the setup with threaded rods is simplified into the drawing shown in figure 5.3.

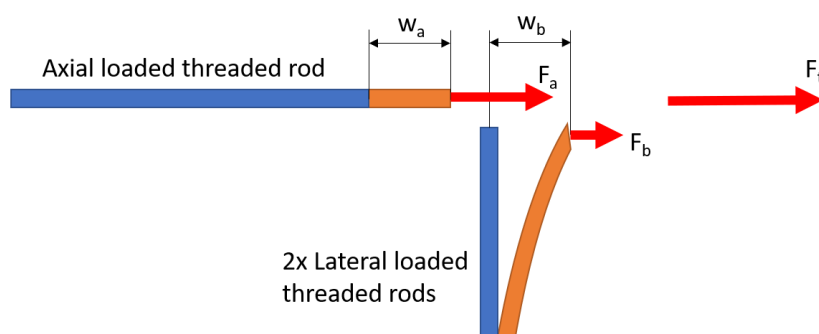


Figure 5.3: Simplified drawing of force distribution in threaded rods

A threaded rod is loaded with a force in the axial direction,  $F_t$ . Due to this force, the deflection of the 3 rods are illustrated in orange. The first rod is loaded in axial direction and the other two rods are loaded in lateral direction. The tip deflection of the axial loaded rod is defined as:

$$w_a = \frac{F_a \cdot L}{A \cdot E} + 0.25\text{mm} \quad (5.1)$$

Where  $F_a$  is a fraction of the total axial force  $F_t$ ,  $L$  is the length of the rod,  $A$  is the area of the cross section,  $E$  is the young's modulus of the rod and 0.25mm is the maximum deflection of the sensor. The first part of the equation calculates the extension of the rod and the second part is the maximum deflection of the sensor specified by the supplier.

The tip deflection of the two lateral loaded rods is defined as:

$$w_b = \frac{F_b \cdot L^3}{3 \cdot E \cdot 2 \cdot I_w} \quad (5.2)$$

$$I_w = \frac{\pi \cdot r^4}{4} \quad (5.3)$$

Where  $F_b$  is a fraction of the total axial force  $F_t$ ,  $L$  is the length of the rod,  $E$  is the young's modulus of the rod,  $I_w$  is the area moment of inertia of the rod and  $r$  is the radius of the rod. As a total of two rods are loaded in lateral direction, the area moment of inertia is multiplied by 2.

The next step is to combine the deflection equations to determine the required length. The threaded rods are connected to each other at the tip, which means that the tip deflections of all the rods are equal:

$$w_a = w_b \quad (5.4)$$

Furthermore, the total force is the sum of the forces in the rod tips:

$$F_t = F_a + F_b \quad (5.5)$$

By combining formula 5.1, 5.3, 5.2, 5.4 and 5.5, we can formulate an expression for the fraction of the total force ( $F_t$ ) that is taken by the axial loaded rod ( $F_a$ ), dependent on the length of the rod. With  $r=1.19\text{mm}$  the core radius of M3 threaded rod, young's modulus of  $E=100\text{GPa}$  for brass, the force distribution is formulate as equation 5.6.

$$F_a = \frac{1.06 \cdot 10^9 \text{mm}^2 \cdot L^3}{1.06 \cdot 10^9 \text{mm}^2 \cdot L^3 + 2.25 \cdot 10^9 \text{mm}^4 \cdot L + 1.25 \cdot 10^{13} \text{mm}^5} \cdot F_t \quad (5.6)$$

Finally, a maximum force that can be taken by the two lateral rods should be chosen. As mentioned above, the force taken by the two lateral rods should be reduced to a minimum to ensure that a large part of the force is taken by the sensitive direction of the force sensor. From the formula, we can see that infinite long rods reduce the lateral force to a minimum, however we should take into account the physical dimensions as well. After some iterations, it was found that in case one percentage of the total force is taken by the lateral rods, the rods should have a length of at least 106mm. Therefore, the length of the rods is designed to be 110mm.

With the parameters determined above, the complete frame is designed. The sensor frame and connection plates are fabricated from aluminium plates, the threaded rods are made of brass and the connection block is 3d printed. The drawings of the sensor frame and connection plates can be found in appendix C.1.

### 5.2.2. Axis system

For the test setup, different axis systems will be used further in this report. In this section, the different axis systems are illustrated and elaborated.

First of all, an axis system KLM is determined for the force sensor. In figure 5.4, the axis system is illustrated. For this axis system, M is in the positive, sensitive direction of the sensor.

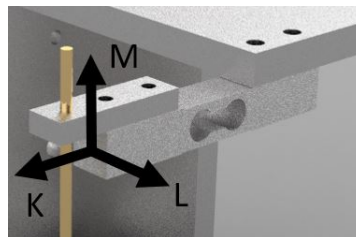


Figure 5.4: Axis system sensor

The second axis system is determined for the sensor frame  $U, V, W$ . In figure 5.5, the axis system is illustrated and sensor numbers are given to each sensor. The positive sensitive direction of the sensors are aligned with the positive direction of this axis system. By doing this, sensor 3 is positioned differently from the other two sensors. For sensor 1 and 2, the positive sensitive direction of the sensors are in the similar direction as the threaded bars. However, for sensor 3, the sensitive direction of the sensor is in the opposite direction of the threaded bar. In the results of the experiments later in this report, this will be visible.

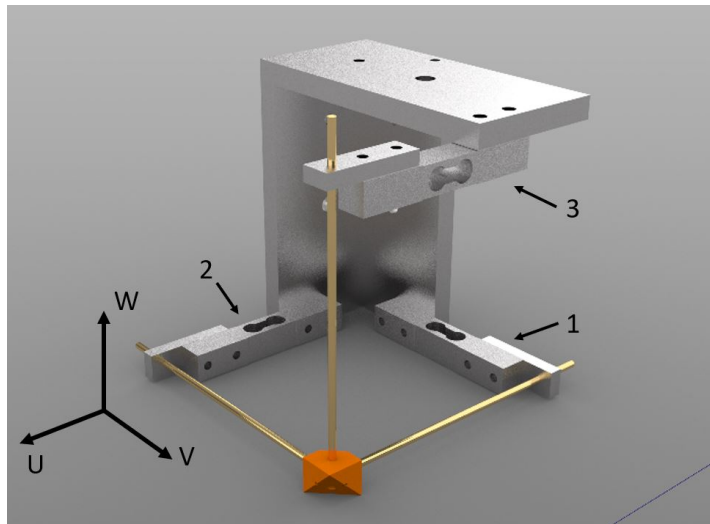


Figure 5.5: Axis system sensor frame

The last axis system is the global axis system  $X, Y, Z$ . This axis system is shown in figure 5.6. In this figure,  $X$  is in the propagation direction of the waves in the towing tank.

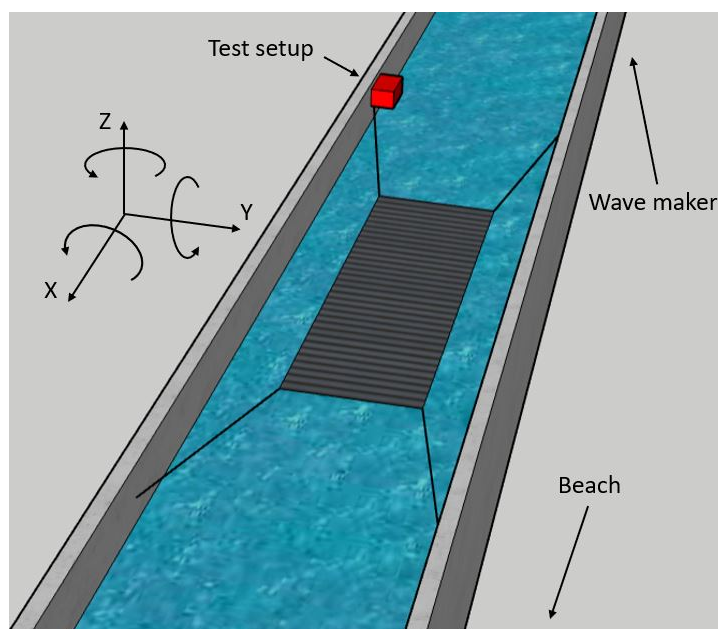


Figure 5.6: Global axis system

### 5.2.3. Sensor position

The sensor frame will be installed in a towing tank and connected to a mooring line of a flexible floating structure. The mooring line of the flexible floating structure should be positioned as horizontal as possible, to minimize vertical mooring loads on the structure. The connection block of the sensor frame

should therefore be positioned as close to the undisturbed water surface as possible. The first position is to install the sensor frame in the orientation, such that the X,Y,Z and U,V,W axis systems are in line. When the connection block is positioned close to the water surface, likewise force sensor 1 and 2 are close to the water surface. Although, force sensors are water resistant to a certain extent, these sensors are sensitive and should be protected from harsh environments. To still be able to position the connection block as close to the water surface as possible, the sensor frame should be rotated relative to the X,Y,Z axis system. To maximize the vertical distance of the force sensors with the water surface, the sensor frame is rotated 45 degrees around the Y axis in positive direction and 35 degrees around the X axis in negative direction, this is the rotated position. The upright and rotated position are illustrated in figure 5.7.

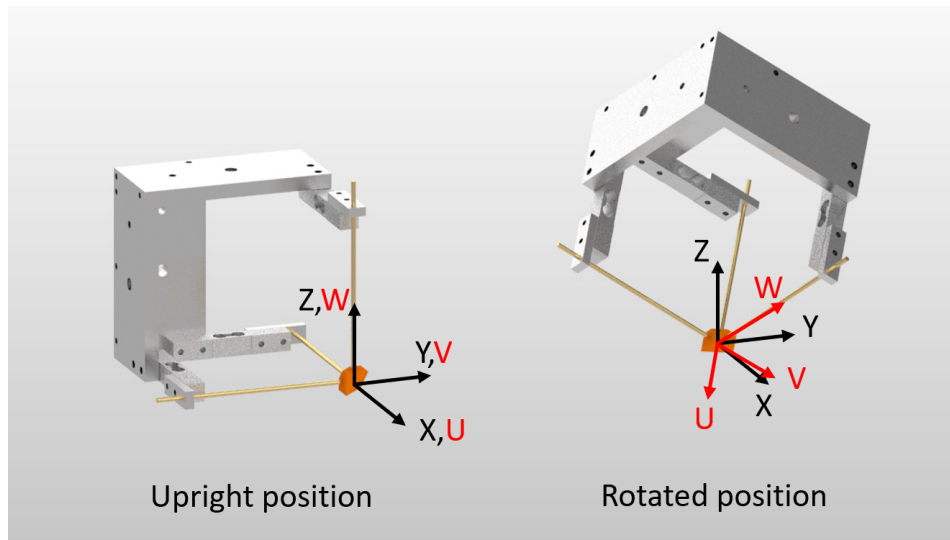


Figure 5.7: Sensor frame, left: Upright position, sensor frame and global axis system are in line, right: Rotated position, sensor frame axis system rotated relative to global axis system

# 6

## Calibration

Before the sensor designed in chapter 5 can be used in experimental setups, calibration of the sensor is required. With calibration experiments, output signals of a sensor can be translated to desired data. Without this translation, it is impossible to obtain valuable results of the sensor. Next to the translation of the output signals, the accuracy of the sensor can be obtained with the calibration experiments.

The sensor developed in this report consists of three force sensors. Calibration of a single force sensor consists of determining the regression parameters of the sensor. A single force sensor only has one output signal that its translated to the desired data, therefore two calibration parameters are determined. For the calibration of combined force sensors, mutual influences can also be taken into account. Due to these mutual influences, different calibration approaches can be applied. These different approaches are discussed in this chapter.

First, the calibration procedure for the single sensors are presented. The theory for this procedure is explained, followed by the calibration setup and the required experiments. Furthermore, the results of the calibration procedure are presented. In the second part, the calibration procedure for the complete sensor in the upright position is presented in the similar sequence as the single sensor calibration procedure: theory, calibration setup, experiments and the results. The last calibration procedure that is explained, is for the complete sensor in the rotated position. The procedure is explained in a the similar sequence. At the end of this chapter, the results of all calibration procedures are discussed and the first conclusions are drawn. The calculations performed for the calibration experiments are shown in appendix F.1.

### 6.1. Single sensor calibration

The first part of the calibration procedure is to investigate the force sensors individually. The characteristics of the force sensors are specified by the supplier [34]. To validate these specifications and to determine the sensitivity of the sensor in all directions, calibrations are performed with the single sensors.

#### 6.1.1. Theory single variable regression analysis

Forces on a force sensor are measured by the sensor and the sensor translates these forces into voltages, the output signal. To determine the relation between the force and output voltage, a translation factor is required. This translation is determined with the regression analysis. In figure 6.1 a simple example of a regression analysis is shown.

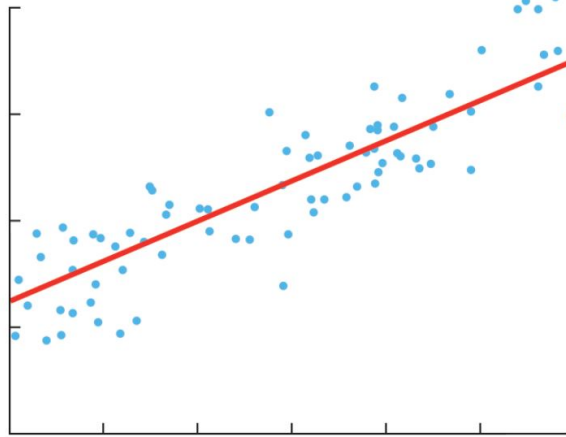


Figure 6.1: Example regression analysis, blue dots: data points, red line: relation between the output signal on the Y axis and the input variable on the X axis, [11]

In this figure data points are plotted with blue dots. To determine a relation between the output and input values, y axis and x axis respectively, a red line is drawn through the blue data points. Force sensors are linear dependent, which means that a straight line can be drawn through the data points. The fundamental equation for the regression analysis is [1]:

$$y = a + bx \quad (6.1)$$

This equation describes the relation between the dependent output value  $y$  and the independent input value  $x$ . For this analysis two parameters are determined,  $a$  and  $b$ .  $a$  is the intercept of the regression line, the position where the line crosses at  $x=0$ , and  $b$  is the slope of the regression line. As can be seen in figure 6.1, the red line does not cross all blue data points. Therefore, this regression line is an estimation. Equation 6.1 is written as, [24]:

$$\hat{Y}_i = \hat{\beta}_0 + \hat{\beta}_1 X_i \quad (6.2)$$

Where  $\hat{Y}_i$  is the estimated output signal,  $\hat{\beta}_0$  is the estimated intercept,  $\hat{\beta}_1$  is the estimated slope and  $X_i$  is the input value.

To determine the 'best' estimation of the regression line, different approaches can be applied. In this project, the least square method is used to determine the regression parameters. With the least square method, first the residuals are determined after which the sum of the squares are minimized. The sum of the squares can be found with, [24]:

$$SS(r) = \sum_{i=1}^n (Y_i - \hat{Y}_i)^2 \quad (6.3)$$

In this equation,  $n$  is the number of data points used for the regression analysis.  $Y_i$  is the measured output signal and  $\hat{Y}_i$  is the estimated output signal.

By minimizing the squares of the residuals, the regression parameters are determined as, [24]:

$$\begin{aligned} \hat{\beta}_1 &= \frac{\sum(X_i - \bar{X})(Y_i - \bar{Y})}{\sum(X_i - \bar{X})^2} = \frac{\sum x_i y_i}{\sum x_i^2} \\ \hat{\beta}_0 &= \bar{Y} - \hat{\beta}_1 \bar{X} \end{aligned} \quad (6.4)$$

The most important regression parameter is the slope. With the slope, the sensitivity of the sensor is expressed. The sensitivity is provided by the supplier and will be checked during these calibration experiments.

The regression analysis can be written in matrix form. The analysis is similar to the equation written above, however for the regression analysis of the complete sensor, it is more convenient to write it in

matrix form. First of all, the data points used to determine the intercept and slope are written as, based on [24]:

$$\begin{pmatrix} Y_1 \\ Y_2 \\ \vdots \\ Y_n \end{pmatrix} = \begin{bmatrix} 1 & X_{11} \\ 1 & X_{21} \\ \vdots & \vdots \\ 1 & X_{n1} \end{bmatrix} \times \begin{pmatrix} \beta_0 \\ \beta_1 \end{pmatrix} \quad (6.5)$$

Where  $Y$  is the output signal for each data point  $n$ ,  $X$  is the input variable,  $\beta_0$  is the intercept and  $\beta_1$  is the slope. And this equation is simplified to the equation, [24]:

$$\mathbf{Y} = \mathbf{X}\boldsymbol{\beta} \quad (6.6)$$

With this simplified equation, the regression parameters  $\boldsymbol{\beta}$  can be estimated with, [24]:

$$\hat{\boldsymbol{\beta}} = (\mathbf{X}'\mathbf{X})^{-1} \mathbf{X}'\mathbf{Y} \quad (6.7)$$

Now that the regression parameters of the sensor can be determined, more information about the accuracy of the sensors should be determined. The accuracy of the sensor can be investigated by the confidence interval. The confidence interval provides a range for the input and output values. Usually this confidence limit is given for a 95% confidence interval. In figure 6.1, it can be observed that the blue data points are not in line with the red regression line. The scatter of the data points (residuals) determines the confidence interval. The more the data points are scattered around the regression line, the bigger the confidence interval is. The first step to determine the confidence interval is to determine the standard deviation, [1]:

$$SEE = \sqrt{SS_R/(n-2)} \quad (6.8)$$

With the standard deviation of the regression analysis the confidence interval can be calculated with, [24]:

$$CI = +/- t_{\alpha/2, n-2} \cdot \sqrt{SEE^2 + x \cdot ((\mathbf{X}'\mathbf{X})^{-1} \cdot SEE^2) \cdot x} \quad (6.9)$$

Where  $t_{\alpha/2, n-2}$  is the Student-t inverse probability density function at  $\alpha/2$  confidence limit, with  $\alpha/2=0.025$  for a 95% confidence limit, and  $x$  is the input variable.

From this equation, it can be observed that the confidence interval changes over the input variable as it is dependent on the input variable  $x$ . It is also dependent on the Student-t inverse probability density function. These two variables depend on the amount of data points, therefore a factor of the confidence interval can be determined upfront the experiments by choosing a certain amount of experiments (data points). The Student-t inverse probability density function decreases for an increase of data points, see table A.1. in [24]. With equation 6.9 and the Student-t probability density function, a curve is plotted where the confidence factor is plotted against the amount of data points, figure 6.2. As the confidence interval is dependent on  $x$ , two lines are curves are plotted. The first curve is the maximum confidence interval and the second curve the minimum confidence interval.

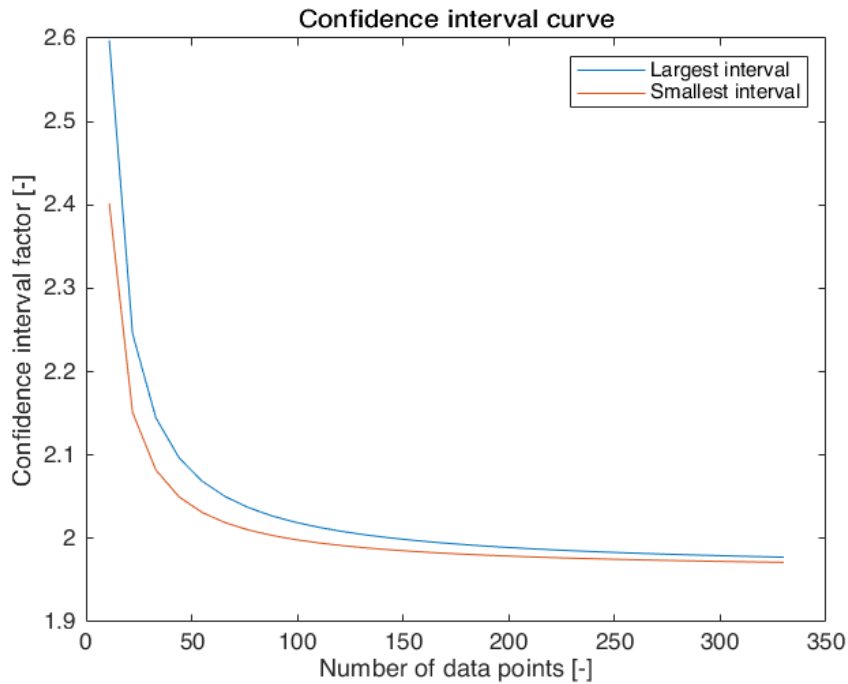


Figure 6.2: Confidence factor plotted against the amount of data points

From this plot, it can be seen that the confidence factor converge to around 2, this means that more experiments will decrease the confidence interval. Nevertheless, the downside of more experiments is the required time for the experiments. To select the required amount of experiments, it is stated that an extra experiment is no longer contributing in case it decreases the confidence factor with less than 0.5%. This means that the slope of the curve in figure 6.2 should be less than 0.005. At 80 data points the slope is below this level, and therefore at least a total of 80 data points are required for the calibration experiments.

For the final regression line, the confidence interval can be plotted by adding the confidence interval to the regression line, equation 6.10 and figure 6.3. The data points are indicated with blue points, the regression line with a red line and the confidence interval with dashed red lines.

$$Y = X\beta + CI \quad (6.10)$$

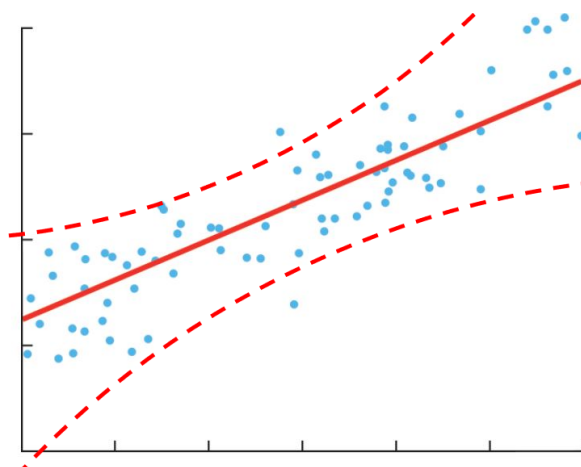


Figure 6.3: Example regression analysis with confidence interval, red dashed lines: confidence interval

### 6.1.2. Calibration setup

In the previous section, it is described what information is required to perform a regression analysis for a force sensor. To obtain this data, several experiments should be conducted with the sensors, and to facilitate these experiments a calibration setup is required. The requirements of this calibration setup are:

- Apply loads in three orthogonal directions on the sensor
- Apply loads in like manner as in the sensor frame

For the calibration setup of the single sensors, a simple aluminium support is fabricated on which the force sensor can be attached. In figure 6.4, this support is shown. The support is clamped onto a horizontal table. The connection plate is attached to the force sensor to apply loads at the same position as in the sensor frame. The loads are applied with weights, and thus the loads are applied in the direction of the gravitational force. Detailed information about the applied weights during the calibration experiments are described in the next section.

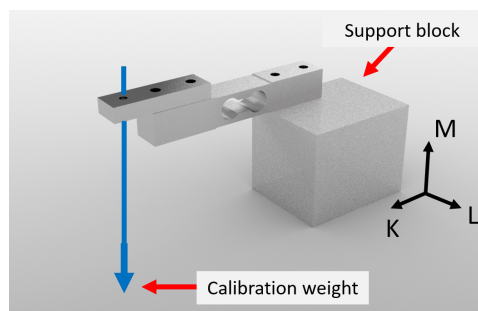


Figure 6.4: Calibration setup for the single sensor in the sensitive direction

To obtain the regression parameters of the sensor in the non-sensitive direction, another setup is used. From experiments for the non-sensitive direction, it was shown that small oscillations of the free hanging weight cause large output voltage fluctuations. These fluctuations are caused by the small load components in the sensitive direction of the force sensor. Therefore, a single force sensor is attached to the sensor frame, to determine the regression parameters of the sensors in the non-sensitive direction. By applying weights with the use of a pulley, oscillations of the weight are removed. Furthermore, forces in the non-sensitive direction are applied with a distance to the force sensor in the sensor frame. This distance causes an extra couple on the force sensor. As we are interested in the sensitivity of the force sensors in the frame, this distance should be taken into account as well. The setup for the non-sensitive direction is shown in figure 6.6.

The sensors are connected to a data acquisition PC, PXIe-1078 National Instruments chassis with a National Instruments strain/bridge input module PXIe-4330. With this setup, a sampling rate of 1000 Hz and a 24 bit resolution are achieved and an anti-alias filter is build in the system. With this system the output values of the sensors are recorded. Specifications of the data acquisition PC and strain/bridge input module are listed in [21] and [20].

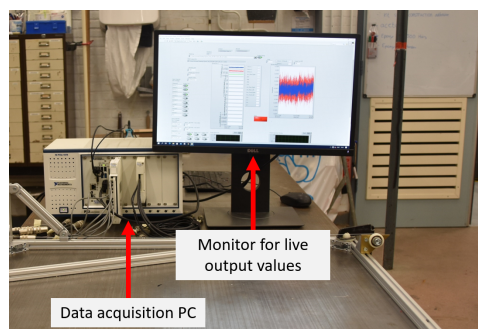


Figure 6.5: Data acquisition PC to monitor and collect output data

### 6.1.3. Calibration experiments

The calibration experiments for the single sensor are needed to determine the regression parameters of the single sensors. For each force sensor, three experiments are required to determine the sensitivity of the sensor in the three axis (K,L,M).

The different calibration experiments are grouped in table 6.1. Each group is given its own calibration reference number and represents the experiments required for the regression analysis of a single sensor direction. Each calibration group is explained below. More detailed information of each experiment can be found in table G.1.

Table 6.1: Calibration experiments for single sensor with reference number

Calibration reference number	Type of calibration experiment	Force sensor	Experiment numbers
S1	Single sensitive M axis	1	21-28
S2	Single sensitive M axis	2	29-32,34-37
S3	Single sensitive M axis	3	39-46
S4	Single non-sensitive K axis	1	57-64
S5	Single non-sensitive K axis	2	78-79
S6	Single non-sensitive K axis	3	67-72,74-75
S7	Single non-sensitive L axis	1	47,49-54,56
S8	Single non-sensitive L axis	2	76-77
S9	Single non-sensitive L axis	3	65-66

Calibration S1-S3 are illustrated in figure 6.4. The force sensor is attached to the simple support and a weight holder is placed at the tip of the sensor. For the calibration in the sensitive direction S1-S3, the calibration weights of table 6.2 are used. During a single experiment, the weights are stacked until the full weight is applied on the sensor after which the weights are removed in the opposite order. This procedure is repeated 7 times to collect the right amount of data points.

The weights are selected by the range of the sensors and the amount of steps in this range. The selected force sensors have a range of 20N or around 2kg in their sensitive direction. For the calibration of the sensors sensitive direction, the range is divided into 9 weights. As there is an additional frame of around 150 gram connected to the wire to put the weights on, the calibration weights can be maximum 1800 gram. The weight distribution for the single sensor calibration is listed in table 6.2. In the second column the weight of a single load is given and in the fourth column the total stacked weight of all above-mentioned loads is given. The weights are measured with a Kern 440-49N scale. This scale has an absolute accuracy of 0.3 gram, [14].

Table 6.2: Weight specifications single sensor sensitive direction

Weight number	Weight	Accuracy interval	Total weight	Accuracy interval
[-]	[gram]	[gram]	[gram]	[gram]
1	100.2	+/- 0.3	100.2	+/- 0.3
2	200.1	+/- 0.3	300.3	+/- 0.3
3	200.0	+/- 0.3	500.3	+/- 0.3
4	200.0	+/- 0.3	700.3	+/- 0.3
5	200.0	+/- 0.3	900.3	+/- 0.3
6	199.8	+/- 0.3	1100.1	+/- 0.3
7	200.2	+/- 0.3	1300.3	+/- 0.3
8	199.8	+/- 0.3	1500.1	+/- 0.3
9	200.1	+/- 0.3	1700.2	+/- 0.3

For the calibration experiments S4-S6, another setup is used than that of S1-S3. In figure 6.6, the setup for S4-S6 is shown. As stated above, the loads are applied with a distance to the force sensor, as this replicated the actual applied load in the complete sensor frame. For this calibration, the weights listed in table 6.3 are used. The weights are applied in the same manner as for calibration S1-S3.

For the sensors non-sensitive direction, the applied load is lower. As 99 percent of the load is directed to the sensitive direction, the sensors non-sensitive direction is only loaded with 0.5 percent of the

full range of the sensor, which means maximum 10 gram. Much smaller weights are therefore used for this direction. To ensure that the sensor is able to measure the difference between the applied weights, weights up to 115 gram are used. In table 6.3, the weights for the single sensors non-sensitive direction are listed, these weights are measured with the Kern 440-49N scale. During the experiments, the measured voltage difference was very low and almost invisible. Therefore, it was first thought that these data were unusable and not all experiments were repeated enough times to achieve the required amount of data points for the confidence interval. During the analysis of all data, it became clear that the data could be used, but for that reason not enough data points were obtained to meet the required data points.

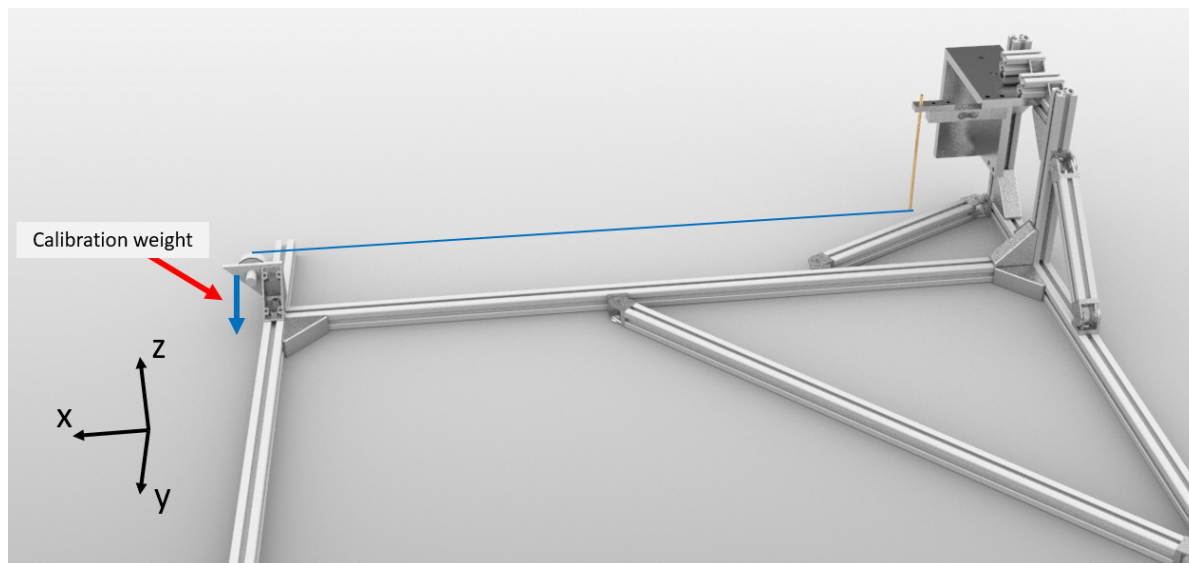


Figure 6.6: Calibration experiment setup for S4-S6, loads applied in the sensor non-sensitive direction K.

Table 6.3: Weight specifications single sensor non-sensitive direction

Weight number [-]	Weight [gram]	Accuracy interval [gram]	Total weight [gram]	Accuracy interval [gram]
1	15.0	+/- 0.3	15.0	+/- 0.3
2	20.0	+/- 0.3	35.0	+/- 0.3
3	20.0	+/- 0.3	55.0	+/- 0.3
4	20.0	+/- 0.3	75.0	+/- 0.3
5	20.0	+/- 0.3	95.0	+/- 0.3
6	20.0	+/- 0.3	115.0	+/- 0.3

The calibration experiments S7-S9 for the second non-sensitive direction (L axis) are comparable with the calibrations of the other non-sensitive direction described above. The calibration setup is shown in figure 6.7. For these experiments, the weights of table 6.3 are again used.

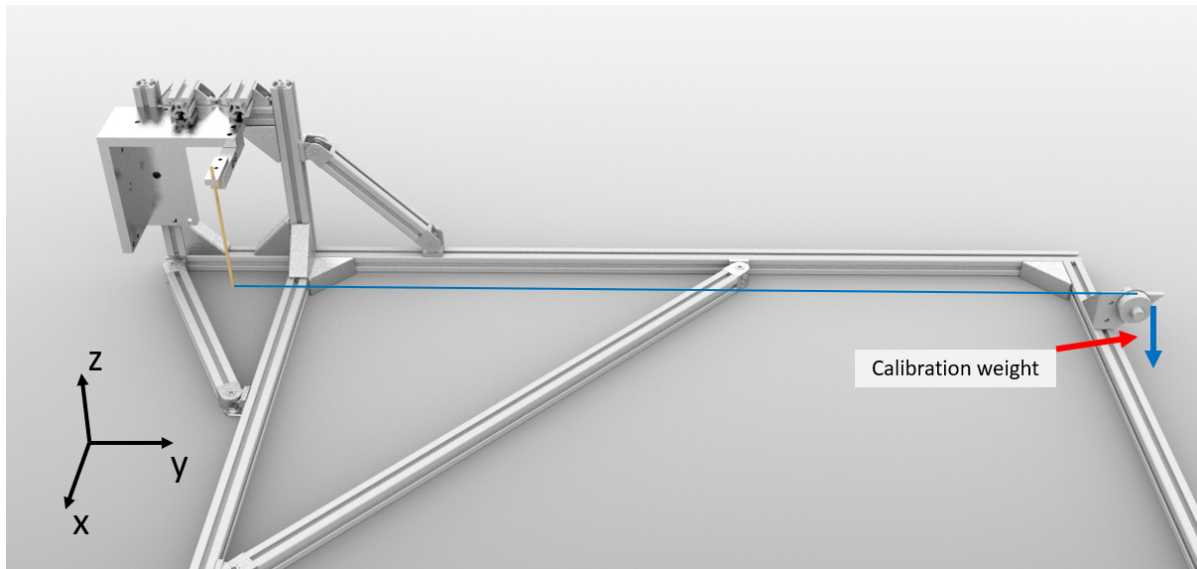


Figure 6.7: Calibration experiment setup for S7-S9, loads applied in the sensor non-sensitive direction L.

#### 6.1.4. Results

After all calibration experiments were performed, the output data was used for the regression analysis. First, the results of the experiments in the sensitive direction are presented. Secondly, the results of the first non-sensitive direction, followed by the other non-sensitive direction and at the end the regression parameters of the single sensors are summarized in a table.

An example of the output data obtained during the experiments with a single sensor in the sensitive direction is shown in figure 6.8. In this figure, the measured output voltage in mV/V is plotted against time in seconds. In this plot, the increase or decrease of weight during the experiment can be observed at the steep slopes, furthermore plateaus can be observed between the steep slopes. During these plateaus, the output voltage is measured for the regression analysis. The time span which is used to determine the averaged output is indicated with green and red vertical lines: green is the start of the time span and red the end of the time span.

In total, 17 data points are obtained out of one experiment (figure 6.8) and for each experiment described in table 6.1, 8 experiments are performed. This results in a total of 136 data points for the regression analysis, which suffice the minimum required data points described in section 6.1.1.

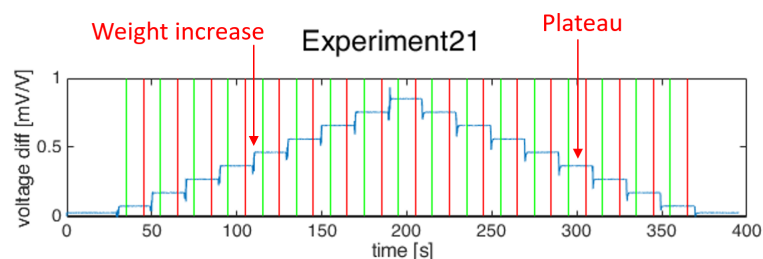
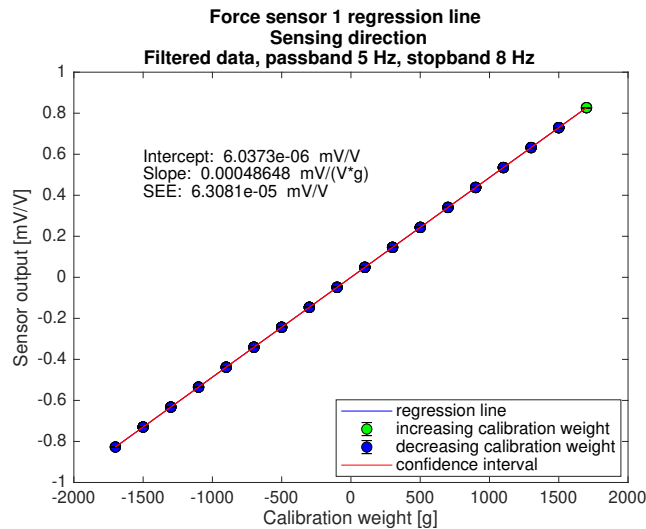
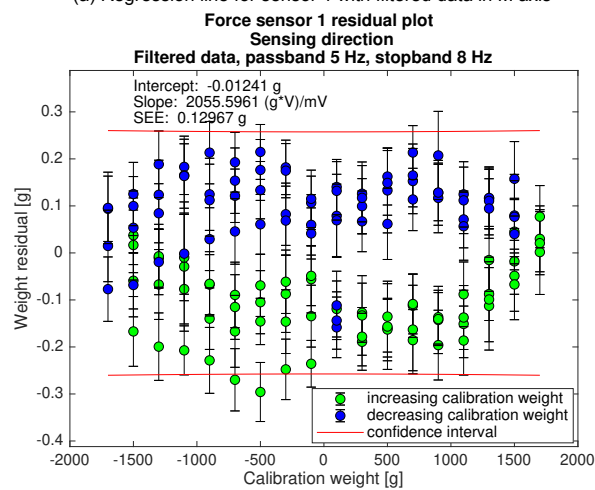


Figure 6.8: Output data experiment 21

First, the results are shown for the regression analysis in the sensitive direction (experiments S1-S3). The regression analysis is performed according section 6.1.1. The results for sensor 1 are shown in this section, results for all three sensors are shown in appendix D.



(a) Regression line for sensor 1 with filtered data in M axis



(b) Residual for sensor 1 with filtered data in M axis

Figure 6.9: Sensor regression analysis results, M axis

The results of the regression analysis for the sensitive direction show that the sensor experiences slight hysteresis. This is observed in figure 6.9b. The data for increasing weight (green points) show a consequent difference from the data for decreasing weight (blue points). The supplier of the sensors indicates a hysteresis of +/- 0.02% FS, in other words +/- 0.4 gram. From figure 6.9b, it can be determined that the hysteresis observed in the calibration experiments falls within this range. Additionally, the output sensitivity (slope) falls within the range determined by the supplier. In the specifications of the supplier, an output sensitivity of 1.0+/-0.15 mV/V is given. In figure 6.9a, the slope is calculated as  $4.86 \cdot 10^{-4}$  mV/(V\*g). Multiplied by the maximum range of the sensor (2000g) gives an output sensitivity of 0.973 mV/V, and this is within the range specified by the supplier. The confidence interval is shown in figure 6.9b with two red lines. In figure 6.9b, it can be seen that the confidence interval is around +/- 0.26g, or +/- 0.013% FS. The supplier indicates an accuracy of +/- 0.02%, thus the force sensor is working properly.

Secondly, the results are shown for the first non-sensitive direction (K axis). The output data of a single experiment is shown in figure 6.10. The output voltage range in this plot is fairly small compared to the voltage range in figure 6.8. For one thing, this is caused by the smaller total weight that is applied, secondly, it could mean that the sensor is less sensitive for this direction. Again, only the results for sensor 1 are shown in this section and the all results are shown in appendix D.

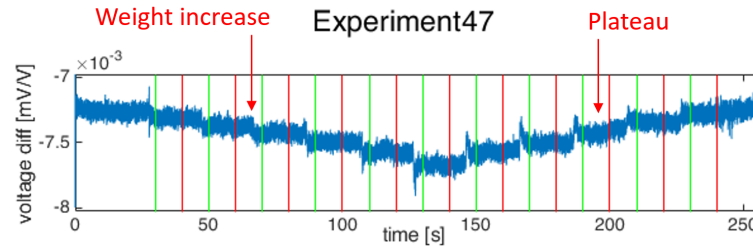
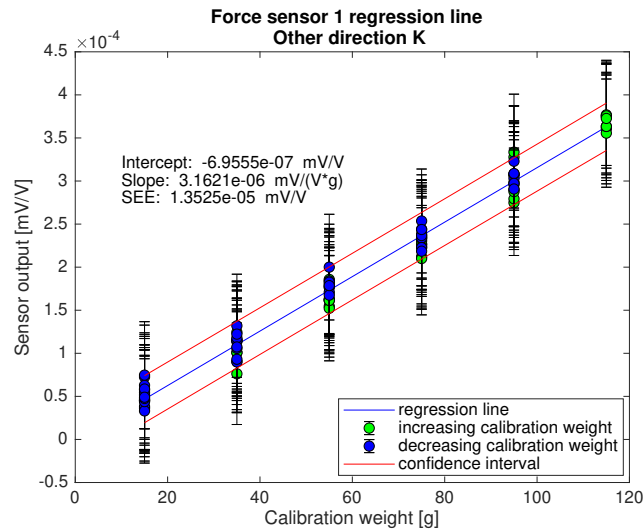
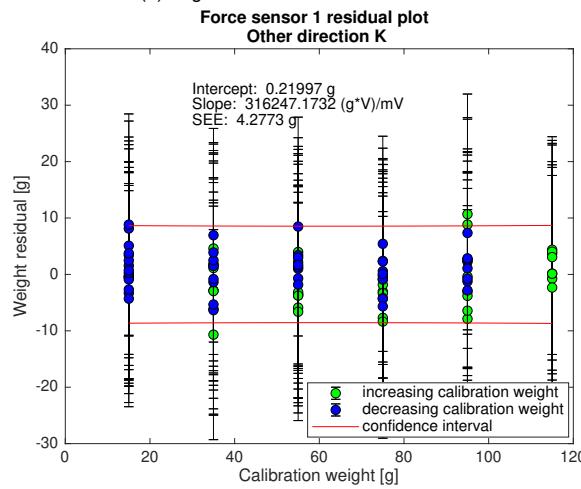


Figure 6.10: Output data experiment 47



(a) Regression line for sensor 1 in K axis



(b) Residual for sensor 1 in K axis

Figure 6.11: Sensor regression analysis results, K axis

In figure 6.11a, the regression line is shown with a slope of  $3.16 \cdot 10^{-6} \text{ mV}/(\text{V} \cdot \text{g})$ . This slope is much smaller than the regression slope in the sensitive direction:  $4.86 \cdot 10^{-4} \text{ mV}/(\text{V} \cdot \text{g}) / 3.16 \cdot 10^{-6} \text{ mV}/(\text{V} \cdot \text{g}) = 154$  times smaller. This means that the sensor is 154 times less sensitive in K axis compared to the M axis. In figure 6.11b, the weight residual in the K axis is around  $\pm 10$  gram, which is relatively high compared to the calibration weights. A high weight residual implies that the uncertainty of the measurement is high. Lastly, it can be observed in figure 6.11b that the interval for each data point is relative large compared to the scatter of the data points, which implies that there is much noise during

the measurement. This can be observed in figure 6.10, where the output signal shows a large continuous noise band compared to the voltage drop caused by applying weights.

Finally, the results are shown for the second non-sensitive direction (L axis). Similar to the results of the other non-sensitive direction, the sensitivity is much lower. In figure 6.12, an example output is shown and in figure 6.13 the results are shown for sensor 1. In appendix D the results are shown for all sensors.

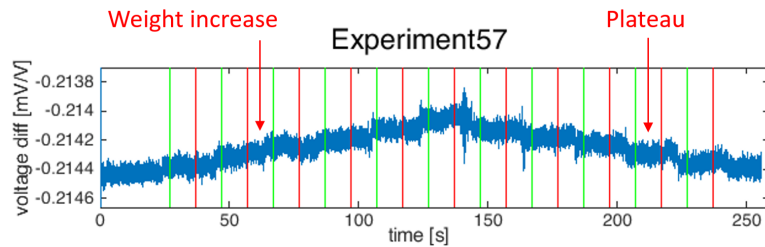
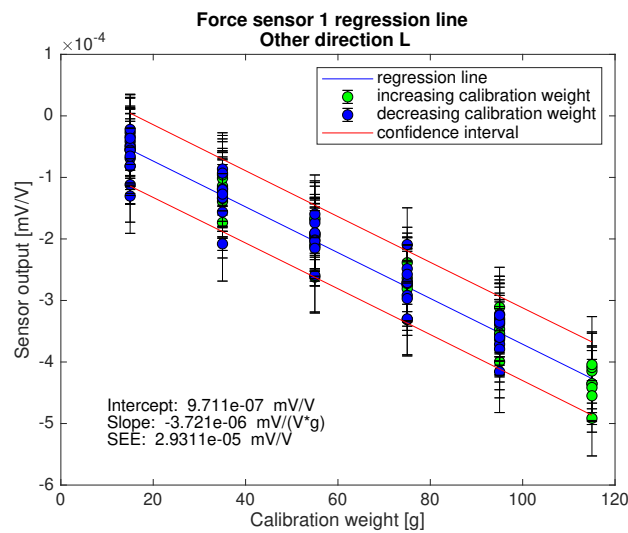
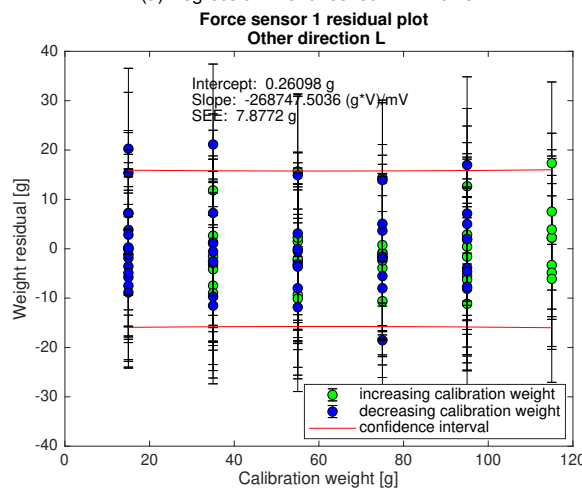


Figure 6.12: Output data experiment 57



(a) Regression line for sensor 1 in L axis



(b) Residual for sensor 1 in L axis

Figure 6.13: Sensor regression analysis results, L axis

With the results shown above, all regression parameters are determined for the sensors. In table 6.4, all single sensor regression slopes are summarized. From this table, it can be seen that the regression slopes of the sensors in the sensitive direction are reasonably close. For the regression slopes in the non-sensitive direction, larger deviations are observed. Especially sensor 3 for the L axis has a fairly small sensitivity. Since these type of sensors are designed to measure forces in only one single direction, it could explain the low sensitivity and the large deviations in the non-sensitive direction. Another important observation is the negative sign of sensor 3 in the K axis. The other two sensors have a positive sign in this direction. In the experimental setup, sensor 1 and 2 are positioned 180 rotated around the K axis relative to sensor 3. The load applied in the calibration experiment is applied at same position, thus sensor 3 experiences a different moment caused by the load. This can clarify the negative sign of sensor 3.

Table 6.4: Single sensor regression slope summary

Sensor	Regression slope		
	Sensitive direction	Non-sensitive direction	
	positive M axis $\cdot 10^{-4}$ [mV/(V*g)]	positive K axis $\cdot 10^{-6}$ [mV/(V*g)]	positive L axis $\cdot 10^{-6}$ [mV/(V*g)]
1	4.86	3.16	3.72
2	5.06	2.67	4.47
3	4.67	-3.31	1.36

## 6.2. Frame calibration upright position

For the second part of the calibration procedure, the complete sensor frame is calibrated. For this part, the sensor frame is calibrated in the upright position see figure 5.7. During this calibration, the sensors are installed in the sensor frame and the performance of the combined sensors are tested. Again the sensitivities of the sensor in all directions are determined with the regression analysis. Before the experiments are performed, the theory described in section 6.1.1 is extended to allow multiple variables in the regression analysis.

### 6.2.1. Theory multi variable sensor

Multi variable calibration is required in case an output signal is dependent on multiple input signals. In this case, the force sensors are dependent on forces in three orthogonal directions. And due to the mutual influences of these sensors, all three sensors depend on the applied forces in three directions. Similar to the calibration of a single variable dependent signal, a data set is required, by which a regression analysis is performed. For a sensor dependent on three variables, the calibration data set can be written as [24]:

$$\begin{pmatrix} Y_1 \\ Y_2 \\ \vdots \\ Y_n \end{pmatrix} = \begin{bmatrix} 1 & X_{11} & X_{12} & X_{13} \\ 1 & X_{21} & X_{22} & X_{23} \\ \vdots & \vdots & \vdots & \vdots \\ 1 & X_{n1} & X_{n2} & X_{n3} \end{bmatrix} \times \begin{pmatrix} \beta_0 \\ \beta_1 \\ \beta_2 \\ \beta_3 \end{pmatrix} \quad (6.11)$$

or

$$\mathbf{Y} = \mathbf{X}\boldsymbol{\beta} \quad (6.12)$$

Where  $Y_n$  is the output signal,  $X_{ni}$  are the input signals,  $\beta_0$  is the intercept and  $\beta_{1,2,3}$  are the regression slopes.

From these expressions, the regression parameter vector  $\boldsymbol{\beta}$  can be approximated in a similar approach as used for the single variable regression analysis, section 6.1.1. For the sensor frame of this project, these equations are not enough to describe the working principle, therefore the theory is extended in the next section.

### 6.2.2. Extended theory multi variable

In the previous section, the multi variable regression analysis is elaborated. For the sensor developed in this project, a total of three force sensors are combined, which means that there are three output

variables. To apply the multi variable regression analysis on this sensor, the calibration expression should be expanded to an equation with three output variables. The expanded expression is shown in equation 6.13:

$$\begin{bmatrix} Y_{11} & Y_{12} & Y_{13} \\ Y_{21} & Y_{22} & Y_{23} \\ \vdots & \vdots & \vdots \\ Y_{n1} & Y_{n2} & Y_{n3} \end{bmatrix} = \begin{bmatrix} 1 & X_{11} & X_{12} & X_{13} \\ 1 & X_{21} & X_{22} & X_{23} \\ \vdots & \vdots & \vdots & \vdots \\ 1 & X_{n1} & X_{n2} & X_{n3} \end{bmatrix} \times \begin{bmatrix} \beta_{01} & \beta_{02} & \beta_{03} \\ \beta_{11} & \beta_{12} & \beta_{13} \\ \beta_{21} & \beta_{22} & \beta_{23} \\ \beta_{31} & \beta_{32} & \beta_{33} \end{bmatrix} \quad (6.13)$$

Where  $Y_{ni}$  are the output signals in mV/V,  $X_{ni}$  are the input signals in gram,  $\beta_{0i}$  are the intercepts in mV/V and  $\beta_{ni,ni,ni}$  are the regression slopes in mV/V/gram.

As can be seen in the equation above, the regression parameters  $\beta$  are expanded from a vector into a matrix, the calibration matrix. The calibration matrix of this sensor translates the applied weights in different directions into the output signal in mV/V.

As a matter of fact, the expanded regression analysis, is the multi variable regression analysis repeated three times. For each output signal  $Y$ , the regression parameters are determined with the use of all input signals  $X$ . Therefore, the first column of the calibration matrix is estimated with the first column  $Y_{n1}$  etc.

### 6.2.3. Calibration setup frame

For the sensor setup it is now clear what calibration data is required. For the full upright frame, loads should be applied in the range of the sensor frame to determine the sensitivity of the sensor in all directions. To obtain this data, a calibration setup is designed that is able to perform all calibration experiments. The requirements of this calibration setup are:

- Position the sensor frame in the upright position
- Ability to apply loads in three orthogonal directions
- Alignment of the calibration setup with the sensor frame

The calibration setup for the sensor frame is shown in figure 6.14. This frame consists of ITEM 20x20 profiles. With this setup, three orthogonal loads can be applied at the same time on the sensor. The setup is clamped onto a horizontal table. The sensor frame is attached to a vertical support, and with two small profiles at the top, the sensor frame is aligned with the calibration setup in the upright position, figure 6.15. The loads are applied with the use of weights in three orthogonal directions. A total of three wires are connected to the connection block. The first weight is directly attached to the sensor frame with a wire. The other two weights are attached to the sensor frame guided by two pulleys. With the use of drawings, the pulleys are aligned with the sensor frame to ensure the loads are applied in orthogonal directions. The pulleys are fabricated of light weight plastic bearings with a slot milled to guide the wire. This calibration setup is used for the calibration experiments of the single sensor for the non-sensitive direction too.

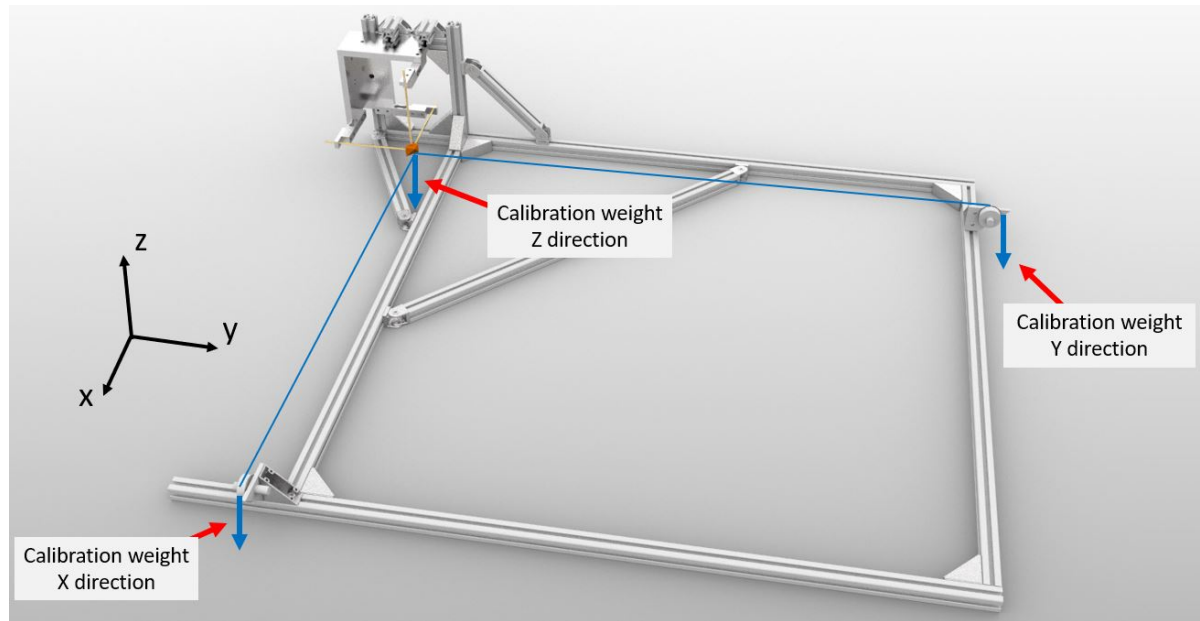


Figure 6.14: Rendered image of the calibration setup for the complete sensor frame

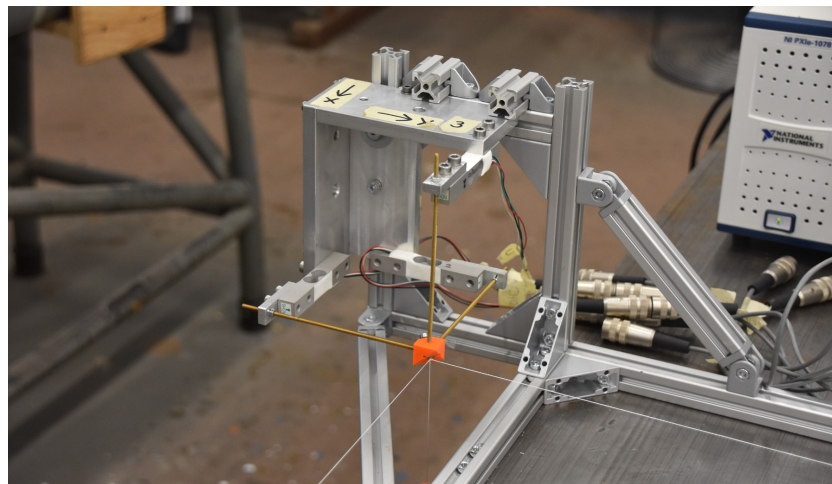


Figure 6.15: Sensor positioned in the upright position

#### 6.2.4. Calibration experiments

For the calibration of the sensor frame, only one type of calibration experiment is required. To obtain the data, weights should be applied simultaneously on the sensor in three orthogonal directions. In table 6.5, the experiment group is shown including a reference number. More detailed information of each experiment can be found in table G.1.

Table 6.5: Calibration experiments for sensor frame in upright position with reference number

Calibration reference number	Type of calibration experiment	Force sensor	Experiment numbers
C1	Complete sensor frame upright position	1,2,3	111-113,115-147

Calibration C1 is shown in figure 6.16. For this calibration group, the sensor frame is attached to the calibration setup. During the experiments, weights are applied on the sensor in three orthogonal directions. The weights in table 6.2 are used to apply loads in the V or Y direction. Next to this weight stack, two other weight stacks are used. To apply loads in the U or X direction the weights in table 6.6

are used and for the W or Z direction, the weight of table 6.7 are used. These weights are measured with the Kern 440-49N scale as well.

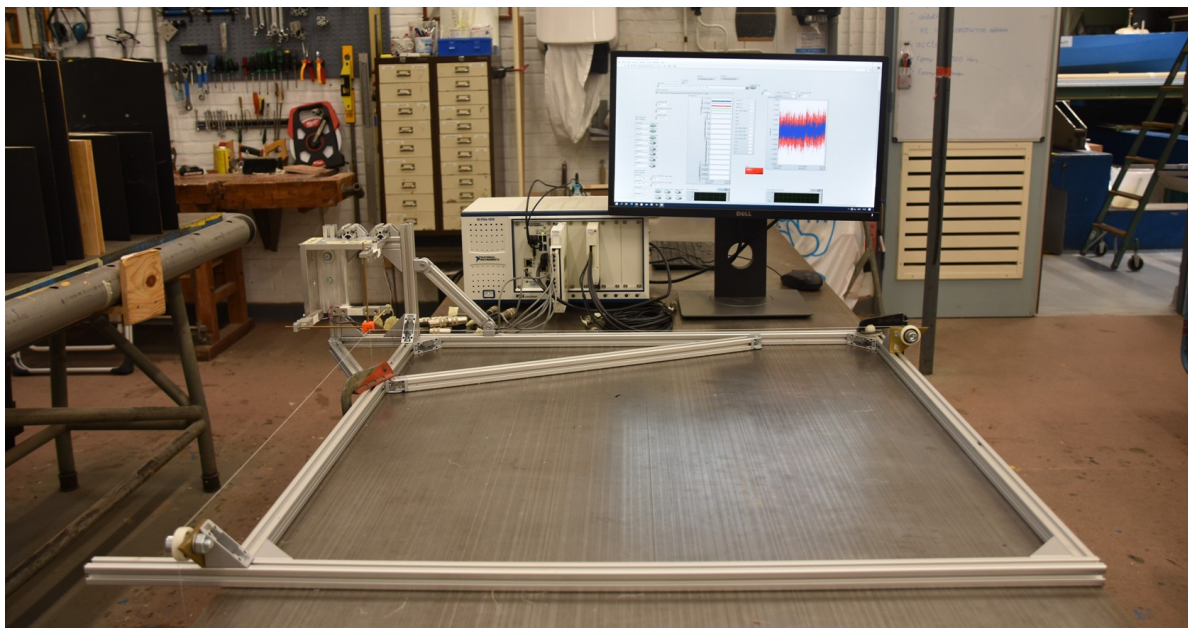


Figure 6.16: Calibration setup C1

Table 6.6: Weight specifications X axis (blue weights)

Weight number [–]	Weight [gram]	Accuracy interval [gram]	Total weight [gram]	Accuracy interval [gram]
1	242.2	+/- 0.3	258.6	+/- 0.3
2	242.4	+/- 0.3	501.0	+/- 0.3
3	237.3	+/- 0.3	738.3	+/- 0.3
4	239.3	+/- 0.3	978.2	+/- 0.3
5	245.6	+/- 0.3	1223.7	+/- 0.3
6	240.5	+/- 0.3	1464.0	+/- 0.3
7	236.5	+/- 0.3	1700.5	+/- 0.3

Table 6.7: Weight specifications Z axis (yellow weights)

Weight number [–]	Weight [gram]	Accuracy interval [gram]	Total weight [gram]	Accuracy interval [gram]
1	245.4	+/- 0.3	262.9	+/- 0.3
2	238.9	+/- 0.3	501.7	+/- 0.3
3	240.5	+/- 0.3	742.3	+/- 0.3
4	239.6	+/- 0.3	981.9	+/- 0.3
5	242.3	+/- 0.3	1224.2	+/- 0.3
6	242.6	+/- 0.3	1467.2	+/- 0.3
7	246.8	+/- 0.3	1714.0	+/- 0.3

In total, 36 experiments are performed, where different weight combinations are used for each experiment. The range of the sensor consists of a 3D cube and to perform experiments in this complete space, several weight combinations should be applied. In figure 6.17, the outer working range of the sensor is plotted in red. In this figure, the markers present the data points where the sensor is tested during the calibration experiments.

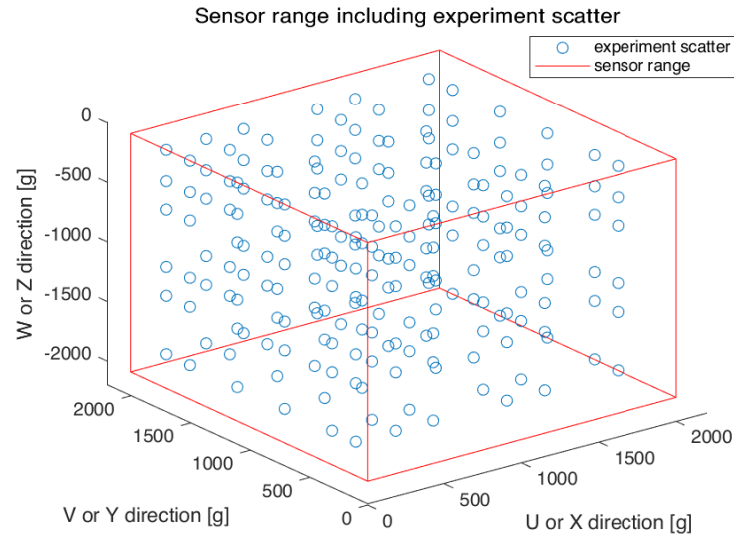


Figure 6.17: Sensor range plotted with the experimental data scatter

### 6.2.5. Verification of calculation calibration matrix

To verify that the calculation for the calibration matrix is working properly, a fictional example is tested of which the calibration matrix result is known. First, the fictional example results are structured as equation 6.13. Each row represents a single data point, with the measured voltage of the three sensors and the applied weight in three orthogonal directions. In equation 6.14, the example data is shown.

$$\begin{bmatrix} 0.005 \text{ mV/V} & 0.005 \text{ mV/V} & 0.99 \text{ mV/V} \\ 0.01 \text{ mV/V} & 0.01 \text{ mV/V} & 1.98 \text{ mV/V} \\ 0.99 \text{ mV/V} & 0.005 \text{ mV/V} & 0.005 \text{ mV/V} \\ 1.98 \text{ mV/V} & 0.01 \text{ mV/V} & 0.01 \text{ mV/V} \\ 0.005 \text{ mV/V} & 0.99 \text{ mV/V} & 0.005 \text{ mV/V} \\ 0.01 \text{ mV/V} & 1.98 \text{ mV/V} & 0.01 \text{ mV/V} \end{bmatrix} = \begin{bmatrix} 1 & 0 \text{ g} & 0 \text{ g} & 1 \text{ g} \\ 1 & 0 \text{ g} & 0 \text{ g} & 2 \text{ g} \\ 1 & 1 \text{ g} & 0 \text{ g} & 0 \text{ g} \\ 1 & 2 \text{ g} & 0 \text{ g} & 0 \text{ g} \\ 1 & 0 \text{ g} & 1 \text{ g} & 0 \text{ g} \\ 1 & 0 \text{ g} & 2 \text{ g} & 0 \text{ g} \end{bmatrix} \times \begin{bmatrix} \beta_{01} & \beta_{02} & \beta_{03} \\ \beta_{11} & \beta_{12} & \beta_{13} \\ \beta_{21} & \beta_{22} & \beta_{23} \\ \beta_{31} & \beta_{32} & \beta_{33} \end{bmatrix} \quad (6.14)$$

For the first data point of the fictional data only a load is applied in the Z direction with a magnitude 1g and the three sensors measure a voltage of 0.005mV/V, 0.005mV/V and 0.99mV/V. The fictional measured voltage are determined by the structural behaviour of the sensor explained in 6.3.1. In total, 6 data points are used for this example calculation, each data point presents a load applied in a single direction. With the fictional data, the calibration matrix is calculated with equation 6.7. The resulting calibration matrix is shown in equation 6.15, and this matrix is as expected. The values of the first row, intercepts, are close to zero and the regression slope parameters are according to the load distribution over the three force sensors, eq. 6.21. For this example, misalignment and other effects in the sensor are neglected, therefore the structural behaviour matrix was expected. Thus, it is concluded that the data processing is working correct.

$$\begin{bmatrix} \beta_{01} & \beta_{02} & \beta_{03} \\ \beta_{11} & \beta_{12} & \beta_{13} \\ \beta_{21} & \beta_{22} & \beta_{23} \\ \beta_{31} & \beta_{32} & \beta_{33} \end{bmatrix} = \begin{bmatrix} 5.55 \cdot 10^{-16} \text{ mV/V} & 5.55 \cdot 10^{-16} \text{ mV/V} & 5.55 \cdot 10^{-16} \text{ mV/V} \\ 0.99 \text{ mV}/(\text{V} * \text{g}) & 0.005 \text{ mV}/(\text{V} * \text{g}) & 0.005 \text{ mV}/(\text{V} * \text{g}) \\ 0.005 \text{ mV}/(\text{V} * \text{g}) & 0.99 \text{ mV}/(\text{V} * \text{g}) & 0.005 \text{ mV}/(\text{V} * \text{g}) \\ 0.005 \text{ mV}/(\text{V} * \text{g}) & 0.005 \text{ mV}/(\text{V} * \text{g}) & 0.99 \text{ mV}/(\text{V} * \text{g}) \end{bmatrix} \quad (6.15)$$

### 6.2.6. Results

After all the calibration experiments were performed, the data was used for the regression analysis. The output data for the calibration experiments of the sensor frame consists of three measured voltages, one for each force sensor. In figure 6.18, an example of the output data obtained from the calibration experiments is shown. In this figure, it can be seen that at 25 seconds a weight is applied in the vertical W direction and at 35 seconds a weight in the U axis is applied. After these weights are applied, the

weights in last axis (V axis) are stacked and removed. In the output data plot it is clear that each sensor is in line with an applied weight, as a single output variable reacts to an applied weight. If we zoom in at the moment that a weight is applied, mutual influences can be observed. An example is shown in figure 6.19, at around 25 seconds a weight is applied in the W direction. From this plot it can be observed that sensor 1 and 2 also change slightly due to this weight addition.

In total, 36 experiments are performed similar as figure 6.18 in order to obtain all the data points shown in figure 6.17. One experiment defines 11 data points as shown in figure 6.18, thus a total of 396 data points are obtained.

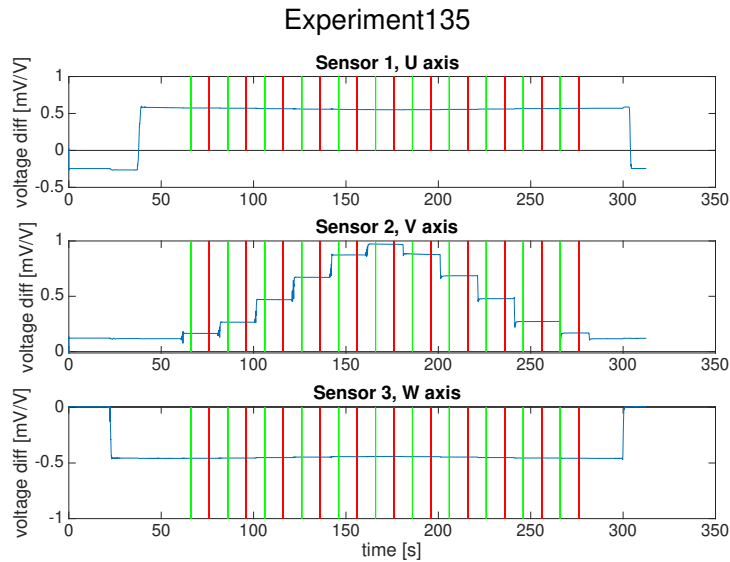


Figure 6.18: Output data experiment 135

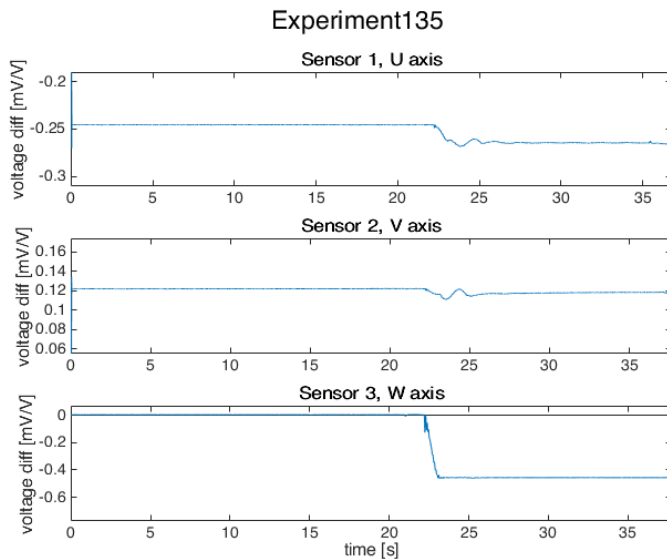


Figure 6.19: Output data experiment 135, zoom in with mutual influence

From the collected data, the data points are determined by averaging the measured voltage at the plateaus (between the vertical green and red lines in figure 6.18). With the data set collected, the regression analysis is performed according to the extended multi variable regression analysis described in section 6.2.2. The data set is inserted in equation 6.13. A short example is shown in equation 6.16.

$$\begin{bmatrix} -0.0013 \text{ mV/V} & 0.050 \text{ mV/V} & 0.0009 \text{ mV/V} \\ -0.0039 \text{ mV/V} & 0.150 \text{ mV/V} & 0.0029 \text{ mV/V} \\ -0.0091 \text{ mV/V} & 0.358 \text{ mV/V} & 0.0071 \text{ mV/V} \\ -0.0133 \text{ mV/V} & 0.560 \text{ mV/V} & 0.0107 \text{ mV/V} \\ \vdots & \vdots & \vdots \\ Y_{n1} & Y_{n2} & Y_{n3} \end{bmatrix} = \begin{bmatrix} 1 & 0 \text{ g} & 100.2 \text{ g} & 0 \text{ g} \\ 1 & 0 \text{ g} & 300.3 \text{ g} & 0 \text{ g} \\ 1 & 0 \text{ g} & 700.3 \text{ g} & 0 \text{ g} \\ 1 & 0 \text{ g} & 1100.1 \text{ g} & 0 \text{ g} \\ \vdots & \vdots & \vdots & \vdots \\ 1 & X_{n1} & X_{n2} & X_{n3} \end{bmatrix} \times \begin{bmatrix} \beta_{01} & \beta_{02} & \beta_{03} \\ \beta_{11} & \beta_{12} & \beta_{13} \\ \beta_{21} & \beta_{22} & \beta_{23} \\ \beta_{31} & \beta_{32} & \beta_{33} \end{bmatrix} \quad (6.16)$$

From this analysis, the calibration matrix is obtained. As this is a full matrix, it is not possible to visualize these data in regression line plots as done for the single sensor regression analysis. The obtained calibration matrix is shown in equation 6.17.

$$\text{Calibration matrix} = \begin{bmatrix} 0.0030 \text{ mV/V} & 0.0038 \text{ mV/V} & -0.0014 \text{ mV/V} \\ 4.96 \cdot 10^{-4} \text{ mV/(V * g)} & -2.18 \cdot 10^{-6} \text{ mV/(V * g)} & -8.93 \cdot 10^{-7} \text{ mV/(V * g)} \\ -1.08 \cdot 10^{-5} \text{ mV/(V * g)} & 5.07 \cdot 10^{-4} \text{ mV/(V * g)} & 9.20 \cdot 10^{-6} \text{ mV/(V * g)} \\ 2.09 \cdot 10^{-5} \text{ mV/(V * g)} & 6.17 \cdot 10^{-6} \text{ mV/(V * g)} & 4.69 \cdot 10^{-4} \text{ mV/(V * g)} \end{bmatrix} \quad (6.17)$$

An approach to examine how well the calibration matrix is determined, is to investigate the residuals. For the regression matrix there are two ways to investigate the residuals. First, to investigate the residual of the measured output voltage.

$$\text{res}_y = Y - Y_d \quad (6.18)$$

In this equation,  $Y$  is the measured output voltage and  $Y_d$  is the calculated output voltage from the applied weight times the calibration matrix.

The second method is the residual of the applied weight.

$$\text{res}_x = \frac{\text{res}_y}{\sqrt{\beta_{1,i}^2 + \beta_{2,i}^2 + \beta_{3,i}^2}} \quad (6.19)$$

In this equation,  $\text{res}_y$  is the residual of the output voltage and  $\sqrt{\beta_{1-3,i}^2}$  is the square root of the summation of each column to the power two.

The results of the output voltage and weight residuals are plotted in figure 6.20 and 6.21 respectively.

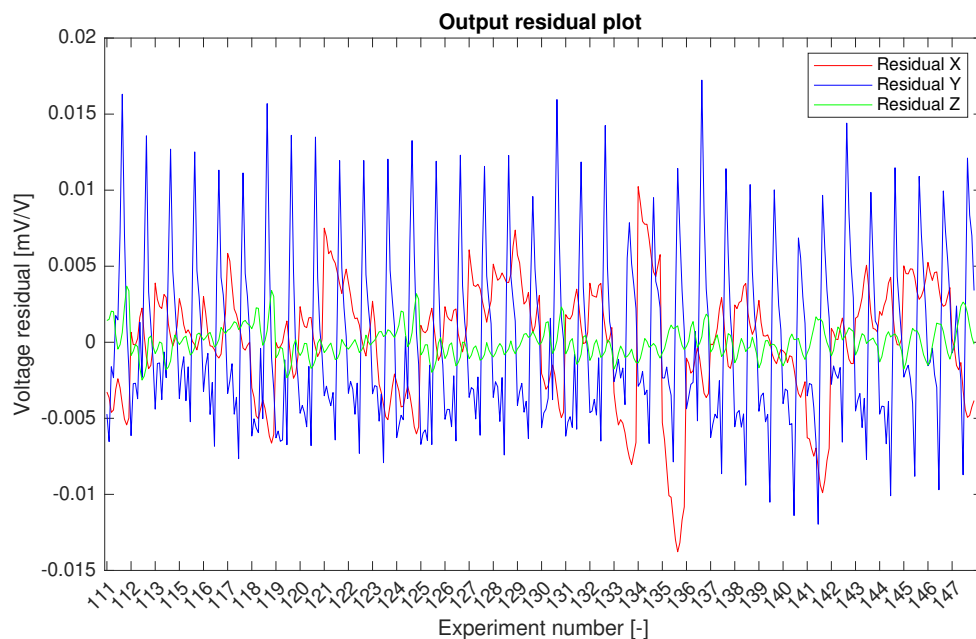


Figure 6.20: Residual plot of measured output voltage of upright sensor frame from eq. 6.19

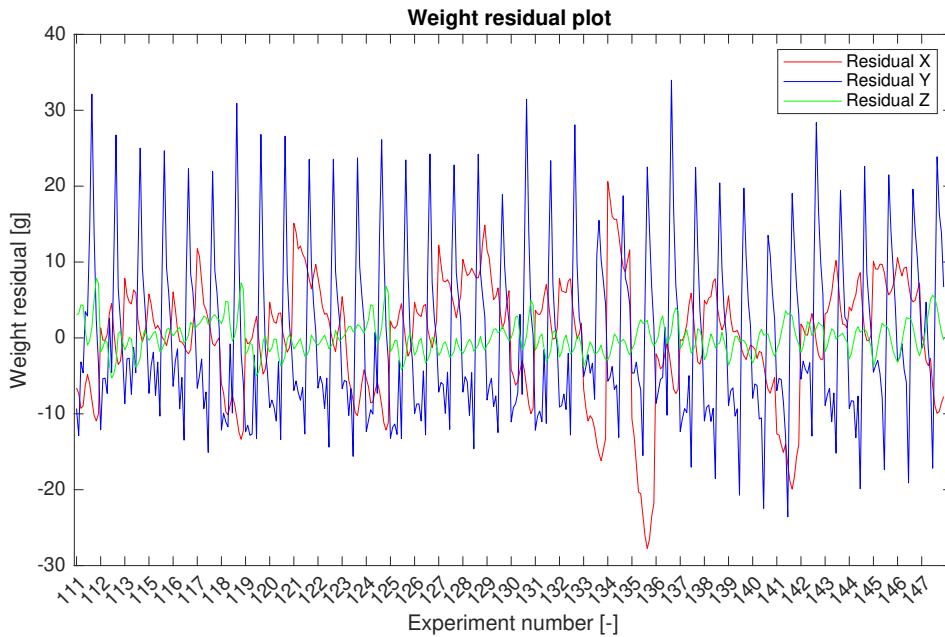


Figure 6.21: Residual plot of applied weight on upright sensor frame from eq. 6.18

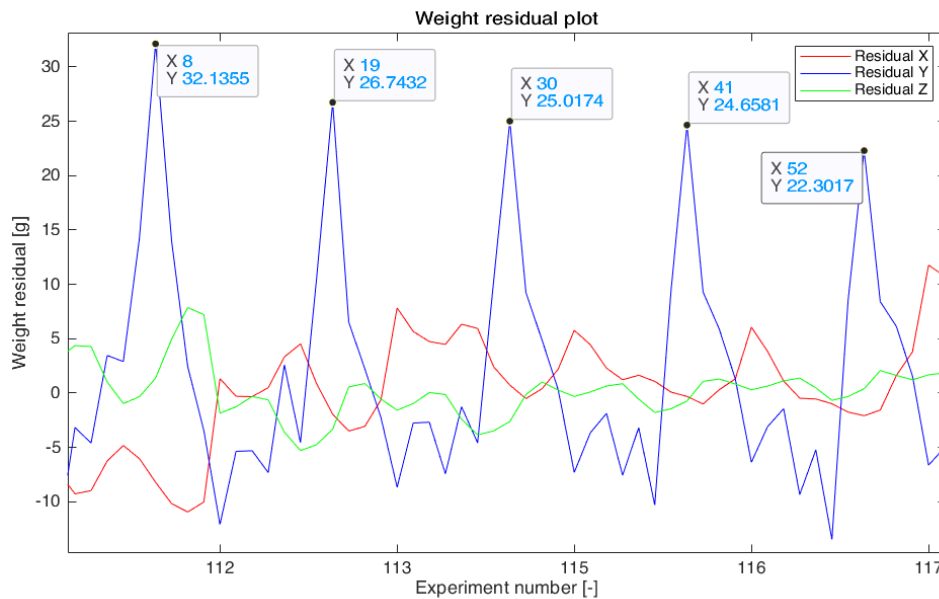


Figure 6.22: Residual plot of applied weight on upright sensor frame, periodic residual Y zoomed in

From the residual plots, it can be seen that the weight residual greatly corresponds with the residual of the output voltage in that specific direction. That could be the case, as the force sensors are sensitive in their sensitive direction and less in the non-sensitive directions. Furthermore, it can be seen that for both figures the residual range of Z is smaller than the residual ranges of X and Y. To evaluate the residuals from a physical point of view, the second figure (figure 6.21) is used as this figure shows the physical error of the load in gram. The weight residual of Z has a maximum of 8g and the maximum weight residual of X and Y is 28g and 34g respectively. The residual of Y shows a clear periodic repetition and residual X shows a repetition too. In figure 6.22, the periodic repetition is shown for the residual of Y. In this plot, the peak values of the residual Y are indicated. The peak value repeats every eleven x values. As from each experiment a total of 11 data points are obtained, this corresponds to

a length of a single experiment. If we look closer into a single experiment, it can be noticed that the weight in the Y direction is stacked and removed in a single experiment. The periodicity of the residual X is shown in figure 6.23. With red dashed lines, the periods are indicated. In a single experiment, the weight in X direction is kept constant, however the weight in X direction is completely stacked in a period indicated between the red dashed lines.

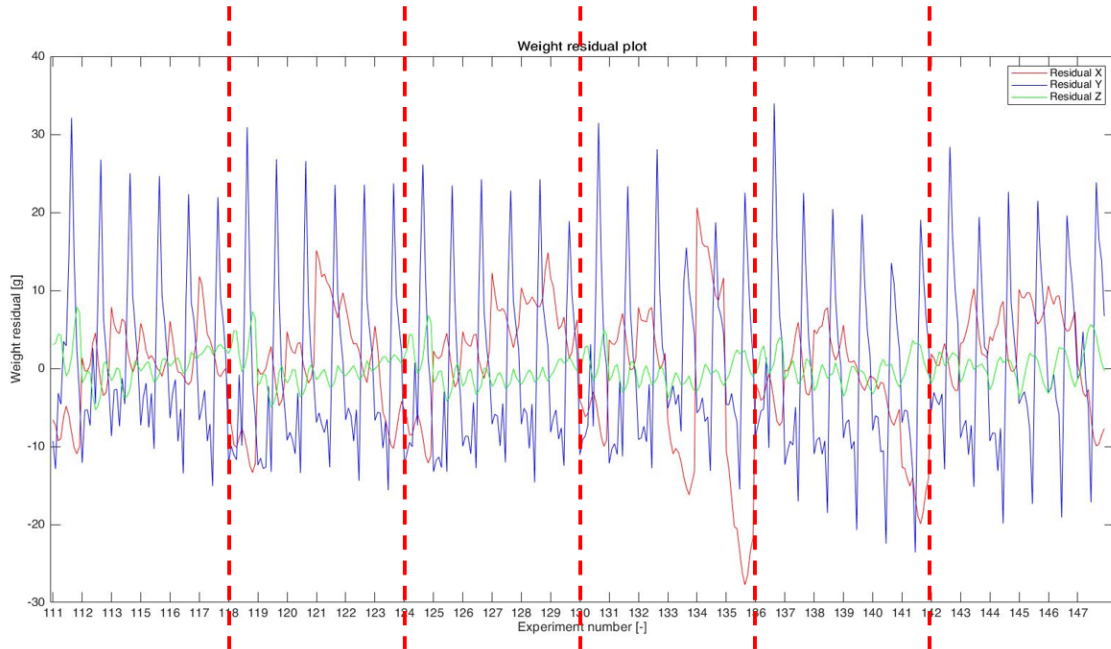


Figure 6.23: Residual plot of applied weight on upright sensor frame, periodic residual X (red dashed lines)

### 6.3. Comparison calibration matrices upright position

With the experiments described above, data about the individual force sensors and the sensor frame are obtained. With this data, different methods can now be applied to obtain the calibration matrix of the sensor frame. First, the theoretical calibration matrix is obtained with the individual sensor characteristics. Secondly, the calibration matrix is obtained with the individual sensor characteristics and sensor frame. Finally, the full upright calibration matrix found in section 6.2.6 is described. After these three calibration matrices are obtained, the matrices are compared and the performance of the matrices are tested.

#### 6.3.1. Theoretical calibration matrix

After the calibration experiments are performed and the regression matrices are determined, it should be checked whether these obtained regression matrices are as expected. The regression matrices can be compared with the theoretical regression matrix.

The theoretical regression matrix is determined with the structural behaviour of the sensor as well as the regression parameters of the sensors. With the structural behaviour of the sensor, mutual influences of the sensors are taken into account. The theoretical regression matrix can be determined with the following equation:

$$\underbrace{\begin{bmatrix} \beta_{11} & \beta_{12} & \beta_{13} \\ \beta_{21} & \beta_{22} & \beta_{23} \\ \beta_{31} & \beta_{32} & \beta_{33} \end{bmatrix}}_{\text{theoretical regression matrix}} = \underbrace{\begin{bmatrix} struc_{11} & struc_{12} & struc_{13} \\ struc_{21} & struc_{22} & struc_{23} \\ struc_{31} & struc_{32} & struc_{33} \end{bmatrix}}_{\text{structural behaviour}} \circ \underbrace{\begin{bmatrix} \beta_{1m} & \beta_{2k} & \beta_{3k} \\ \beta_{1k} & \beta_{2m} & \beta_{3l} \\ \beta_{1l} & -\beta_{2l} & \beta_{3m} \end{bmatrix}}_{\text{regression parameters}} \quad (6.20)$$

The structural matrix and regression parameters are multiplied with the Hadamard product or element wise multiplication. Furthermore, it can be observed that the first row (intercept values) of the

calibration matrix is omitted. Only the slope regression parameters are determined for the theoretical regression matrix as this analysis is exact and does not involve estimations.

The structural behaviour matrix is determined by the mutual influences of the force sensors. During the design of the sensor setup, it was determined what length was required to ensure that 99 percent of the force is taken by a sensor in its sensitive direction. The last 1 percent is divided over the two other sensors equally, 0.5 percent each. In the structural matrix, each row represents a force sensor and each column represents a force parallel to an axis. As the sensor frame is symmetrical, each force is distributed identically over the force sensors. This results in the structural matrix:

$$\text{structural matrix} = \begin{bmatrix} 0.99 & 0.005 & 0.005 \\ 0.005 & 0.99 & 0.005 \\ 0.005 & 0.005 & 0.99 \end{bmatrix} \quad (6.21)$$

The regression parameters matrix consists of all single force sensor regression parameters listed in table 6.4. Each force sensor should be calibrated for the sensitivity in the sensitive direction (M axis) and the two other non-sensitive directions (K,L axis). In figure 6.24, the orientation of the force sensor axis system (K,L,M) with respect to the frame axis system (U,V,W) is shown.

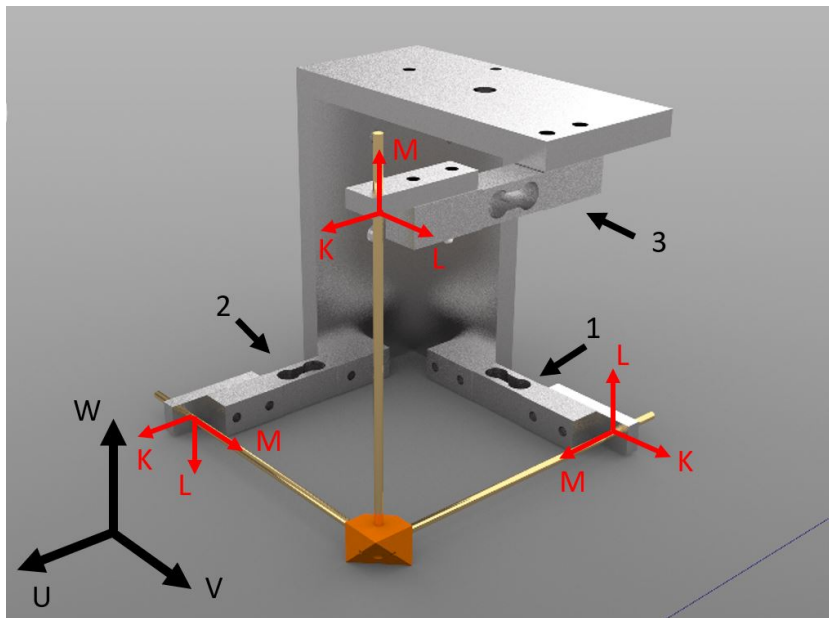


Figure 6.24: Sensor frame with local axis system of the three force sensors

Each column in the matrix with regression parameters (eq. 6.22) presents the sensitivity of a single force sensor in its three direction. Only for sensor 2 the L axis is in the negative direction of the frame axis system (U,V,W).

From table 6.4, the single sensor regression parameters can be obtained. This results in the following theoretical calibration matrix:

$$\underbrace{\begin{bmatrix} 0.99 & 0.005 & 0.005 \\ 0.005 & 0.99 & 0.005 \\ 0.005 & 0.005 & 0.99 \end{bmatrix}}_{\text{structural behaviour}} \circ \underbrace{\begin{bmatrix} 4.86 \cdot 10^{-4} \text{ mV}/(\text{V} * g) & 2.67 \cdot 10^{-6} \text{ mV}/(\text{V} * g) & -3.31 \cdot 10^{-6} \text{ mV}/(\text{V} * g) \\ 3.16 \cdot 10^{-6} \text{ mV}/(\text{V} * g) & 5.06 \cdot 10^{-4} \text{ mV}/(\text{V} * g) & 1.36 \cdot 10^{-6} \text{ mV}/(\text{V} * g) \\ 3.72 \cdot 10^{-6} \text{ mV}/(\text{V} * g) & -4.47 \cdot 10^{-6} \text{ mV}/(\text{V} * g) & 4.67 \cdot 10^{-4} \text{ mV}/(\text{V} * g) \end{bmatrix}}_{\text{regression parameters}} \\ = \begin{bmatrix} 4.81 \cdot 10^{-4} \text{ mV}/(\text{V} * g) & 1.35 \cdot 10^{-8} \text{ mV}/(\text{V} * g) & -1.66 \cdot 10^{-8} \text{ mV}/(\text{V} * g) \\ 1.58 \cdot 10^{-8} \text{ mV}/(\text{V} * g) & 5.00 \cdot 10^{-4} \text{ mV}/(\text{V} * g) & 6.79 \cdot 10^{-8} \text{ mV}/(\text{V} * g) \\ 1.96 \cdot 10^{-8} \text{ mV}/(\text{V} * g) & -2.24 \cdot 10^{-8} \text{ mV}/(\text{V} * g) & 4.62 \cdot 10^{-4} \text{ mV}/(\text{V} * g) \end{bmatrix} \quad (6.22)$$

### 6.3.2. Single sensor calibration matrix

The first estimation of the calibration matrix is determined with the single sensor regression parameters. With this method, the regression parameters of the single sensors are used and a multiplication factor is determined for the sensors in the frame. This multiplication number is determined by the difference between the output signals for a single sensor and the complete sensor. In case a certain weight is applied in the sensors' sensitive direction, the single sensor will give a different output signal than the same sensor in the combined sensor. An important assumption of this method is that the mutual influence of input parameters are neglected. Which means that the regression matrix is approximated only with the weights directly in line with the sensitive direction of the sensors. Therefore, the calibration matrix for this option will consist of a diagonal matrix. The multiplication factor is determined with:

$$a_f = \frac{y_m}{r_s * W} \quad (6.23)$$

In this equation,  $a_f$  is the multiplication factor,  $y_m$  is the measured output voltage of a single sensor in the sensor frame,  $r_s$  is the regression slope determined for an individual force sensor (table 6.4) and  $W$  is the applied weight used to determine  $y_m$ .

The method to determine the multiplication factor is an estimation, therefore this method is performed for a total of 5 different weights after which an average multiplication factor is determined for each sensor. In table 6.8, the multiplication factors are shown. In equation 6.24 the calibration matrix is calculated with the multiplications factors and the sensor regression parameters.

Sensor	Multiplication factor [-]
1	1.0403
2	1.0046
3	1.0091

Table 6.8: Approximation of the multiplication factors for single sensor calibration matrix

$$\begin{array}{c}
 \left[ \begin{array}{ccc}
 6.04 \cdot 10^{-6} \text{ mV/V} & -2.87 \cdot 10^{-5} \text{ mV/V} & 5.98 \cdot 10^{-5} \text{ mV/V} \\
 4.86 \cdot 10^{-4} \text{ mV/(V * g)} & 0 & 0 \\
 0 & 5.06 \cdot 10^{-4} \text{ mV/(V * g)} & 0 \\
 0 & 0 & 4.67 \cdot 10^{-4} \text{ mV/(V * g)}
 \end{array} \right] \circ \left[ \begin{array}{ccc}
 1.0403 & 1.0046 & 1.0091 \\
 1.0403 & 0 & 0 \\
 0 & 1.0046 & 0 \\
 0 & 0 & 1.0091
 \end{array} \right] \\
 \text{Single sensor regression slope} \qquad \qquad \qquad \text{Multiplication factors} \\
 = \left[ \begin{array}{ccc}
 6.28 \cdot 10^{-6} \text{ mV/V} & -2.88 \cdot 10^{-5} \text{ mV/V} & 6.04 \cdot 10^{-5} \text{ mV/V} \\
 5.06 \cdot 10^{-4} \text{ mV/(V * g)} & 0 & 0 \\
 0 & 5.08 \cdot 10^{-4} \text{ mV/(V * g)} & 0 \\
 0 & 0 & 4.71 \cdot 10^{-4} \text{ mV/(V * g)}
 \end{array} \right] \\
 (6.24)
 \end{array}$$

### 6.3.3. Full upright calibration matrix

The full upright calibration matrix is determined in equation 6.17. This matrix is calculated directly from the calibration experiments. Mutual influences are taken into account for this calibration matrix as well as the intercepts.

### 6.3.4. Calibration matrices comparison upright position

For the sensor frame, two calibration matrices are estimated with the use of calibration experiments. A third calibration matrix is determined with the sensor characteristics and sensor structure. Below, these three calibrations matrices are presented once more. The theoretical calibration matrix is determined in section 6.3.1, the single sensor calibration matrix in section 6.3.2 and the full upright calibration matrix in section 6.2.6.

$$\textit{Theoretical calibration matrix} = \begin{bmatrix} 4.81 \cdot 10^{-4} & 1.35 \cdot 10^{-8} & -1.66 \cdot 10^{-8} \\ 1.58 \cdot 10^{-8} & 5.00 \cdot 10^{-4} & 6.79 \cdot 10^{-8} \\ 1.96 \cdot 10^{-8} & -2.24 \cdot 10^{-8} & 4.62 \cdot 10^{-4} \end{bmatrix} \quad (6.25)$$

$$\textit{Single sensor calibration matrix} = \begin{bmatrix} 6.28 \cdot 10^{-6} & -2.88 \cdot 10^{-5} & 6.04 \cdot 10^{-5} \\ 5.06 \cdot 10^{-4} & 0 & 0 \\ 0 & 5.08 \cdot 10^{-4} & 0 \\ 0 & 0 & 4.71 \cdot 10^{-4} \end{bmatrix} \quad (6.26)$$

$$\textit{Full upright calibration matrix} = \begin{bmatrix} 0.0030 & 0.0038 & -0.0014 \\ 4.96 \cdot 10^{-4} & -2.18 \cdot 10^{-6} & -8.93 \cdot 10^{-7} \\ -1.08 \cdot 10^{-5} & 5.07 \cdot 10^{-4} & 9.20 \cdot 10^{-6} \\ 2.09 \cdot 10^{-5} & 6.17 \cdot 10^{-6} & 4.69 \cdot 10^{-4} \end{bmatrix} \quad (6.27)$$

First, these two calibration matrices are compared with the theoretical calibration matrix. The first and distinct difference between the two matrices and the theoretical matrix is that the diagonal values (sensitive regression slopes) in the two matrices have increased and that of the theoretical matrix have decreased compared to the single sensor sensitivity. The decrease of the diagonal values in the theoretical matrix comes from the fact that a small percentage of the load is distributed to the other two sensors (structural matrix, equation 6.22). However, for the other two matrices, it is not clear what phenomenon causes the diagonal values to increase.

The second difference is that the off-diagonal values of the full upright calibration matrix are exceeding the values of the theoretical matrix. That could mean two things: the structural behaviour of the sensor is not as expected or other unknown effects occur in the sensor when it is assembled. In case the structural behaviour is not as expected, a higher percentage could be directed to the sensors in the non-sensitive direction and increase these values. However, in this case, it would mean that the diagonal values should decrease due to this effect, but the opposite is observed.

The last difference observed in the matrices is the sign of the values. The off diagonal values of  $\beta_{2k}$  and  $\beta_{1k}$  have a negative sign in the full upright calibration matrix and a positive sign in the theoretical matrix. During the calibration of the single sensors, it was already observed that the regression slope of the three sensors for the positive K direction were deviating. This effect could cause the opposite sign in the matrices. For sensor 2, the sensitivity for the L direction has an opposite sign in the matrices. From the theory or physics there is yet no explanation for.

To better compare how well the full upright calibration matrix corresponds with the theoretical calibration matrix, the difference of each matrix value is determined relative to the theoretical value. With this comparison, a factor is obtained for each matrix value. The first row (intercepts) of the theoretical matrix is zero, as it is an exact solution. Therefore, the first row is not taken into account for this comparison. The result is shown in equation 6.28.

$$\textit{Matrix difference factor} = \begin{bmatrix} 0.030 & 164.3 & 52.9 \\ 681.7 & 0.014 & 1353 \\ 1064 & 276.7 & 0.016 \end{bmatrix} \quad (6.28)$$

The difference factor is a good indicator how well it matches the theoretical value. The closer the factor is to zero, the better it matches. The diagonal values match very well, as the values are much smaller than 1. The off diagonal values deviate more. As each column presents the sensitivity of a single sensor in all directions, it can be seen that sensor two (column 2) is closest to the theoretical values.

### **Comparison with random data set**

Another method to compare the calibration matrices, is by testing the matrices with a new data set. From the calibration experiments C1 a random set of 40 data points were omitted during the regression analysis. And with this data set the performance of the different calibration matrices can be tested. The weight distribution of this random data set together with the sensor range is shown in figure 6.25.

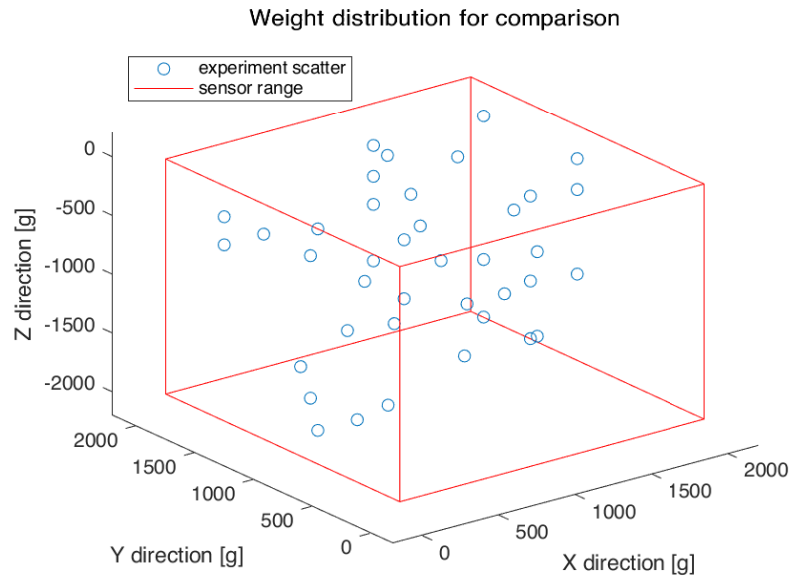


Figure 6.25: Weight distribution of random data set for comparison

The calibration matrices are tested with this random data set by calculating the applied weight with the measured output voltages and the calibration matrices. With equation 6.13, the applied weights are estimated. From these calculations, two weight approximations and the exact weight resulted. This is shown in figure 6.26.

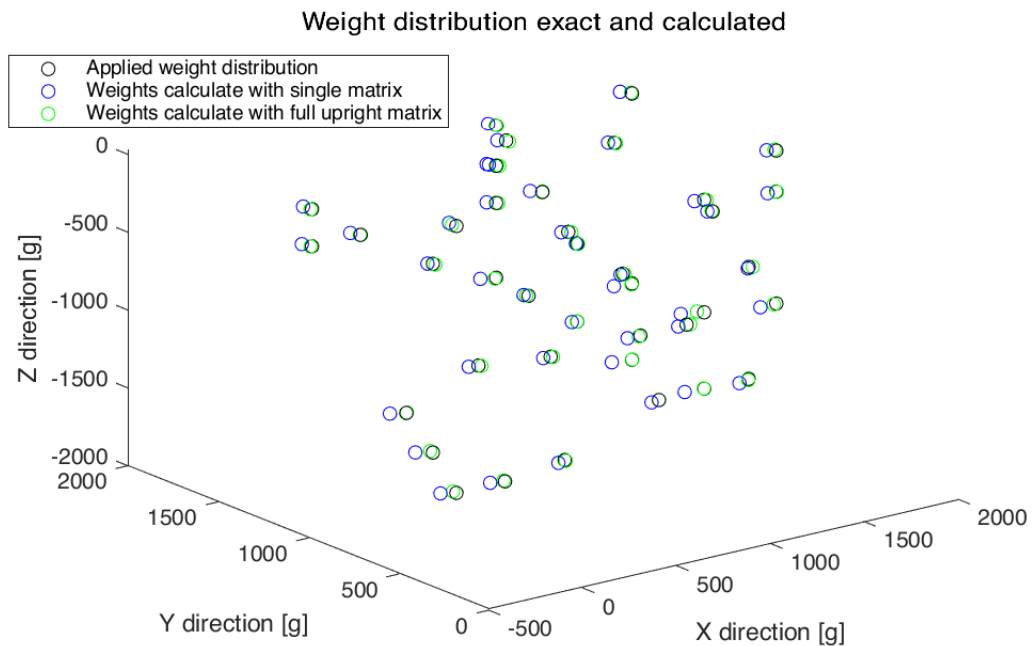


Figure 6.26: Weight approximation of calibration matrices and exact weight

From this figure, it is difficult to distinguish the errors of the calibration matrices. Therefore, to further investigate the error in the calculated weights, the deviation in percentage of each calculated weight per global direction is calculated, equation 6.29.

$$e_{n_i} = \frac{W_{n_i} - W_{e_i}}{W_{e_i}} \cdot 100\% \quad (6.29)$$

In this equation, the error  $e_{n_i}$  is calculated for each data set number  $n$  and global direction  $i$ , with the estimated weight  $W_{n_i}$  and the exact weight  $W_{e_i}$ . The results are shown in figure 6.27a, 6.27b and 6.27c.

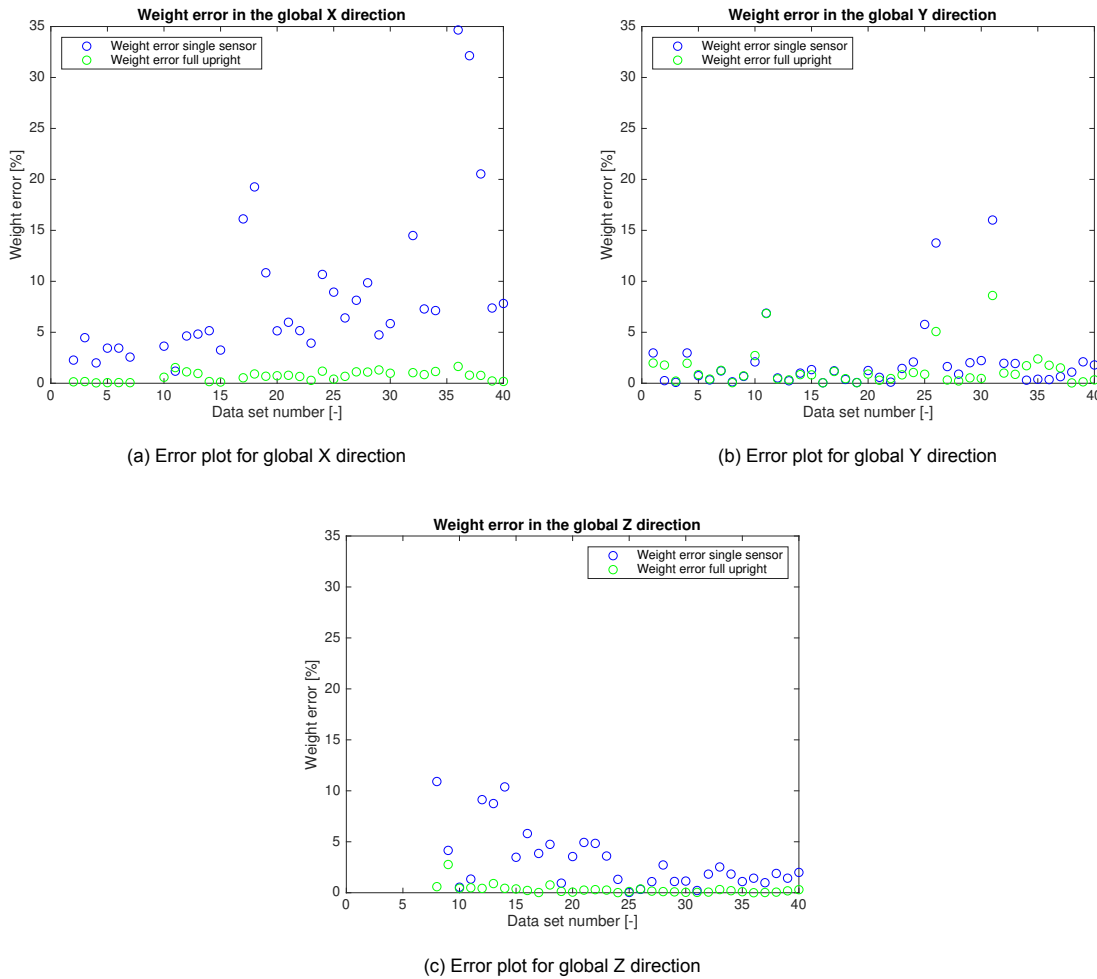


Figure 6.27: Weight error plots for all global directions

Calculating the error per global direction for the applied weight gives information for each direction. In case a small weight is applied in a certain direction, a small error will cause a higher percentage error than in case a large weight is applied. Therefore, errors are calculated as the total percentage error in 3D space. Equation 6.30 is used to determine these total percentage errors. In figure 6.28 the results are plotted.

$$e_{t_n} = \frac{\sqrt{(W_{e_x} - W_{n_x})^2 + (W_{e_y} - W_{n_y})^2 + (W_{e_z} - W_{n_z})^2}}{\sqrt{W_{e_x}^2 + W_{e_y}^2 + W_{e_z}^2}} \cdot 100\% \quad (6.30)$$

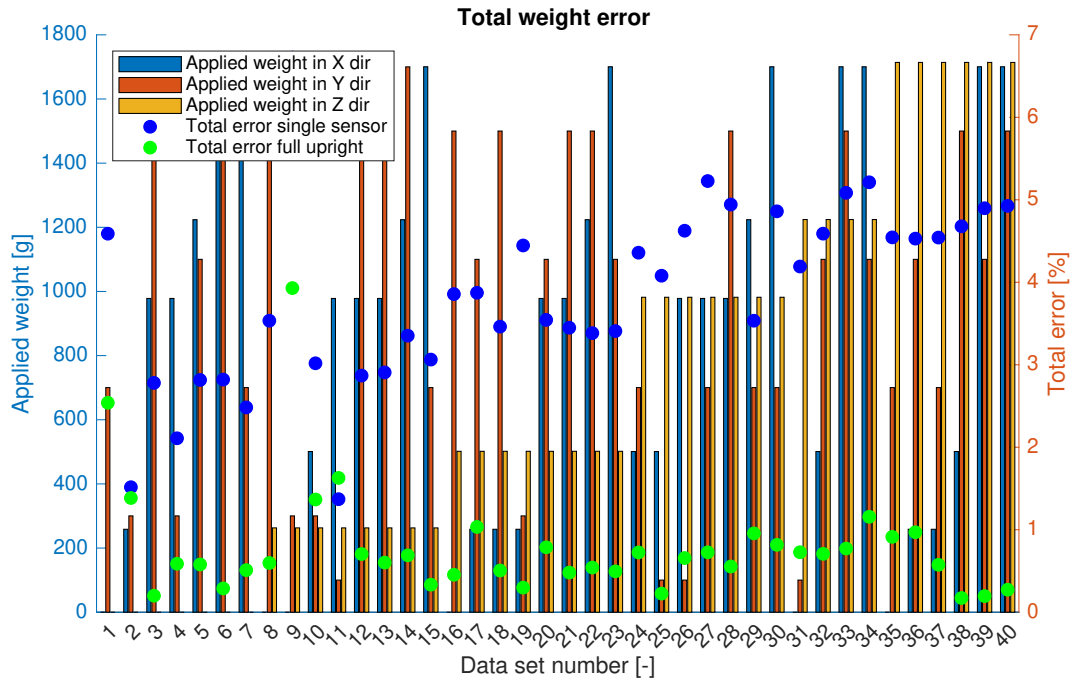


Figure 6.28: Total error plot for each calibration matrix, left axis: applied weight, right axis: total percentage error

From this figure, it can be observed that the total error of the full upright matrix is constant around 1 percent with a couple of outliers. These outliers come with small applied total loads. The total error for the single sensor matrix is significantly higher.

### 6.4. Frame calibration rotated position

In the third part of the calibration procedure, the complete sensor frame is again calibrated. Different from the previous described calibration is the orientation of the sensor. For this part, the sensor frame is positioned in the rotated position. Similar to the previous calibration, the sensor frame is calibrated by applying loads in all directions. With this calibration, different calibration matrices are again obtained and tested for a random data set. Before the sensor frame is calibrated, additional theory is required to determine the rotation matrix of the sensor frame and to determine what the calibration setup should be able to do.

#### 6.4.1. Theory rotation matrix

As mentioned in the design of the sensor setup, the sensor frame should be rotated in order to maximize the vertical distance of each sensor with the water surface. By rotating the sensor, the local axis system of the sensor (U,V,W) is not in line with the global axis system (X,Y,Z). This means that the calibration matrix determined in section 6.3 does no longer apply. For that calibration matrix, both the input and output variables should be in the X,Y,Z coordinate system, equation 6.31. For the rotated frame, the input variables are still in the X,Y,Z coordinate system, but the output variables are in the U,V,W coordinate system.

$$\underbrace{\begin{bmatrix} Y_{11} & Y_{12} & Y_{13} \end{bmatrix}}_{X,Y,Z\text{axis}} = \underbrace{\begin{bmatrix} 1 & X_{11} & X_{12} & X_{13} \end{bmatrix}}_{X,Y,Z\text{axis}} \times \underbrace{\begin{bmatrix} \beta_{01} & \beta_{02} & \beta_{03} \\ \beta_{11} & \beta_{12} & \beta_{13} \\ \beta_{21} & \beta_{22} & \beta_{23} \\ \beta_{31} & \beta_{32} & \beta_{33} \end{bmatrix}}_{X,Y,Z\text{axis}} \tag{6.31}$$

The rotated frame should be calibrated in order to translate the measured output into usable data. This calibration is possible by two methods. The first method is to determine the rotation matrix for the sensor in the rotated position and multiply this with the calibration matrix in the upright position. The

second method is to perform a full calibration experiment described in section 6.2.4 at the experimental setup location in the rotated position.

Preferably, the calibration experiments are performed at the workshop and not at the experimental setup. To determine the rotation matrix of the first method, only two weights should be applied at the experimental setup, whereas for the second method a complete calibration procedure should be performed.

For a rotated sensor, the output signals  $Y$  are in the local rotated  $U,V,W$  coordinate system. To receive output signals in the  $U,V,W$  coordinate system, the calibration matrix is multiplied with the rotation matrix for the first method:

$$\underbrace{\begin{bmatrix} Y_{11} & Y_{12} & Y_{13} \end{bmatrix}}_{U,V,W \text{ axis}} = \underbrace{\begin{bmatrix} 1 & X_{11} & X_{12} & X_{13} \end{bmatrix}}_{X,Y,Z \text{ axis}} \times \underbrace{\begin{bmatrix} \beta_{01} & \beta_{02} & \beta_{03} \\ \beta_{11} & \beta_{12} & \beta_{13} \\ \beta_{21} & \beta_{22} & \beta_{23} \\ \beta_{31} & \beta_{32} & \beta_{33} \end{bmatrix}}_{X,Y,Z \text{ axis}} \times \mathbf{M}_r^{-1} \quad (6.32)$$

The rotation matrix should be obtained in the experimental setup. This can be done by applying a weight in two global axis directions. The output values of these two experiments are in the  $U,V,W$  coordinate system. These values are then normalized and with these experiments two direction of the axis system are determined. The third perpendicular axis can be computed with the cross product:

$$\mathbf{v}_1 = \mathbf{v}_2 \times \mathbf{v}_3 = \begin{bmatrix} y_1 \\ y_2 \\ y_3 \end{bmatrix} \times \begin{bmatrix} z_1 \\ z_2 \\ z_3 \end{bmatrix} = \begin{bmatrix} y_2 z_3 - y_3 z_2 \\ y_3 z_1 - y_1 z_3 \\ y_1 z_2 - y_2 z_1 \end{bmatrix} = \begin{bmatrix} x_1 \\ x_2 \\ x_3 \end{bmatrix}$$

(6.33)

Where  $v_2$  and  $v_3$  are two normalized measured axis directions,  $Y$  and  $Z$  respectively, and  $v_1$  is the third perpendicular axis  $X$ . These normalized axis directions in the  $X,Y,Z$  coordinate system are defined by the components in the  $U,V,W$  coordinate system. And by combining the three normalized axis direction, the rotation matrix is obtained.

$$\mathbf{M}_r = \begin{bmatrix} x_1 & y_1 & z_1 \\ x_2 & y_2 & z_2 \\ x_3 & y_3 & z_3 \end{bmatrix} \quad (6.34)$$

#### 6.4.2. Calibration setup rotated frame

In the previous section, two methods are described to determine the calibration matrix for the rotated sensor. Normally, these calibration experiments should be performed in the experimental setup. However, the goal of this project is to investigate the performance of the sensor frame. Therefore, the calibration experiments for the rotated sensor are performed in the workshop to ensure controlled conditions.

For both methods, the calibration setup described in section 6.2.3 is adapted. The sensor frame described in that section is positioned in the upright position. In order to position the sensor frame in the rotated position, a second frame is added to the calibration setup, see figure 6.29. This second frame consists of ITEM 40x40 profiles and a camera ball head. With the camera ball head, the sensor frame can be rotated in approximately the correct position. To ensure the loads are still applied in the orthogonal directions on the rotated sensor frame, the connection block should be positioned at the same position. Therefore, a pointer plate is placed onto the calibration frame and aligned with the connection block. After this, the sensor frame can be removed and placed in the second frame for the rotated position. This frame is then positioned in a way that the pointer plate and connection block are aligned again. After this is done, the pointer plate can be removed and the connection block is aligned with the pulleys.

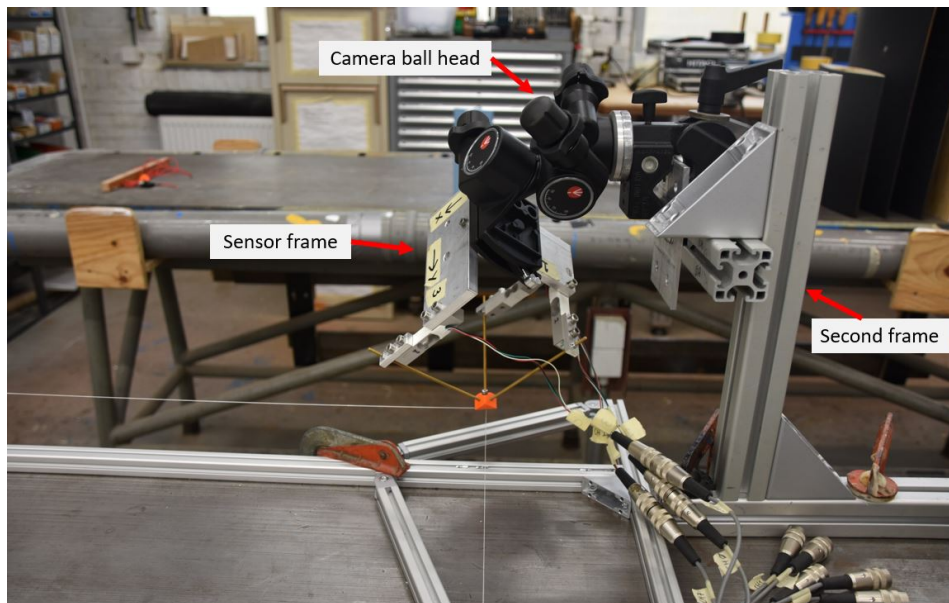


Figure 6.29: Second sensor frame to position the sensor frame in rotated position

### 6.4.3. Calibration experiments

The calibration experiments required for the sensor frame in the rotated position are similar to the experiments for the sensor frame in the upright position, experiment group C1. In table 6.9, the experiment group is shown including a reference number. More detailed information of each experiment can be found in table G.1.

Table 6.9: Calibration experiments for sensor frame in rotated position with reference number

Calibration reference number	Type of calibration experiment	Force sensor	Experiment numbers
C2	Complete sensor frame rotated position	1,2,3	157-177, 180-193

For the calibration C2, similar weights are applied as used for calibration C1. However, the scheme for calibration C2 differs from calibration C1. Due to the rotated sensor frame, the sensor range in the X,Y,Z coordinate system is changed as well. In figure 6.17, the outer range of the sensor was shown. This presents only the range of the sensor when they are all loaded in tension. However, the sensor can also cope with compression forces. The range of the sensor in the upright position for both tension and compression loads is presented in figure 6.30. This range also takes into account the shape of the connection block. For the rotated sensor frame, it is inevitable that compression forces are applied on the sensor. Therefore, the sensor range for the rotated frame can be visualized as figure 6.31, where the red area corresponds to the sensor range for both compression and tension. This resulting range can be described as a diamond like shape. From this plot, it can be seen that a certain part of the calibration scheme falls out of the sensor range, these calibration points are omitted for the calibration experiments C2.

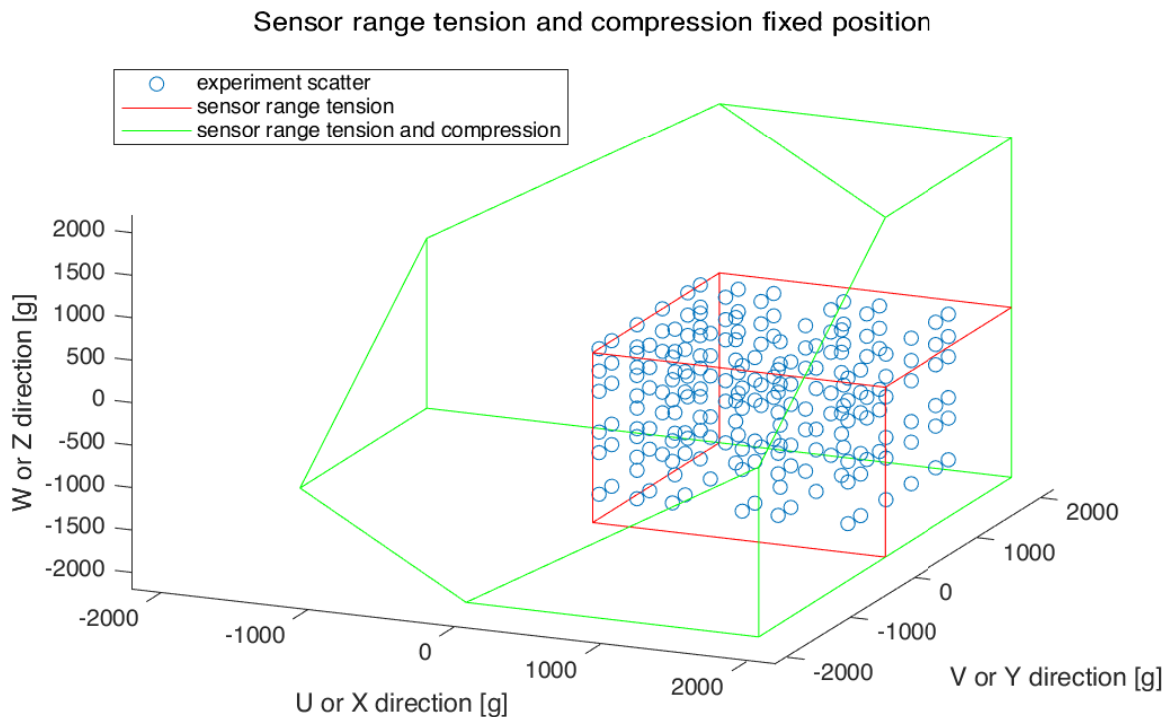


Figure 6.30: Sensor range for tension and compression in upright position

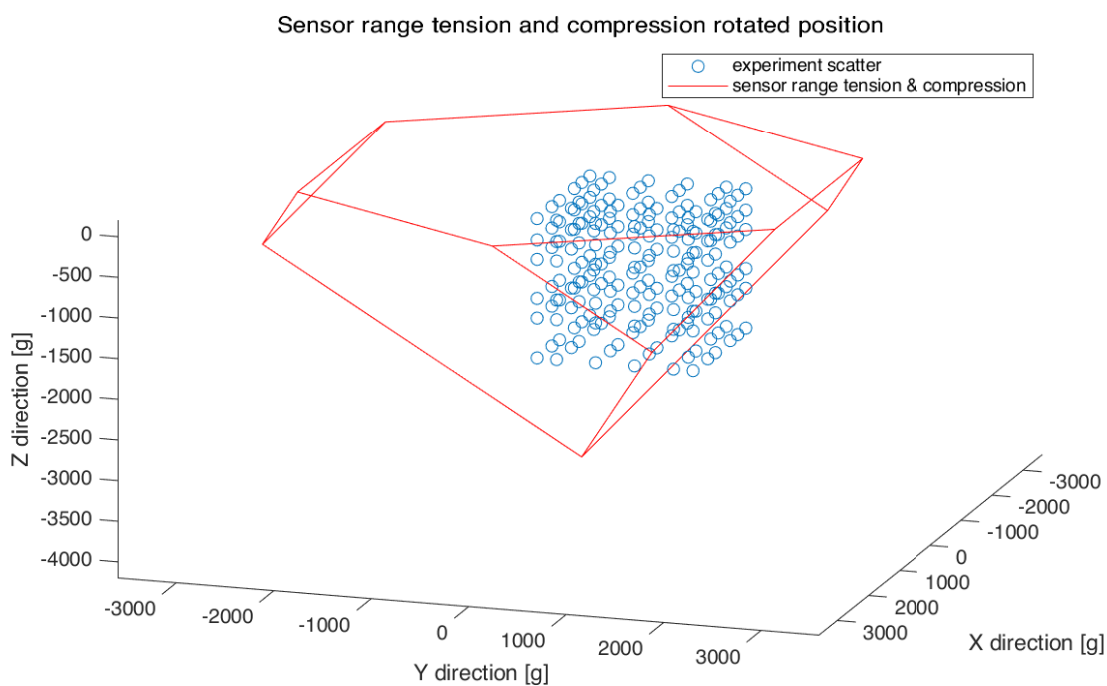


Figure 6.31: Sensor range for tension and compression in rotated position, diamond like shape

### 6.4.4. Results

The results of the calibration experiments are divided into two parts. First, the rotation matrix is determined with the use of specific calibration data of C2, and after that the calibration matrix for the rotated

frame is determined with all calibration data of C2.

In section 6.4.1, it is explained how the rotation matrix can be obtained. From the calibration experiments, experiments 157, 168, 174, 180, 183 and 189 are used for the rotation matrix. In experiment 157, 168, 174, 180 and 183 a weight only in the global Y direction is applied and in 189 a weight in the Z direction for a total of 11 different weights. With these measurements the rotation matrix can be determined. First, the normalized Y and Z axis are determined in equation 6.35 and 6.36, in this equation the mean value of the different measurement results is calculated. Next, the third normalized axis X is obtained with equation 6.4.1. With these three normalized axes the rotation matrix is formulated as equation 6.37.

$$v_2 = \text{mean} \left( \text{norm} \begin{pmatrix} -0.14 \text{ mV/V} \\ 0.33 \text{ mV/V} \\ 0.12 \text{ mV/V} \end{pmatrix} + \text{norm} (...) + \dots \right) = \begin{matrix} -0.36 \\ 0.88 \\ 0.32 \end{matrix} \quad (6.35)$$

$$v_3 = \text{mean} \left( \text{norm} \begin{pmatrix} -0.55 \text{ mV/V} \\ -0.46 \text{ mV/V} \\ 0.46 \text{ mV/V} \end{pmatrix} + \text{norm} (...) + \dots \right) = \begin{matrix} -0.64 \\ -0.54 \\ 0.54 \end{matrix} \quad (6.36)$$

$$M_r = \begin{bmatrix} 0.65 & -0.36 & -0.65 \\ -0.012 & 0.87 & -0.54 \\ 0.76 & 0.32 & 0.54 \end{bmatrix} \quad (6.37)$$

For the second part, all calibration experiments of C2 are used for determining the calibration matrix of the rotated sensor frame. In figure 6.32, the output data of experiment 188 is shown. In this figure, it can be seen that the sensor frame is rotated by the output voltage of all three sensors. At around 40 seconds, the weights in the global Y direction are stacked. From the output voltages, it can be seen that all three sensors are largely influenced by these weights, which means that there is not a single sensor exactly in line with the global Y direction.

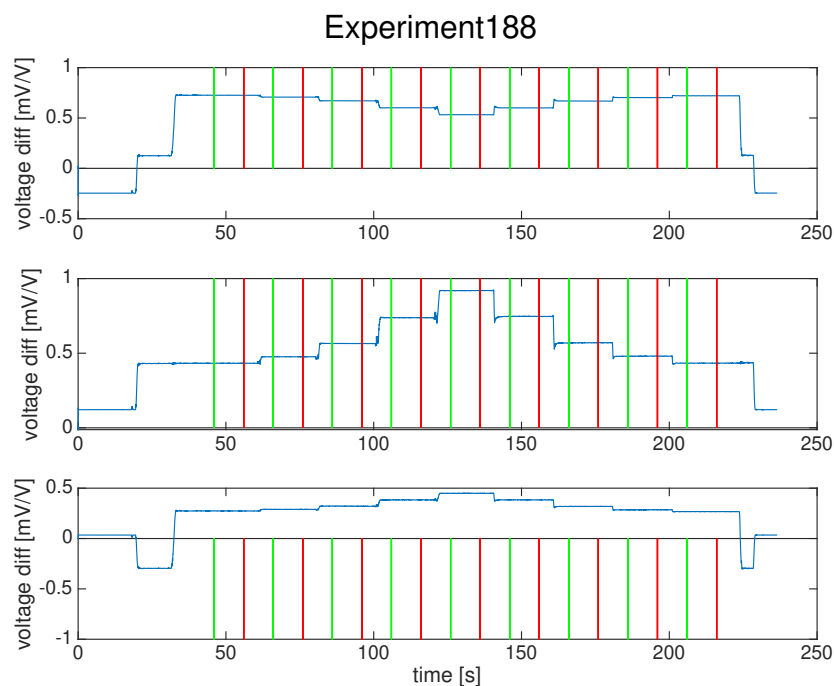


Figure 6.32: Output data experiment 188

In total, 371 data points are obtained from the calibration experiments, and with these data points the regression analysis is performed. From this analysis the calibration matrix in equation 6.38 is determined.

$$\text{Calibration matrix} = \begin{bmatrix} -4.7 \cdot 10^{-4} \text{ mV/V} & 0.0030 \text{ mV/V} & 0.0036 \text{ mV/V} \\ 3.58 \cdot 10^{-4} \text{ mV/(V * g)} & -1.27 \cdot 10^{-7} \text{ mV/(V * g)} & 3.34 \cdot 10^{-4} \text{ mV/(V * g)} \\ -1.75 \cdot 10^{-4} \text{ mV/(V * g)} & 4.51 \cdot 10^{-4} \text{ mV/(V * g)} & 1.67 \cdot 10^{-4} \text{ mV/(V * g)} \\ -3.01 \cdot 10^{-4} \text{ mV/(V * g)} & -2.51 \cdot 10^{-4} \text{ mV/(V * g)} & 2.72 \cdot 10^{-4} \text{ mV/(V * g)} \end{bmatrix} \quad (6.38)$$

Similar to the results of the regression analysis for the upright position, residuals are determined to investigate the performance of the regression analysis. In figure 6.33 and 6.34, the residuals for the output voltage and weight are plotted respectively.

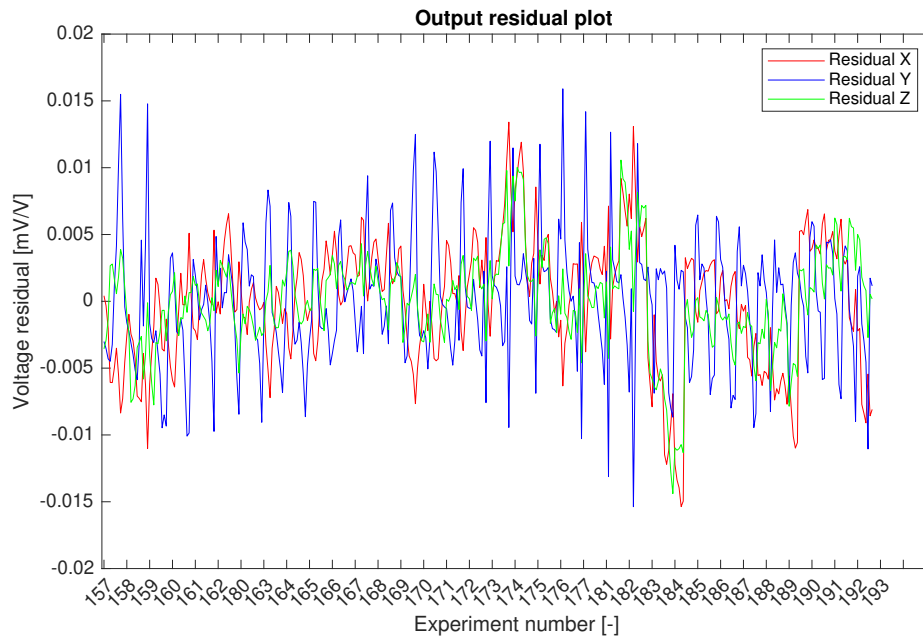


Figure 6.33: Residual plot of measured voltage of rotated sensor frame

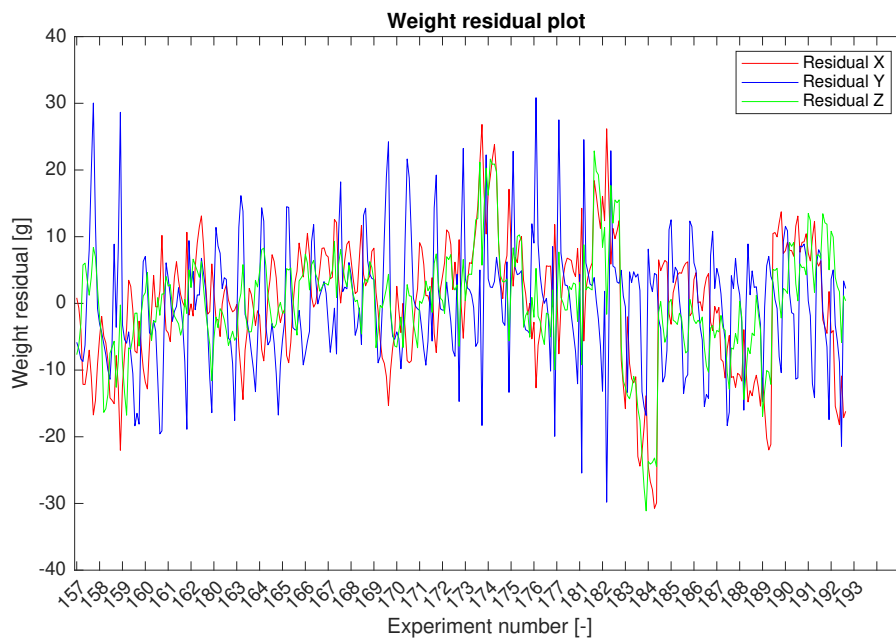


Figure 6.34: Residual plot of applied weight on rotated sensor frame

From the residual plots, it can be seen that all three sensors contain residuals in the same order. For the residuals of sensor 2, residual Y in figure 6.33, a periodicity is observed. This periodicity was also observed in the residuals for the upright position calibration matrix. Similar to that observation, the periodicity can be related to the stacking of weights in the global Y direction. In figure 6.35, the periodicity is shown in a zoomed in figure.

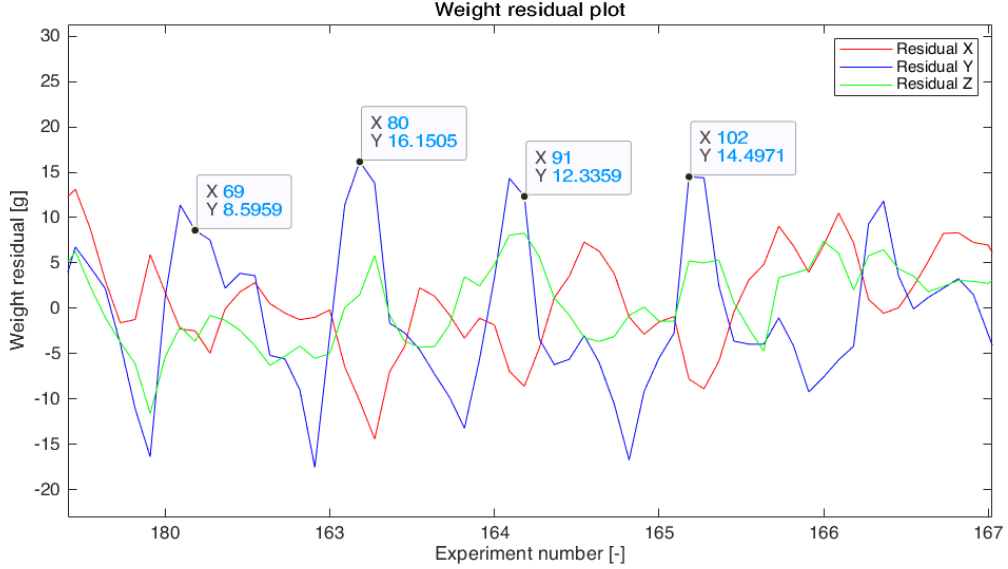


Figure 6.35: Residual plot of applied weight on rotated sensor frame, zoomed in periodicity Y

## 6.5. Comparison calibration matrices rotated position

With the calibration experiments for the rotated sensor frame, the rotation matrix is determined as well as the calibration matrix for the rotated position. Now that these properties are known, the calibration matrix for the rotated sensor frame can be determined in different ways. First of all, the calibration matrix is directly determined in section 6.4.4. Secondly, the two calibration matrices for the upright position determined in section 6.3.4 can be used together with the rotation matrix to obtain the calibration matrix for the sensor in the rotated position. In the next sections, first the rotation matrix is verified by a theoretical rotation matrix after which the three different calibration matrices are compared with the use of a random set of data points.

### 6.5.1. Rotation matrix verification

In the calibration setup, the sensor frame is rotated with the use of a camera ball head. With this ball head, it was possible to set angles with an accuracy of approximately 2 degrees. Before these angles were set, the sensor frame was levelled with a plastic circular level.

To verify that the sensor frame was positioned as intended, the rotation matrix of equation 6.37 is checked with a theoretical rotation matrix. The rotation of an object in a 3D space can be divided into rotation matrices for all global axis. The sensor is first rotated around the Y axis with  $\alpha = 45$  degrees, after which it was rotated around the X axis with  $\beta = -35$  degrees. The theoretical rotation matrices for a rotation around the Y and X axis are shown in equation 6.39 and 6.40 respectively.

$$M_{r\_Y} = \begin{bmatrix} \cos(\alpha) & 0 & -\sin(\alpha) \\ 0 & 1 & 0 \\ \sin(\alpha) & 0 & \cos(\alpha) \end{bmatrix} \quad (6.39)$$

$$M_{r\_X} = \begin{bmatrix} 1 & 0 & 0 \\ 0 & \cos(\beta) & \sin(\beta) \\ 0 & -\sin(\beta) & \cos(\beta) \end{bmatrix} \quad (6.40)$$

The rotation matrix is then found by multiplying the two rotation matrices and filling in the rotation angles. This results in the theoretical rotation matrix of equation 6.41.

$$M_{r\_theo} = M_{r\_Y} \times M_{r\_X} = \begin{bmatrix} 0.707 & -0.406 & -0.579 \\ 0.000 & 0.819 & -0.574 \\ 0.707 & 0.406 & 0.579 \end{bmatrix} \quad (6.41)$$

By comparing the theoretical rotation matrix with the rotation matrix of equation 6.37, we can conclude that calculation of the rotation matrix is working as expected. The values of the matrices are similarly sized and the signs of the values in the matrices match. As the rotation of the sensor was performed by hand and on sight, small deviations between the matrices were expected. The deviations between the theoretical rotation matrix and the obtained rotation matrix do correspond with angle deviations of 4 degrees. This accuracy is slightly lower than what was expected from the rotation tools.

### 6.5.2. Calibration matrices comparison rotated position

Before the calibration matrices for the rotated sensor frame can be compared, the matrices are determined. The first calibration matrix is constructed with the single sensor calibration matrix (equation 6.26) and the rotation matrix (equation 6.37), the second matrix of the full upright calibration matrix for the upright position (equation 6.27) and the rotation matrix (equation 6.37). The third calibration matrix is determined in equation 6.38. Below the three calibration matrices for the rotated position are shown for the single sensor, full upright and full rotated matrix in equation 6.42, 6.43 and 6.44 respectively.

$$\text{Single sensor rotated calibration matrix} = \begin{bmatrix} -2.48 \cdot 10^{-5} & -5.34 \cdot 10^{-5} & 2.88 \cdot 10^{-5} \\ 3.31 \cdot 10^{-4} & -6.06 \cdot 10^{-6} & 3.85 \cdot 10^{-4} \\ -2.05 \cdot 10^{-4} & 4.29 \cdot 10^{-4} & 1.83 \cdot 10^{-4} \\ -3.16 \cdot 10^{-4} & -2.26 \cdot 10^{-4} & 2.68 \cdot 10^{-4} \end{bmatrix} \quad (6.42)$$

$$\text{Full upright rotated calibration matrix} = \begin{bmatrix} 0.0014 & 0.0038 & 0.0028 \\ 3.26 \cdot 10^{-4} & -7.36 \cdot 10^{-6} & 3.76 \cdot 10^{-4} \\ -2.18 \cdot 10^{-4} & 4.24 \cdot 10^{-4} & 1.79 \cdot 10^{-4} \\ -3.04 \cdot 10^{-4} & -2.20 \cdot 10^{-4} & 2.85 \cdot 10^{-4} \end{bmatrix} \quad (6.43)$$

$$\text{Full rotated calibration matrix} = \begin{bmatrix} -4.7 \cdot 10^{-4} & 0.0030 & 0.0036 \\ 3.58 \cdot 10^{-4} & -1.27 \cdot 10^{-7} & 3.34 \cdot 10^{-4} \\ -1.75 \cdot 10^{-4} & 4.51 \cdot 10^{-4} & 1.67 \cdot 10^{-4} \\ -3.01 \cdot 10^{-4} & -2.51 \cdot 10^{-4} & 2.72 \cdot 10^{-4} \end{bmatrix} \quad (6.44)$$

A method to compare the calibration matrices, is by testing the matrices with a new data set. From the calibration experiments C2, a random set of data points were omitted during the regression analysis. With this data set the performance of the different calibration matrices can be compared. The weight distribution of this random data set together with the sensors rotated range (diamond like range) is shown in figure 6.36.

Weight distribution of random data set for comparison rotated position

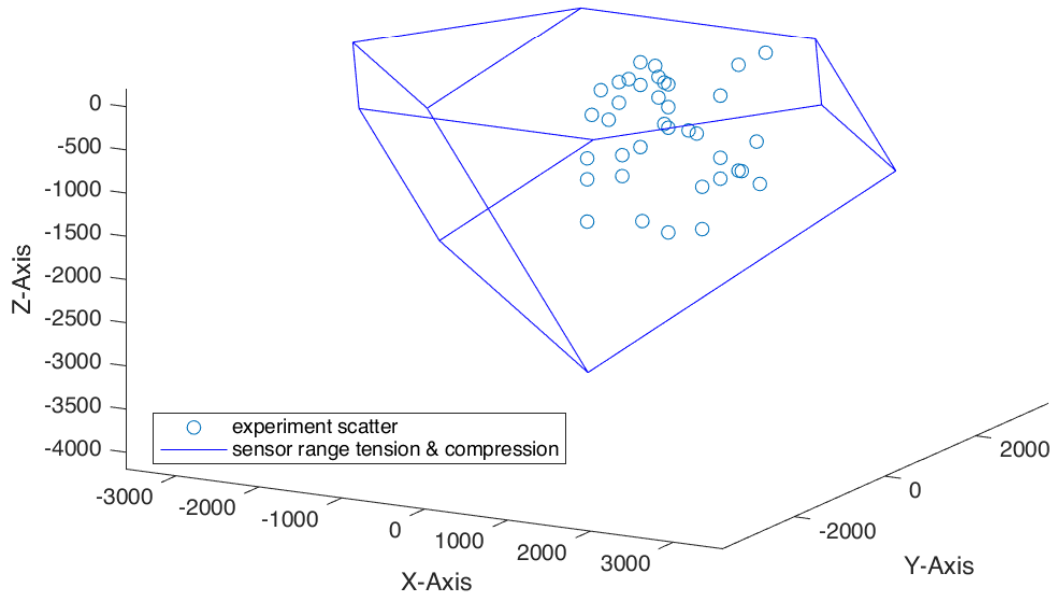


Figure 6.36: Weight distribution of random data set for comparison

The calibration matrices are compared by calculating the weights with the output voltage and the three different calibration matrices. From the data set, the applied weight is known and these values can be compared with the calculated values. In figure 6.37, the exact weights and calculated weights are plotted.

Weight distribution exact and calculated

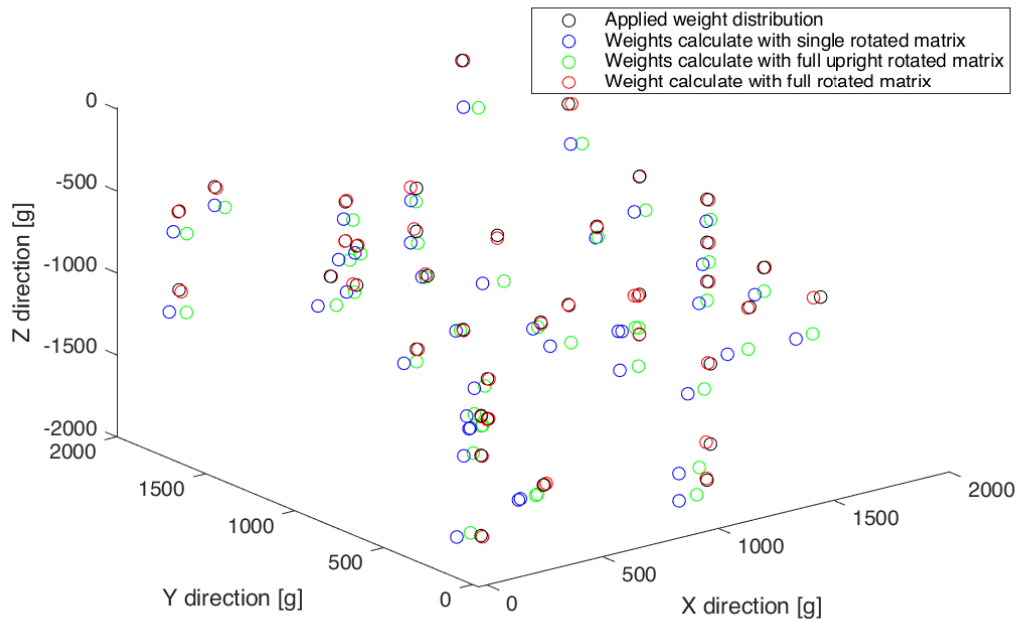


Figure 6.37: Weight distribution of known values and calculated

From this plot, it can be observed that the weights calculated by using the full rotated calibration matrix are closest to the exact weights. To further investigate the error in the calculated weights, the deviation in percentage of each calculated weight per global direction is calculated, equation 6.45.

$$e_{n_i} = \frac{W_{n_i} - W_{e_i}}{W_{e_i}} \cdot 100\% \quad (6.45)$$

Where  $W_{n_i}$  is the weight,  $i$  is the global direction (X, Y or Z),  $n$  is the calibration matrix type (single sensor, full upright or full rotate),  $W_{e_i}$  is the exact weight and  $e_{n_i}$  is the error of the calculated weights compared to the exact weight in percentage.

The errors for each global direction X, Y and Z are presented in figure 6.38a, 6.38b and 6.38c.

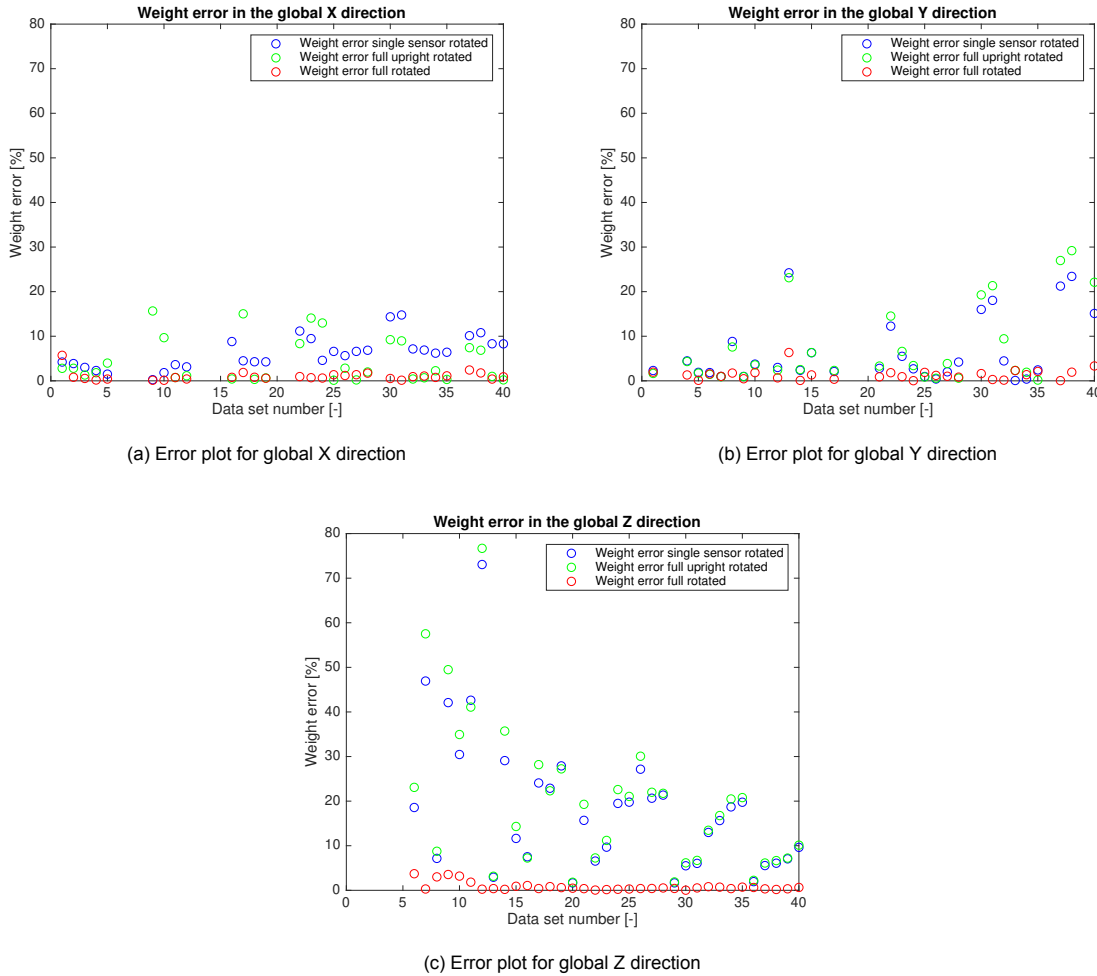


Figure 6.38: Weight error plot for all global directions

From these figures, it can be observed that the errors of the full rotated calibration matrix are the lowest. For the other two calibration matrices, the errors are fluctuating excessively. For the Z direction, the maximum error is around 80%.

Calculating the error per global direction gives information for each direction. In case a small weight is applied in a certain direction, a small error will cause a higher percent error than in case a large weight is applied. Therefore, errors are calculated as the total percent error in 3D space. Equation 6.46 is used to determine these total percent errors. In figure 6.39 the results are plotted.

$$e_{t_n} = \frac{\sqrt{(W_{e_x} - W_{n_x})^2 + (W_{e_y} - W_{n_y})^2 + (W_{e_z} - W_{n_z})^2}}{\sqrt{W_{e_x}^2 + W_{e_y}^2 + W_{e_z}^2}} \cdot 100\% \quad (6.46)$$

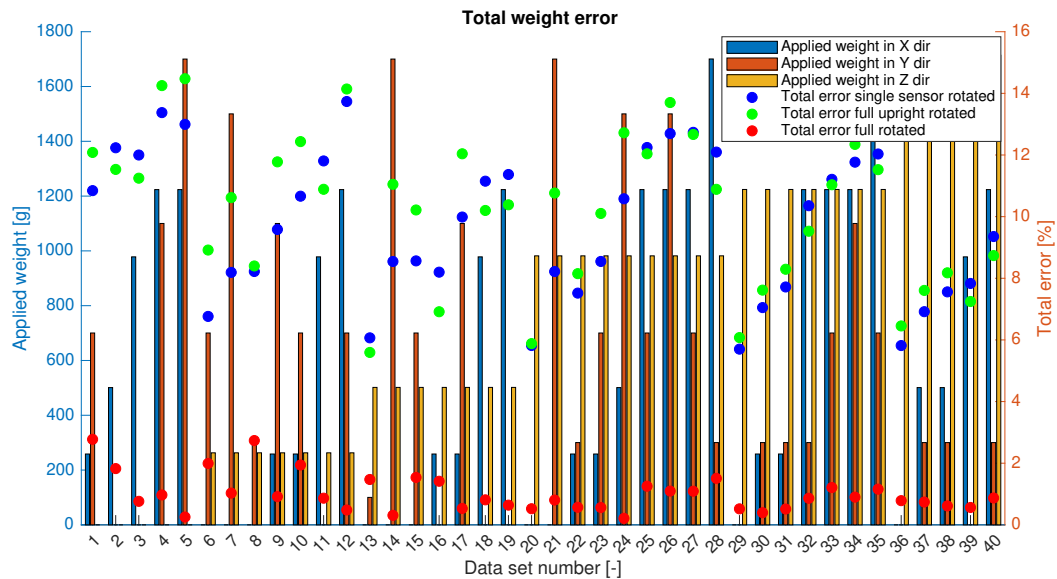


Figure 6.39: Total error plot for each calibration matrix, left axis: applied weight, right axis: total percentage error

In figure 6.39, the applied weight in each global direction is plotted with a histogram. Moreover, the total error in percentage is plotted for each data point. Compared to the error plots for the individual global directions, the percent errors have lower outliers. The maximum errors in this plot are around 15%. For the full rotated calibration matrix, the errors are around 2% and the other two calibration matrices range from 6% up to 15%. For the percent error of the single sensor rotated matrix and full upright rotated matrix a pattern can be observed. The total percent error increases for increasing weights in the global X direction, this is repeated 6 times.

## 6.6. Discussion calibration matrix

The results of the calibration experiments show that the matrices can measure the loads on the sensor frame. However, the accuracy of each matrix differs greatly depending on the calibration method. Especially for the sensor frame in the rotated position, large differences are observed between the matrices. For this setup, two remarks are made.

First of all, the sensor frame is positioned with a camera ball head. During the experiments, small deflection were observed of the connection block, due to the flexibility of the camera ball head. With a deflection of the connection block, the loads are not applied in orthogonal directions and the results will be influenced. The largest deflections of the connection block were observed when a large load was applied in the global Y direction. The maximum deflections were up to 10mm, which causes undesired force components up to 1% of the applied force.

Secondly, the pulley system to apply loads in the global X and Y direction suffers from friction. This friction is also observed in figure 6.22. To identify how friction influences the results, an additional experiment is performed with a single force sensor and a pulley. The error observed in this experiment is used to validate that the residuals in the full upright calibration matrix are mainly caused by this effect.

### 6.6.1. Pulley friction

During the experiments with the sensor frame, periodic fluctuations were observed in the results. To identify what causes this periodicity, an experiment is performed, focused on the pulley system.

In this experiment, the sensor frame is placed in the upright position in the calibration setup, figure 6.15. A single force sensor is positioned at sensor position 3 of the sensor frame. With this setup, a calibration experiment is performed where weights are applied in the sensitive direction of the sensor. The weights are applied directly to the sensor without the use of a pulley.

After this experiment, the sensor is relocated to sensor position 2 in the sensor frame. With this setup another calibration experiment is performed by applying the same weights as in the previous experiment. For this experiment the weight are also applied in the sensitive direction of the sensor. To

achieve this, the pulley system is used to transfer the load from a vertical load into a horizontal load. A detailed image of the pulley system is shown in figure 6.40.

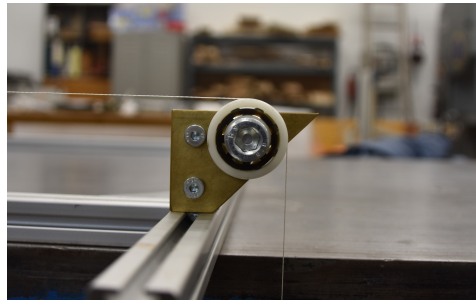


Figure 6.40: Detailed image of pulley system

With the experiments described above, the regression analysis is performed twice, first for the sensor at sensor position 3 and second for the sensor at sensor position 2. The results of these experiments for the direct weight and weight over the pulley are shown in figure 6.41 and 6.42 respectively for sensor 1. In appendix E, the results of all three sensors are shown.

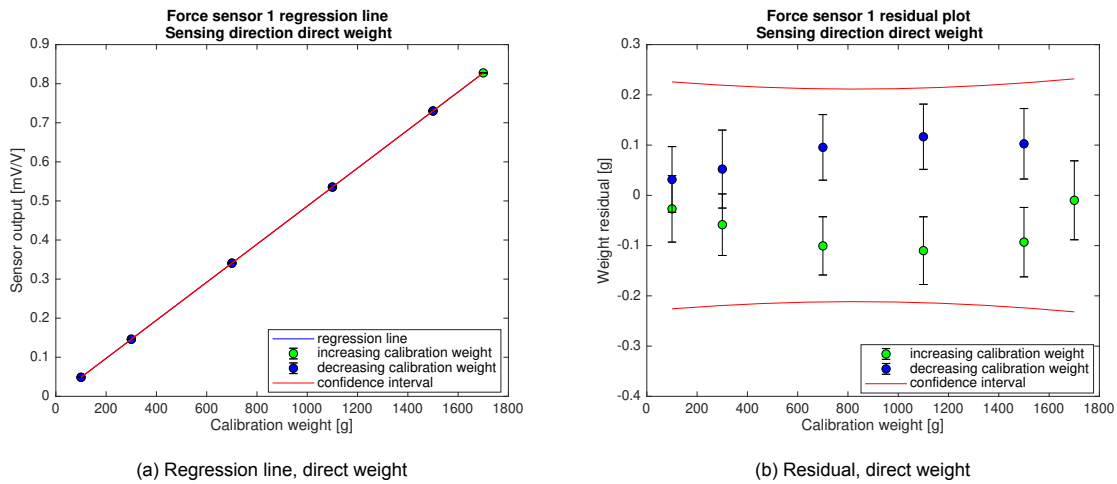


Figure 6.41: Regression line and residual plot of direct weight for sensor 1

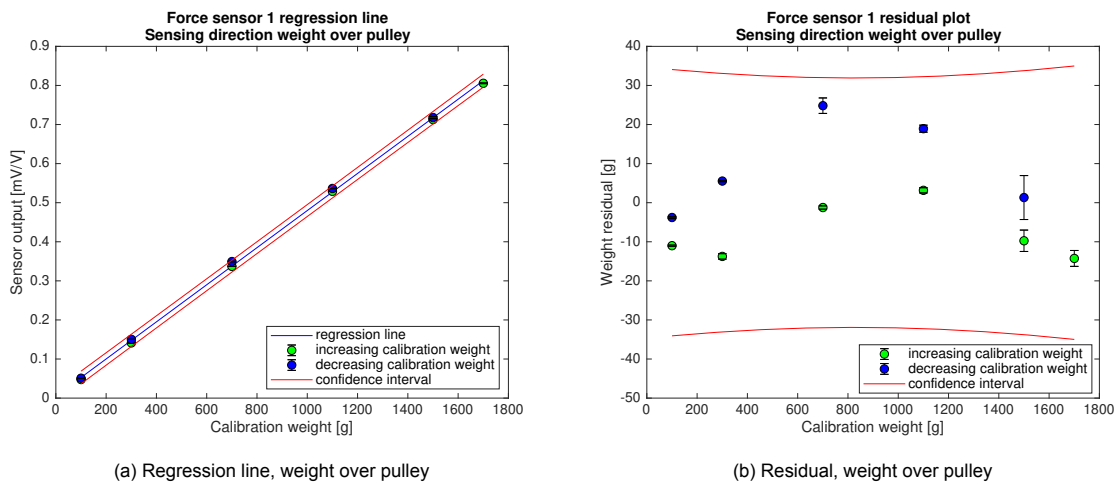


Figure 6.42: Regression line and residual plot of weight over pulley for sensor 1

From figure 6.41 and 6.42, the effect of the pulley system is clearly visible. For the experiment where the pulley system is not used, figure 6.41, the residuals are small with a maximum of around 0.15g. The hysteresis observed during the single sensor experiments (section 6.1) are observed in this experiment as well. For the experiment in which the pulley system is used, figure 6.42, the influence of the pulley system is clearly visible. The residuals of this experiment are much bigger (around 30g) and likewise the hysteresis is much bigger. The residuals of decreasing weights deviate strongly, especially the eighth and ninth step (blue data points).

This deviation most likely is caused by friction in the pulley. When the pulley is loaded by the weights a part of the force is diverted to the pulley's axis. When the pulley is unloaded (weights are removed), pretension in the pulley's axis induces an extra load on the sensor. This phenomenon is seen in figure 6.22. For the weights applied in the global Y direction, the residuals have a peak at the eighth data point of each experiment. This corresponds with the residual plot shown in figure 6.42.

To verify that this pulley effect is also causing the large residuals in the full sensor calibration experiments, figure 6.21 is used. In this figure the residuals for the full upright calibration matrix are shown. From this figure it was observed that the residuals in the X and Y direction contain residuals up to 30g, and for the Z direction only residuals up to 8g. The weights in the X and Y direction are applied with the pulley system, whereas no pulley system is used for the Z direction. Therefore, a random output voltage error is added to the results in the Z direction. This random error should be equal to the output voltage error caused by the pulley system. The magnitude of the output voltage error by the pulley system is shown in figure 6.43.

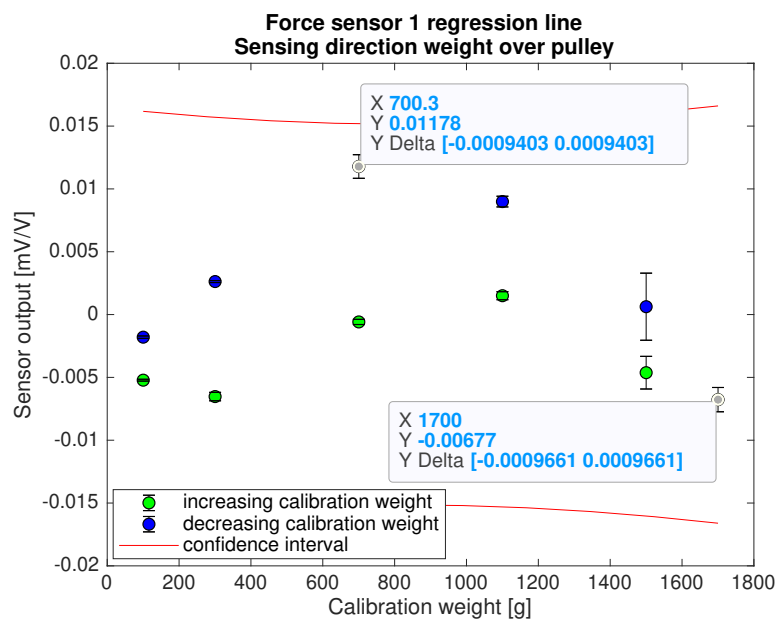


Figure 6.43: Residual plot of measured output voltage of weight over pulley for sensor 1

From this figure it is determined that the minimum and maximum output voltage difference is -0.007 mV/V and 0.012 mV/V respectively. The measured output data in the Z direction obtained for the full upright calibration matrix is then added with a random number in this range. By adding a random number, the residual in the Z direction will increase. In figure 6.44, the residual plot is again presented, however, in this figure the random added numbers are included.

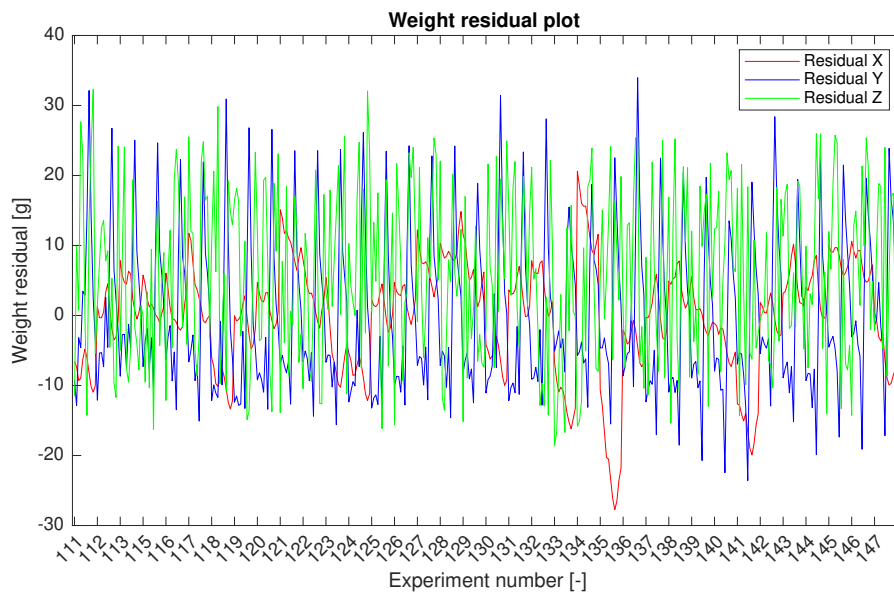


Figure 6.44: Residual plot of measured output voltage for upright sensor frame, with random addition to Z direction

In the figure above it can be observed that the residual magnitude for the Z direction is similar to the X and Y direction. This confirms that the difference between the residuals in the X and Y direction and the Z direction are caused by the pulley system.

## 6.7. Conclusions calibration matrix

In this chapter, the calibration experiments including the results are presented. From the result of the calibration experiments, several conclusion can be drawn:

The force sensor meets the specification provided by the supplier. With the single sensor calibration experiments, the sensitivity of the sensors is determined and corresponds with the specifications.

The calibration matrices determined with calibration experiments differ from the theoretical matrix, thus unexpected phenomena happen in the sensor frame. Therefore, the calibration matrix is best determined with the complete sensor frame assembled to include all effects.

To determine the calibration matrix for the sensor frame in the upright position, the full upright calibration matrix is the best method. With this method, the error of the measured load is almost entirely below 2 percent.

The most accurate method to determine the calibration matrix for the rotated sensor frame, is the full rotated matrix. With this matrix, the error of the measured load is almost entirely below 2 percent. To determine this calibration matrix, the complete calibration procedure should be performed at the experimental setup. The full upright rotated matrix potentially is a good method to determine the calibration matrix for the rotated position. However, due to the pulley effects in the calibration setup and the flexible camera ball head, this method does not yet meet the requirements. In case these effects are reduced, this method has potential, and the calibration experiments can be performed in a controlled environment, whereafter only a simple experiment is required in the experimental setup.

In case the calibration setup is improved with low friction pulleys and a stiff connection, the full upright rotated calibration matrix is the best method to determine the calibration matrix. With this method, the calibration matrix can be determined only once and can be used for different experimental setups. In the experimental setup, only the rotation matrix needs to be determined.

# 7

## Example application

In chapter 6, different calibration methods are analyzed. From this analysis, it was concluded that the full upright calibration procedure is the best way to determine the calibration matrix. To investigate the performance of the complete setup under real conditions, an example application is carried out. The goal of this example application is to investigate the usability of the sensor frame in real conditions. The focus is not on the accuracy of the measurement results.

### 7.1. Experimental procedure

Before the example application is carried out, the steps required for performing experiments are listed. This experimental procedure scheme should be used to set up a experimental test.

- **Sensor frame requirements**  
First the sensor frame requirements should be determined. The amount of mooring forces that should be measured determine the amount of sensor frames that are required. And with a first approximation of the mooring forces, the force sensors can be selected.
- **Sensor frame calibration (Section 6.3.4)**  
The sensor frame should be calibrated according the calibration procedure described in section 6.3.4. In case multiple sensor frames are used, each sensor frame should be calibrated.
- **Installation sensor frame**  
After the sensor frame is calibrated, it can be installed in the experimental setup in the towing tank. The sensor frame should be positioned in the right place and stay at that position during all towing tank experiments. The sensor frame should be aligned with the additional frame to perform the orientation experiments. After the sensor frame is installed it can be connected to the data acquisition system.
- **Orientation experiments**  
With the orientation experiments, the rotation matrix is obtained. The required experiments and calculations are described in section 6.4.
- **Zero measurement**  
Before the mooring line of the floating structure is connected to the sensor frame, a zero measurement is performed. This measurement determines the output values in case no force is applied on the sensor frame.
- **Connecting floating structure**  
Mooring lines of the floating structure are connected to the sensor frame. Only a single mooring line can be attached to a sensor frame. Multiple sensor frames should be used if several mooring lines are measured. After the floating structure is installed, pretension can be applied on the structure and mooring lines by positioning the mooring line connections.

- Pretension measurement  
To determine the pretension in the mooring lines, a second measurement is performed. With the zero measurement and the second measurement, the pretension is calculated. In case the pretension is not sufficient, the mooring line connections can be repositioned. The second measurement should be repeated to determine the pretension.
- Towing tank experiments  
With the sensor frame and floating structure in position, the experiments in the towing tank can be performed.
- Process data  
The data obtained during the towing tank experiments are processed to obtain the mooring forces. With the calibration matrix and rotation matrix, the mooring forces in the global orientation are calculated.

## 7.2. Experimental setup

The experiments are carried out in the towing tank No. 1 at the TU Delft. This towing tank is 142 m long, 4.22 m wide and has a depth of around 2.5 m. As the goal is to determine the usability of the sensor frame, the water temperature, surrounding temperature and water depth are not measured. For the experiments the wave maker is used that consists of a flap type wave maker with a hinge point at the bottom of the tank. During the experiments with the sensor frame and the floating structure, waves are created by the wave maker. As the focus is on the usability of the sensor only two types of waves are tested. The parameters of these waves are listed in table 7.1.

Table 7.1: Wave conditions

Wave condition	Period T [s]	Wave length $\lambda$ [m]	Rel. model length L/ $\lambda$ [-]	Wave amplitude A [mm]
W1	0.877	1.2	4.13	20
W2	0.796	0.99	5.00	20

The sensor frame is designed to measure the mooring forces on flexible floating structures at model scale. Hence, the sensor frame is attached to a neoprene foam rubber sheet, similar to the sheet used in the article of Schreier and Jacobi [26]. The sheet is 4.95 m long, 1.02 m wide and has a thickness of 5 mm. According the article of Schreier and Jacobi [26], the sheet has a density of 116 kg/m<sup>3</sup>, a plate bending stiffness of 6.9·10<sup>-4</sup> Nm, Young's modulus of 560 kPa and a characteristic length of  $\lambda_c = 0.17$  m.

Similar to the calibration setups, the sensor frame is connected to a data acquisition PC, PXIe-1078 National Instruments chassis with a National Instruments strain/bridge input module PXIe-4330. With this setup, a sampling rate of 1000 Hz and a 24 bit resolution are achieved and an anti-alias filter is build in the system.

The floating structure is moored with 4 mooring lines to the sides of the tank, two at the front and two aft. The sensor frame is attached to the front left mooring line. The front mooring lines are attached to a beam that is placed across the tank. The two aft mooring lines are attached to the side of the towing tank. In figure 7.1, the setup is shown including the mooring lines.

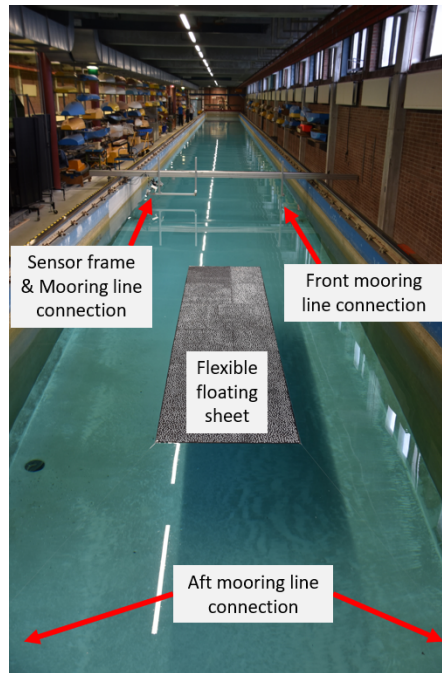


Figure 7.1: Experimental setup with flexible floating structure

The front mooring lines consist of Dyneema lines, these lines have a very high stiffness. The aft mooring lines consist of elastic sewing thread. As these lines have a low stiffness, internal tension of the structure is minimized during the experiments.

To be able to measure the real wave conditions exerted on the floating structure, the water surface elevation is measured with an acoustic wave probe, the General Acoustics USS 13-HF sensor. With a similar reference wave probe, the speed of sound is measured to calibrate the acoustic wave probe. The wave probe is connected to a separate amplifier, the General Acoustics UltraLab ULS Advanced amplifier. This amplifier is connected to the data acquisition PC. The control of the wave probe is done in a different program than the control of the sensor frame and should be started separately.

In figure 7.2, a top view of the experimental setup is shown with the location of the mooring lines, sensor frame and the floating structure. In table 7.2, the distances of the setup are indicated.

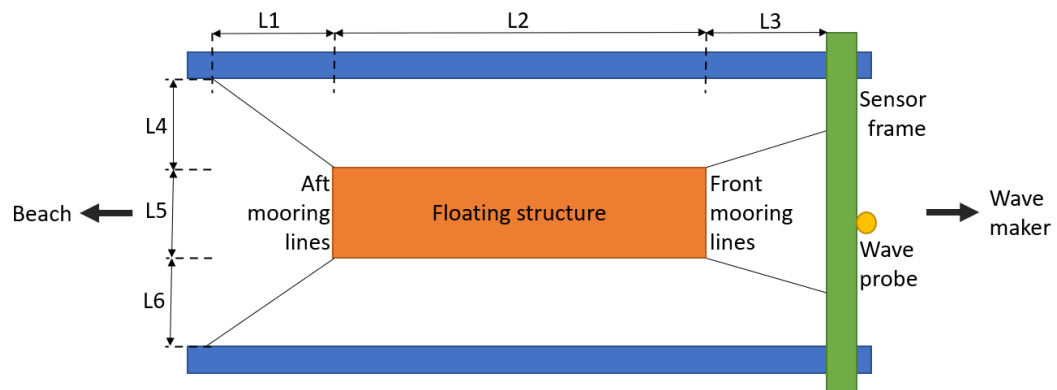


Figure 7.2: Experimental setup in towing tank No. 1 at TU delft

Table 7.2: Variable lengths of experiments setup

Variable	L1	L2	L3	L4	L5	L6
[m]	4.63	4.98	5.70	1.72	1.02	1.49

The sensor frame is installed on a large beam across the towing tank. In addition to this large beam an extra frame is required. With this extra frame, the camera ball head can be attached as close to the water surface as possible and the required experiments for the orientation can be performed with this frame. The frame consists of ITEM 40x40 beams, a connection for the camera ball head and two pulleys. In figure 7.3, the additional frame is shown. The function of the pulleys is described in the next section.

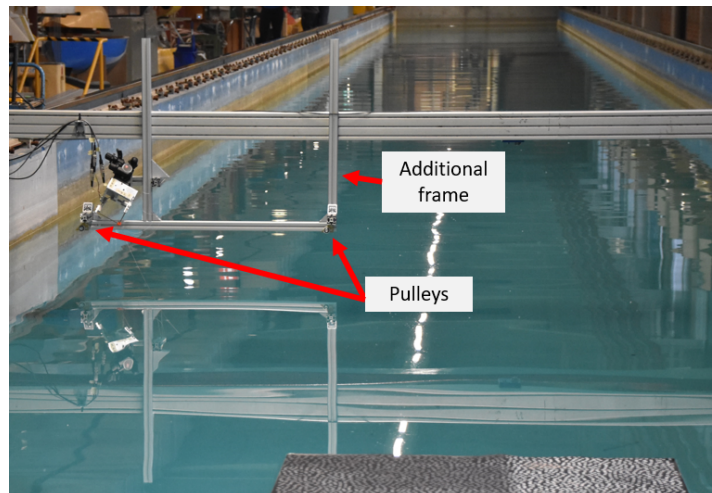


Figure 7.3: Additional frame for positioning the sensor frame

## 7.3. Experiments

To be able to measure the mooring forces on a floating structure with wave loading, different experiments are required. In table 7.3 the required experiments are listed.

Table 7.3: Experiments for the example application in the towing tank

Reference number	Type of experiment	Force sensor	Experiment numbers
TT1	Sensor frame function test	1,2,3	195
TT2	Rotation matrix	1,2,3	196-199
TT3	Zero measurement pretension	1,2,3	200-201
TT4	Wave loading experiment	1,2,3	202-206

First, the sensor is installed in the towing tank with the additional frame including the camera ball head. When the sensor frame is installed and completely connected to the data acquisition instruments, a first experiment (TT1) is performed to ensure that the electrical system is installed correctly. After this experiment, the sensor frame is positioned in the rotated position with the camera ball head. The pulley on the additional frame should be aligned with the connection block of the sensor frame. To align the connection block, a line is stretched across two pulleys on the additional frame. After that, the connection block can be moved until it touches this line, see figure 7.4.

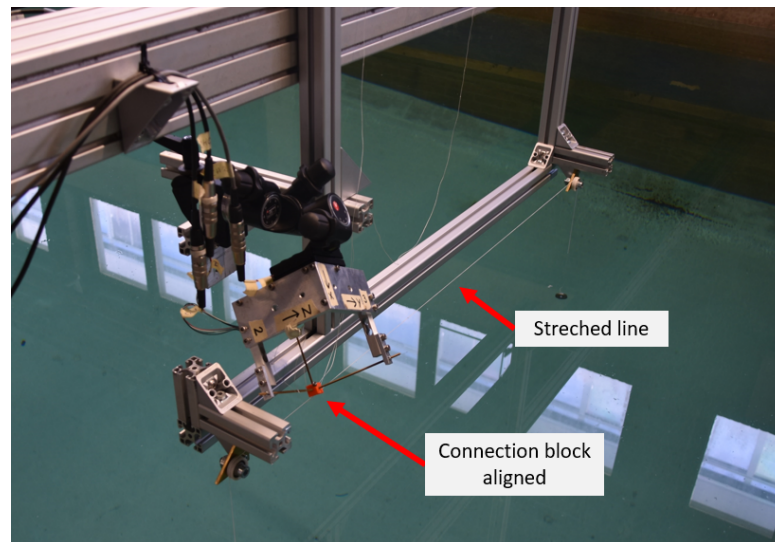


Figure 7.4: Sensor frame aligned with pulleys

With the sensor frame in position, the experiments for the rotation matrix are performed, experiment number TT2. To determine the rotation matrix, a weight should be applied in two global axis directions. These two directions are the global Y and Z direction. In figure 7.5, the experiment for the rotation matrix is shown. In this setup the weight is applied in the global Y direction. The rotation matrix is obtained according to the theory described in section 6.4.1.

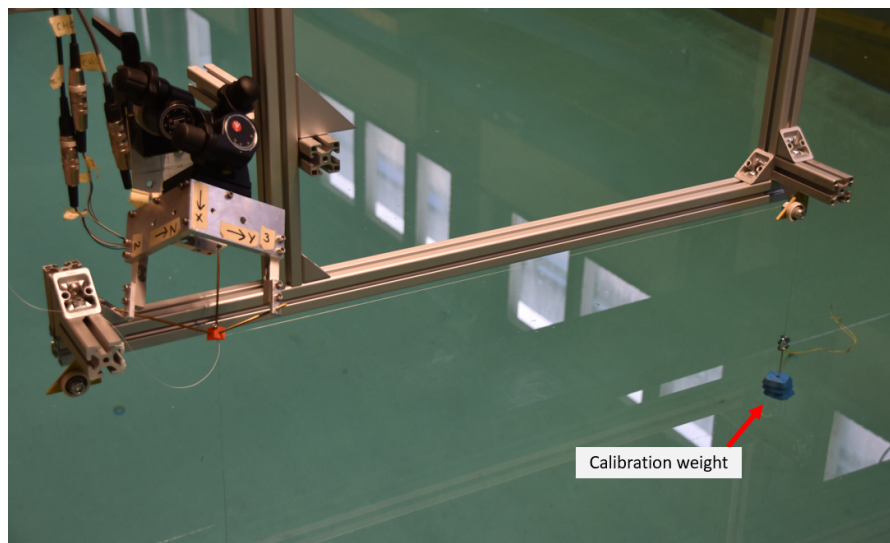


Figure 7.5: Experimental setup for the rotation matrix, weight applied in the global Y direction

The next experiment is performed to determine the pretension in the mooring line due to the floating structure, experiment number TT3. First, a zero measurement is performed without the floating structure, after which the floating structure is put in position. With the floating structure in position a second measurement is performed, whereafter the pretension is determined by the difference between these two measurements.

Finally, the wave loading experiments are performed, experiment number TT4. During these experiments, the sensor frame measures the forces in the mooring line and the wave probe measures the wave elevation.

## 7.4. Results

The results of the towing tank experiments are divided into three parts: rotation matrix, pretension and mooring force. The results of each part are described in the next sections. To obtain the results, several calculations are performed. An overview of the calculations is shown in appendix F.2.

### 7.4.1. Rotation matrix

With experiments of TT2, the rotation matrix can be calculated. With two experiments, the global axes in the Y and Z direction are determined and the third axis is calculated. From this calculation, the rotation matrix in equation 7.1 is obtained.

$$M_r = \begin{bmatrix} 0.599 & -0.338 & -0.706 \\ -0.048 & 0.889 & -0.501 \\ 0.797 & 0.308 & 0.500 \end{bmatrix} \quad (7.1)$$

### 7.4.2. Pretension

The floating structure is positioned in the towing tank with four mooring lines. Pretension is unavoidable in this setup, hence it is important to know the magnitude of the pretension. In the setup used for this project, only the pretension of the front left mooring can be determined. To determine this pretension, the difference of the output variables for the setup with and without the floating structure is measured, TT3. First, the output values of the sensor frame without the structure are set to zero and these corrections are also subtracted from the output values of the sensor frame with the structure. These output results are shown in figure 7.6.

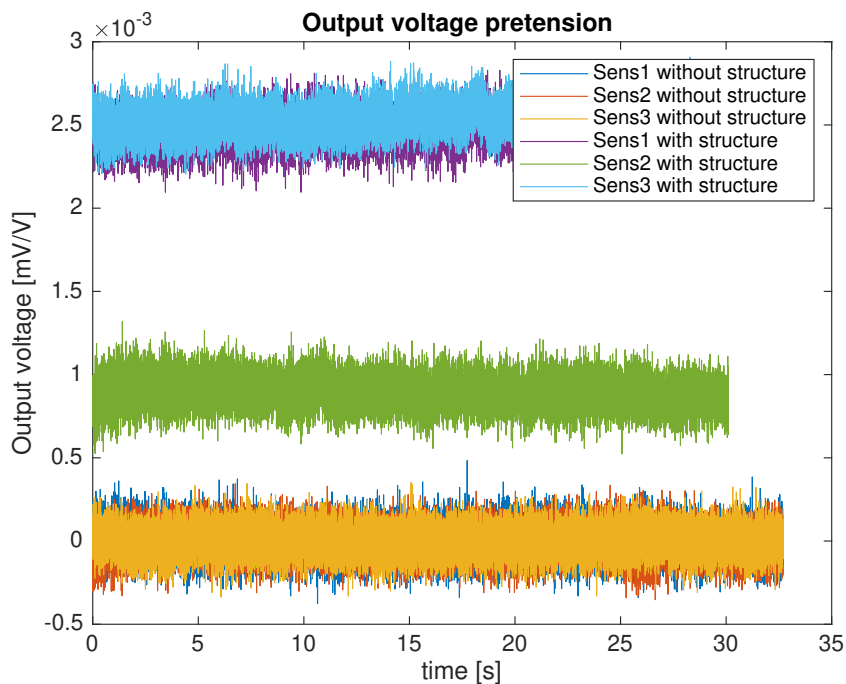


Figure 7.6: Zero measurement output values of the sensor frame with and without the structure

The pretension in the mooring line is now calculated with the calibration matrix of the full upright sensor in equation 6.27, the rotation matrix of equation 7.1 and the mean value of the output voltages of figure 7.6. From this calculation, the first result is the applied weight in each global direction:  $X_w = 7.08$  g,  $Y_w = 1.50$  g and  $Z_w = -2.00$  g. With these values and a gravitational constant of  $9.81$  m/s<sup>2</sup>, the total pretension in the mooring line is estimated as  $0.0737$  N.

### 7.4.3. Mooring force

With the experiments of TT4, mooring forces of the front left mooring line are measured with the floating structure in wave loading conditions. As the rotation matrix and the pretension of the setup are determined, output values can be translated to mooring forces. The wave with the parameters described in section 7.2 are generated by the wave maker and measured with the wave probe. The time series of the wave probe is shown in figure 7.7.

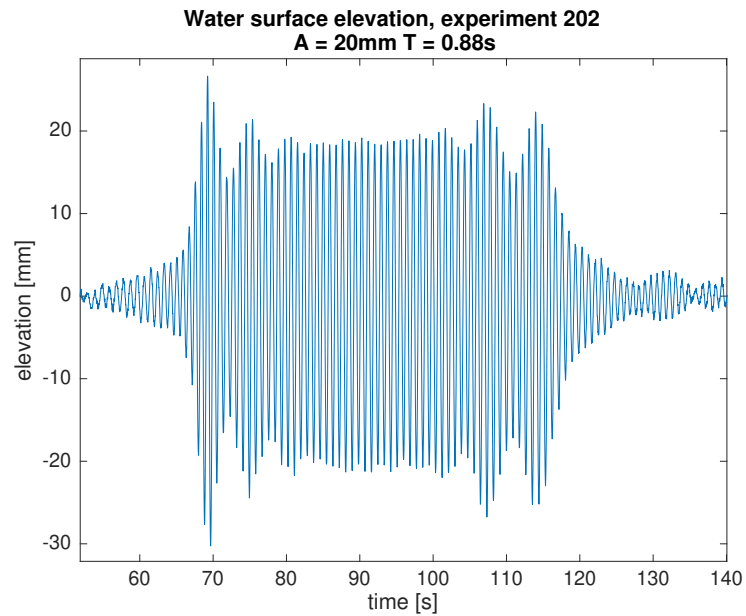


Figure 7.7: Water surface elevation at the front of the floating structure

In figure 7.8, the output values of experiment 202 are shown.

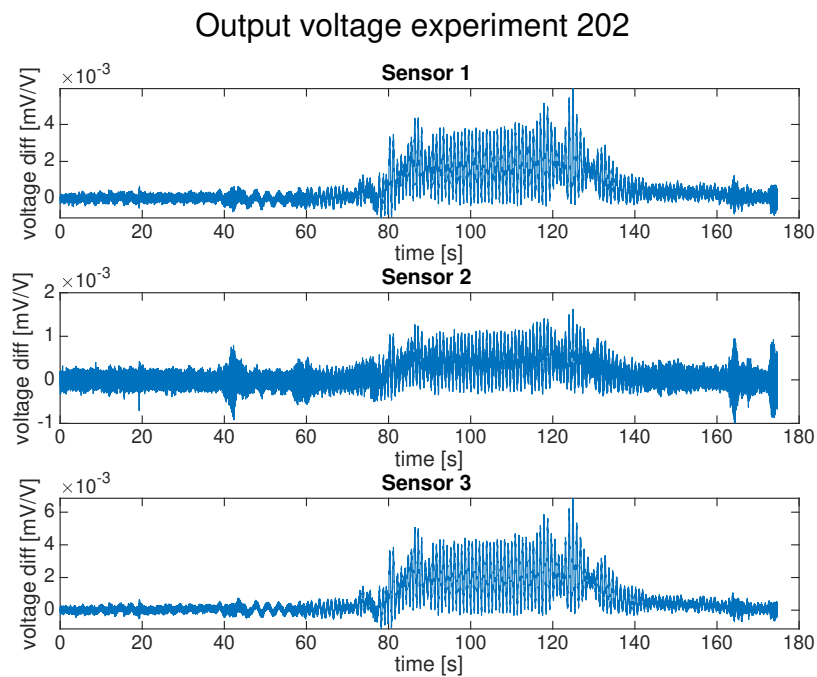


Figure 7.8: Output values of sensor frame

The time scale of the wave elevation in figure 7.7 and the measured output values in figure 7.8 are approximately started at the same time. However, for these experiments we are not interested in the phase of the wave and forces and therefore the different measurements are not exactly started at the same time. The waves arrive at the wave probe at around 70 seconds and this is visible in the output data of the sensor, which starts to fluctuate at around 80 seconds. When we zoom in on the output data of a single sensor, the wave period can be seen. A zoomed in figure of the output data of sensor 1 is shown in figure 7.9.

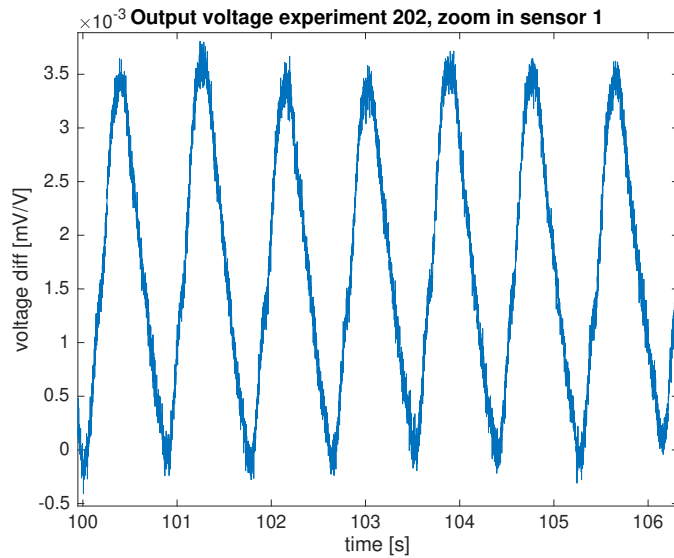


Figure 7.9: Output values of sensor 1 zoomed in

To determine the mooring force on the floating structure, the output data is translated with the rotation matrix, full upright calibration matrix and the gravitational constant of  $9.81 \text{ m/s}^2$ . In figure 7.10, the mooring force in each global direction is shown.

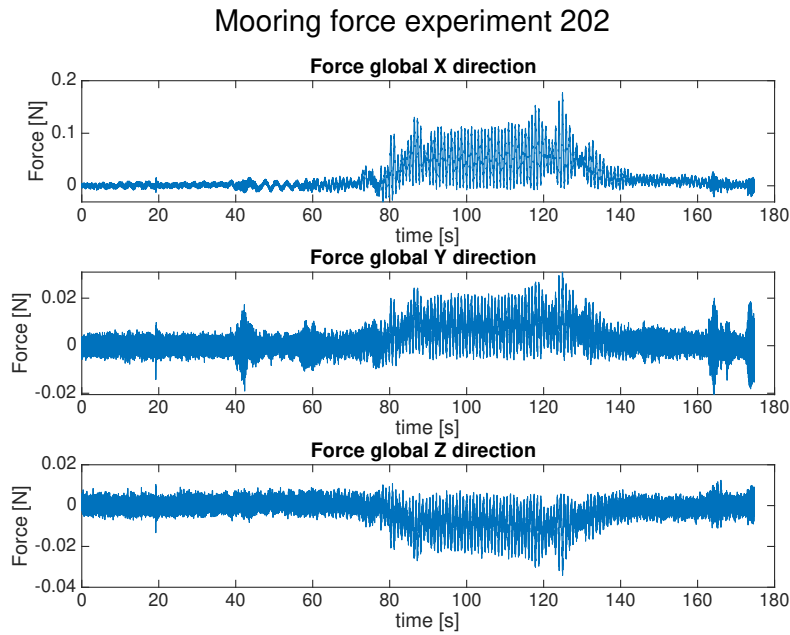


Figure 7.10: Mooring force in each direction, experiment 202

From the mooring forces in each global direction, the orientation of the mooring line can be determined. For a first estimation of the mooring line direction, an average is taken from the mooring force in each direction after a certain amount of waves, after which a normalized orientation is determined. The forces are averaged from 90 seconds to 110 seconds and shown in table 7.4. To compare the orientation of the total force with the actual mooring line orientation, the forces are normalized by dividing the averaged forces with the force in the X direction. These normalized forces are shown in table 7.4. In the last two columns of this table, the measured mooring line distance and the normalized orientation is shown. The distance in the X direction is measured in the experimental setup. The distance in the Y direction was not completely measured, only the distance of the floating structure to the towing tank wall was measured. The distance of the sensor frame to the towing tank wall is estimated to be 700mm. The height of the sensor frame was approximately 120mm above the water surface.

Table 7.4: Normalized mooring line orientation

Global direction	Averaged force [N]	Normalized force [-]	Mooring line distance [mm]	Normalized orientation [-]
X	0.052	1	5700	1
Y	0.0080	0.15	1120	0.20
Z	-0.0086	-0.17	120	-0.021

The normalized force and normalized orientation are not exactly the same. First of all, the signs of the two normalized values correspond, however the normalized force for the Z direction is ten times bigger than the normalized orientation. To explain this difference, we take a closer look into the mooring line configuration in figure 7.11. For the mooring line distance it is assumed that the mooring line reaches the water surface at the attachment point of the floating structure. However, in this figure it can be seen that the mooring line touches the water surface much earlier. This means that the mooring line distance is incorrect, and on top of that the mooring line orientation changes in case the floating structure is exerted with waves.

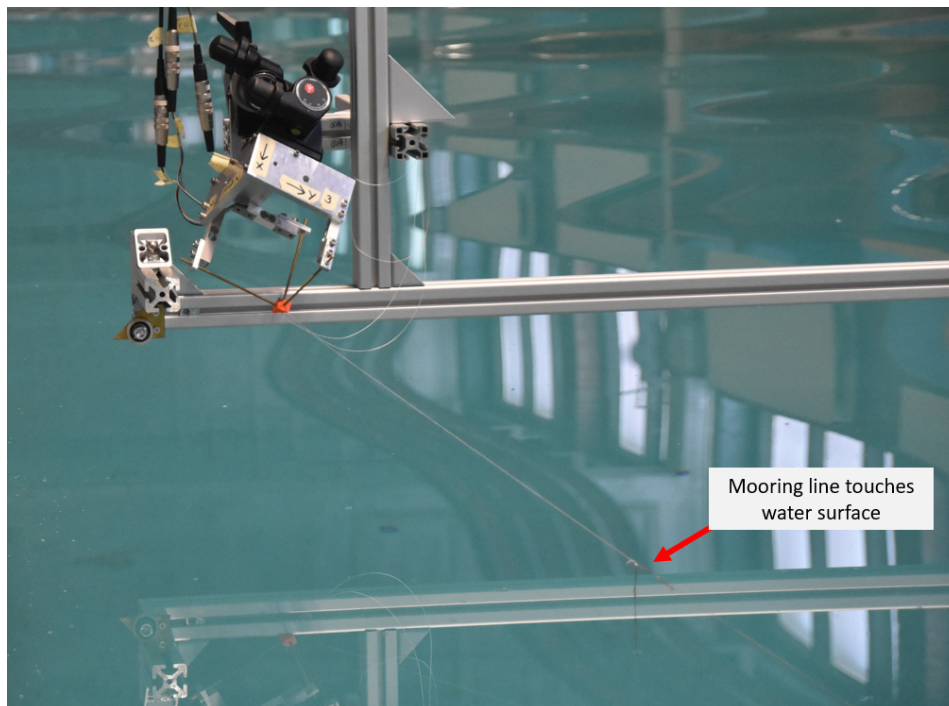


Figure 7.11: Mooring line orientation

In figure 7.12, the total mooring line force is shown. As a mooring line only can transfer tension loads, the total force is always positive. The maximum force is around 0.18N and the total force has a

period similar to the wave period. The static force contribution is around 0.06N and with a dynamical part of around 0.06N.

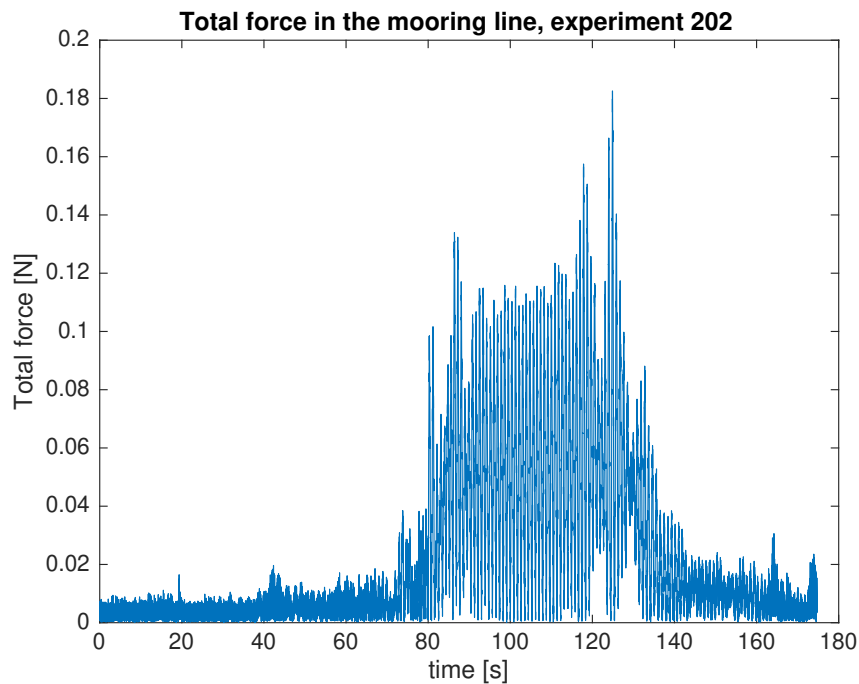
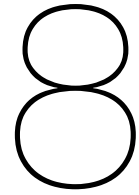


Figure 7.12: Total mooring force for experiment 202

#### 7.4.4. Discussion and Conclusions of example application

The goal of this example application is to prove the sensor frame usability. From the results it was found that the force orientation is not exactly matching the mooring line orientation. The mooring line orientation changes during the experiments and therefore it cannot be checked easily. Additionally, the results showed that the maximum total mooring force is around 0.18N, while in the mooring force estimation, a maximum force of around 0.6N was determined. The measured force is close to the expected estimated force, but with a different floating structure and different wave conditions it does not exactly match. The sensors in the sensor frame have a maximum range of 20N. And as expected, the sensors are loaded far below their maximum capacity and therefore the noise in the output data is relatively large. For new research, the sensor range and the expected force should be matched better. It can be concluded that the sensor frame is working as expected under real conditions. The sensor frame can be installed in an experimental setup for floating structures, and it is possible to determine the orientation of the sensor frame in the setup by calculating the rotation matrix. The pretension in the mooring lines can be kept well by performing experiments with and without the structure. The sensor is able to measure the mooring forces during an experiment in all global directions, and by combining these mooring forces, the total force with direction can be determined.



## Discussion

In this project, a sensor frame is developed to measure mooring forces on flexible floating structures. The design of this sensor is a new design and tested for its performance. As this sensor is a new design, challenges during the developing process were observed. The main discussions are described below.

First of all, the concept selection. During the concept development, the design with the sensor positioned above the water was selected. The position of the sensor determines in large extent the feasible experiments. To perform experiments with catenary mooring lines, the sensor should be positioned at the bottom of the towing tank. However, the sensor is not designed for submerged conditions and requires adaptations for measuring at this position.

From the experimental data, the calibration matrix for the complete sensor frame is obtained. The results of the sensor frame show that the obtained calibration matrix does not correspond exactly with the theoretical calibration matrix. The regression parameters on the main diagonal are increased, where they were expected to decrease in the theoretical calibration matrix. Additionally, the off diagonal values are larger in the experimental results than theoretically determined and the sign is for some off diagonal values different. Thus, for the fabricated sensor frame, other effects than expected occurred during experiments, e.g. misalignments and internal tensions. An example of the misalignments is caused by the camera ball head. When loaded, the camera ball head suffers from deflections. These deflections can cause deviations up to 1%.

The results showed that the pulley system in the calibration setup causes large errors in the measurements. The pulley system induces a hysteresis in the sensor. Due to this hysteresis, the performance of the full upright calibration matrix and single sensor calibration matrix is less than the full rotated calibration matrix. With an improved pulley system, the performance of these two matrices will most likely also improve.

In the results of the full calibration matrices, the residuals showed a periodicity. To ensure that this periodicity is not caused by the scheme of applying forces, the weights should be applied in different schemes. In this project the weights in the X and Z direction were constant during an experiment and the weight in the Y direction was stacked. With new experiments the weights should also be stacked in the X and Z direction.

To ensure that the sensor frame including the force sensors are working as expected, the output values are monitored between experiments. After the sensor frame is calibrated, the behavior of the frame is defined. The behavior of this frame can change due to an overloaded sensor or a deformation of the frame. In case the behavior changes, the calibration of the sensor frame should be repeated. Therefore, care must be taken when handling the frame.

In the example application, mooring forces are measured on the flexible floating structure. To validate the direction of the mooring force, it was compared with the geometrical direction of the mooring line. However, it was observed that this geometrical direction was not identical to the direction in the setup. Due to this difference it was not possible to compare the direction of the measured force accurately.

The mooring forces measured in the example application had a magnitude of around 0.18N. Together with the pretension of 0.07N, the total force in the mooring line is approximately 0.25N for the tested floating structure. The sensor frame is equipped with force sensors with a range of 20N. As the force sensor are seriously oversized, the results contain as expected a large noise. For a balanced sensor, the force sensors should be selected according to the expected force which can also imply that different sized force sensors are required.

# 9

## Conclusions

In this project, a new force sensor is developed that is able to measure the forces in a mooring line including the orientation. The setup is equipped with a total of three force sensors, by which the direction and the magnitude of the force are measured. The development of this setup accomplished the goal of this project: *'Develop an instrumented mooring system for flexible floating structures at model scale for the towing tank No. 1 at the TU Delft and determine its accuracy'*. To determine the accuracy of the setup and to meet the requirements of the system described in section 1.2.1, first the research questions are answered.

The main research question was: *'How does the accuracy of the proposed system depend on its sensor configuration and the calibration procedure and how can the accuracy be optimized to acceptable levels?'*. And this question was divided into two sub questions.

*'What is the effect of the force sensor configuration on the accuracy and what is the optimal configuration taken into account the accuracy and the usability'*. From the theory it was determined how an applied force is divided over the force sensors of the frame. Next to this distribution, it was found from experiments that the force sensor has the highest accuracy in its sensitive direction. With these two parameters, the influence of the sensor configuration on the accuracy is known and can be optimized to increase the accuracy. To increase the accuracy of the sensor frame, the length of the threaded rods should be increased. As the sensor frame is used in a towing tank, the sensor frame dimensions are limited.

*'What are feasible calibration procedures and what is the accuracy of each procedure'*. In this project, three different types of calibration procedures are investigated. With calibration experiments, the performance of each procedure is tested. First, the single sensor and full upright matrix were investigated. These experiments showed that the accuracy was better for the full upright matrix. For a random set of data points the accuracy of the full upright matrix was less than 1%, whereas it was around 5% for the single sensor matrix. Next, the full rotated matrix was investigated as well for a situation where the sensor frame was rotated. For another random set of data points, the accuracy of the full rotated matrix gave the best results of all three matrices. Nonetheless, it was shown that the calibration procedure for the full upright matrix requires less effort and the results for the full upright matrix could be improved. The calibration procedure for the full upright matrix is performed in a workshop with stable conditions and has to be performed only once, whereas the calibration procedure for the full rotated matrix has to be performed at the experimental setup. Also the results of the full upright matrix can be optimized with a better pulley system.

As the obtained calibration matrices deviate strongly from the theoretical calibration matrix, it is concluded that the calibration matrix should be obtained by experiments with the complete sensor frame. With these observations, it is concluded that the full upright matrix procedure is the optimal procedure, while keeping in mind that this procedure still has to be optimized.

Now if we look back at the goal and the design requirements for this project, we can observe that two of the three requirements are met. First of all, the system is able to measure the magnitude and the direction of the mooring force. Secondly, it is able to measure forces on a flexible floating structure in the towing tank No. 1 at the TU Delft. The requirement for the accuracy between 0.1%FS - 0.3%FS is not met. From the random set of data points for the rotated position, it was observed that the accuracy is around 10%. This accuracy is determined for the actual applied force and not the full scale (FS), still the accuracy is around 10% for the FS. It was also observed that this large deviation of accuracy can be improved with a better calibration setup. Still, an improved calibration setup will likely return an accuracy of around 1%FS, similar to the accuracy in the upright position, which does not meet the requirement. To further improve the accuracy, calibration experiments at a smaller force range can be performed.

With the example application, it is proven that the sensor frame can be used in the towing tank to measure mooring forces on flexible floating structures. With an additional frame and simple experiments, the orientation of the sensor can be determined in the setup. Pretension in the mooring lines can be controlled before experiments are performed. And finally, the system is able to measure fluctuating mooring forces on a flexible floating structure under wave loading conditions.

In this project a sensor frame is developed. First, a concept is selected, whereafter it was fabricated and tested. The sensor frame made it possible to measure mooring forces with direction and is easy in use. Next to the sensor frame, a calibration setup is developed. This calibration setup is equipped with pulley systems to investigate the complete range of the sensor. Additionally, this setup allowed to position the sensor frame in the upright and rotated position. The sensor frame designed in this project forms a good base for an instrumented mooring system for flexible floating structures and is provided with a clear calibration procedure to determine the accuracy of the setup. With additional research, the two most important improvements can be realized: adapt the sensor range according the expected mooring force and improve the pulley system with low friction pulleys.

## Future work and improvements

As the sensor frame designed in this project forms a base for new research, recommendations about design improvements, procedure improvements and instructions for future work are listed in this chapter.

First of all, the design of the sensor frame. An improvement is the installation of the threaded bars. The threaded bars combine the connection block with the force sensors. Preferably, these threaded bars are installed orthogonal. In practice, the bars are adjusted with small screw-nuts and on sight. Thus, small misalignments of the threaded bars are expected.

Additionally, misalignments are caused by the flexibility of the camera ball head. This can be improved by replacing the camera ball head with a fixed and stiff structure. In practice, the sensor frame should be rotated in a single rotated position and this can be accomplished with a rigid block too.

Another improvement is the pulley system. During the experiments it was concluded that the pulley system introduces large errors. By redesigning the pulley system with low friction, these errors can be reduced.

Finally, an improvement is the usability of the sensor. The sensor frame is designed for the location just above the water surface. To make the sensor frame suitable for submerged conditions as well, the sensors should be made water resistant without influencing the behaviour of the sensor frame. With a submerged sensor, catenary mooring line configurations can be investigated.

Secondly, procedure improvements are listed. For the calibration experiments, attention should be paid on the start and end of an experiment. For processing the results efficiently, each experiment should have a similar starting time and stacking of the weights should be started at a similar time.

Furthermore, improvements can be done into the influence of the misalignments. As mentioned, different misalignments are introduced by the design and procedure. When the extent of the misalignment is known, an additional accuracy can be given to the results.

For the single sensor regression parameters, a confidence interval was determined. This interval indicates how accurate the sensor is able to measure forces. For the multi regression analysis with multiple sensors, this confidence interval is not indicated. In chapter 5 of [24], a method to determine the confidence interval is initiated. This method explains the confidence interval for a single output value. For the sensor frame in this project, this method should be extended to determine the confidence interval of the input values.

Lastly, recommendations for the instructions are made. For the calibration experiments in this research, it was concluded that the regression matrix from single sensor parameters resulted in a sensor which is not accurate. Therefore, the parameters of the sensor frame should not be determined with single sensor parameters. Experiments with a single sensor should only be used to verify the parameters specified by the supplier or to check if the sensor is in good conditions.

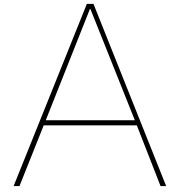
Before the sensor is used in a setup, it should be verified that the range of the sensor is matching while at the same time the mooring line force and orientation is not exceeding the sensor range.

# Bibliography

- [1] 28th ITTC. 7.5-01-03-01 Uncertainty Analysis, Instrument Calibration. *ITTC – Recommended Procedures and Guidelines Uncertainty*, page 17, 2017. URL <https://www.ittc.info/media/7979/75-01-03-01.pdf>.
- [2] José Azcona, Xabier Munduate, Leo González, and Tor A Nygaard. Experimental validation of a dynamic mooring lines code with tension and motion measurements of a submerged chain. *Ocean Engineering*, 129(February 2016):415–427, 2017. ISSN 0029-8018. doi: 10.1016/j.oceaneng.2016.10.051.
- [3] Carlos Barrera, Raúl Guanche, and Iñigo J Losada. Experimental modelling of mooring systems for floating marine energy concepts. *Marine Structures*, 63(October 2018):153–180, 2019. ISSN 0951-8339. doi: 10.1016/j.marstruc.2018.08.003.
- [4] W T Bruinsma, J L Cramer, A Gerritsen, and S H Hoogervorst. The Effect of Bending Stiffness on Wave-Induced Drift of Thin Flexible Plates. *Not published*, (December), 2020.
- [5] Yunus A. Cengel and John M. Cimbala. *Fluid mechanics fundamentals and applications*. Mc Graw Hill Higher Education, 2005.
- [6] Xujun Chen, Torgeir Moan, Shixiao Fu, and Weicheng Cui. Hydroelastic Analysis of Flexible Floating Structures in Regular Waves. *Proceedings of ICMEM2005*, 34(11-12):973–977, 2005.
- [7] Shanna R Daly, Colleen M Seifert, and Richard Gonzalez. Comparing Ideation Techniques for Beginning Designers. (September), 2016. doi: 10.1115/1.4034087.
- [8] Montserrat Gómez Delgado and Joaquín Bosque Sendra. Sensitivity analysis in multicriteria spatial decision-making: A review. *Human and Ecological Risk Assessment*, 10(6):1173–1187, 2004. ISSN 10807039. doi: 10.1080/10807030490887221.
- [9] Daniele Dessi and Sara Siniscalchi Minna. Experimental investigation VS numerical simulation of the dynamic response of a moored floating structure to waves. *Proceedings of the International Conference on Offshore Mechanics and Arctic Engineering - OMAE*, 8B:153–165, 2014. doi: 10.1115/OMAE2014-24064.
- [10] R. Ding, C. R. Liu, H. C. Zhang, D. L. Xu, Q. J. Shi, D. L. Yan, W. Y. Yang, W. P. Chen, and Y. S. Wu. Experimental investigation on characteristic change of a scale-extendable chain-type floating structure. *Ocean Engineering*, 213(July), 2020. ISSN 00298018. doi: 10.1016/j.oceaneng.2020.107778.
- [11] Amy Gallo. *A Refresher on Regression Analysis*, 2015. ISSN 01000000.
- [12] H. Leo Holthuijsen. *Waves in Oceanic and Coastal Waters*. Cambridge: Cambridge University Press, 2007.
- [13] ITTC. 7.6-02-09-Calibration of Load Cells. pages 1–25, 2002.
- [14] Kern. Manual Kern 440 scale, 2017.
- [15] Neil Kitney and David T Brown. Experimental Investigation of Mooring Line Loading Using Large and Small-Scale Models. 123(February):1–9, 2001. doi: 10.1115/1.1342159.
- [16] Miguel Lamas-Pardo, Gregorio Iglesias, and Luis Carral. A review of Very Large Floating Structures (VLFS) for coastal and offshore uses. *Ocean Engineering*, 109:677–690, 2015. ISSN 00298018. doi: 10.1016/j.oceaneng.2015.09.012.

- [17] Eva Loukogeorgaki, Oral Yagci, and M. Sedat Kabdasli. 3D Experimental investigation of the structural response and the effectiveness of a moored floating breakwater with flexibly connected modules. *Coastal Engineering*, 91:164–180, 2014. ISSN 03783839. doi: 10.1016/j.coastaleng.2014.05.008.
- [18] Kai-Tung Ma, Yong Luo, Thomas Kwan, and Yongyan Wu. Mooring analysis. *Mooring System Engineering for Offshore Structures*, pages 85–114, 2019. doi: 10.1016/b978-0-12-818551-3.00005-3.
- [19] Celso K. Morooka and Raphael I. Tsukada. Experiments with a steel catenary riser model in a towing tank. *Applied Ocean Research*, 43:244–255, 2013. ISSN 01411187. doi: 10.1016/j.apor.2013.10.010.
- [20] National instruments. PXI Express Chassis, .
- [21] National instruments. PXI Analog I / O, .
- [22] E. Peña, J. Ferreras, and F. Sanchez-Tembleque. Experimental study on wave transmission coefficient, mooring lines and module connector forces with different designs of floating breakwaters. *Ocean Engineering*, 38(10):1150–1160, 2011. ISSN 00298018. doi: 10.1016/j.oceaneng.2011.05.005.
- [23] Hongde Qin, Zhijing Xu, Peng Li, and Songchen Yu. A physical model approach to nonlinear vertical accelerations and mooring loads of an offshore aquaculture cage induced by wave-structure interactions. *Ocean Engineering*, 197(November 2019):106904, 2020. ISSN 00298018. doi: 10.1016/j.oceaneng.2019.106904.
- [24] John O. Rawlings, Sastry G. Pantula, and David A. Dickey. *Applied Regression Analysis: A Research Tool*, volume 41. 1990. ISBN 0387984542. doi: 10.2307/2583482.
- [25] Paulo Rosa-Santos, Francisco Taveira-Pinto, and Fernando Veloso-Gomes. Experimental evaluation of the tension mooring effect on the response of moored ships. *Coastal Engineering*, 85: 60–71, 2014. ISSN 03783839. doi: 10.1016/j.coastaleng.2013.11.012.
- [26] Sebastian Schreier and Gunnar Jacobi. Experimental investigation of wave interaction with a thin floating sheet. *Proceedings of the International Offshore and Polar Engineering Conference*, 2020-Octob:2479–2488, 2020. ISSN 15551792.
- [27] Yugao Shen, Marilena Greco, Odd M. Faltinsen, and Ivar Nygaard. Numerical and experimental investigations on mooring loads of a marine fish farm in waves and current. *Journal of Fluids and Structures*, 79(7491):115–136, 2018. ISSN 10958622. doi: 10.1016/j.jfluidstructs.2018.02.004.
- [28] Michael Spackman, Alan D Pearman, and Lawrence D Phillips. *Multi-Criteria Analysis : A Manual Multi-criteria analysis : a manual*. Number January. 2009. ISBN 9781409810230.
- [29] H. Suzuki, T. A. Shugar, B. Bhattacharya, H. R. Riggs, H. Seto, D. A. Hudson, M. Fujikubo, Y. Yasuzawa, and H. Shin. Very large floating structures. *Proceedings of the International Conference on Offshore Mechanics and Arctic Engineering - OMAE*, 2(July 2014):597–608, 2007. doi: 10.1115/OMAE2007-29758.
- [30] Zahra Tajali and Mehdi Shafieefar. Hydrodynamic analysis of multi-body floating piers under wave action. *Ocean Engineering*, 38(17-18):1925–1933, 2011. ISSN 0029-8018. doi: 10.1016/j.oceaneng.2011.09.025.
- [31] Kim Trapani. FLEXIBLE FLOATING THIN FILM PHOTOVOLTAIC ( PV ) ARRAY CONCEPT FOR MARINE AND LACUSTRINE ENVIRONMENTS by Kim Trapani Thesis submitted in partial fulfillment of the requirements for the degree of Doctor of Philosophy ( PhD ) in Natural Resources Engineering. 2014.
- [32] Roscoe B White. Nonlinear Behavior. *The Theory of Toroidally Confined Plasmas*, (January): 191–235, 2001. doi: 10.1142/9781848161412{\\_\}0006.

- 
- [33] Sheng Xu, Chun yan Ji, and C. Guedes Soares. Experimental and numerical investigation a semi-submersible moored by hybrid mooring systems. *Ocean Engineering*, 163(June):641–678, 2018. ISSN 00298018. doi: 10.1016/j.oceaneng.2018.05.006.
- [34] Zemic Europe BV. Type Q45 Miniature Sensor Type Q45 Miniature Sensor, 2015.
- [35] Su Xia Zhang, You Gang Tang, and Xi Jun Liu. Experimental investigation of nonlinear dynamic tension in mooring lines. *Journal of Marine Science and Technology (Japan)*, 17(2):181–186, 2012. ISSN 09484280. doi: 10.1007/s00773-012-0160-7.



# Concept development

## A.1. Morphological chart

With the use of the morphological chart, concepts for the instrumented mooring system are created. Each concept is a combination of one solution per function, unfeasible concepts are neglected and not investigated. Figure A.1 shows the morphological chart with all possible combinations. In the figure, it can be observed that only a few concepts are created with the third solution of function 3.

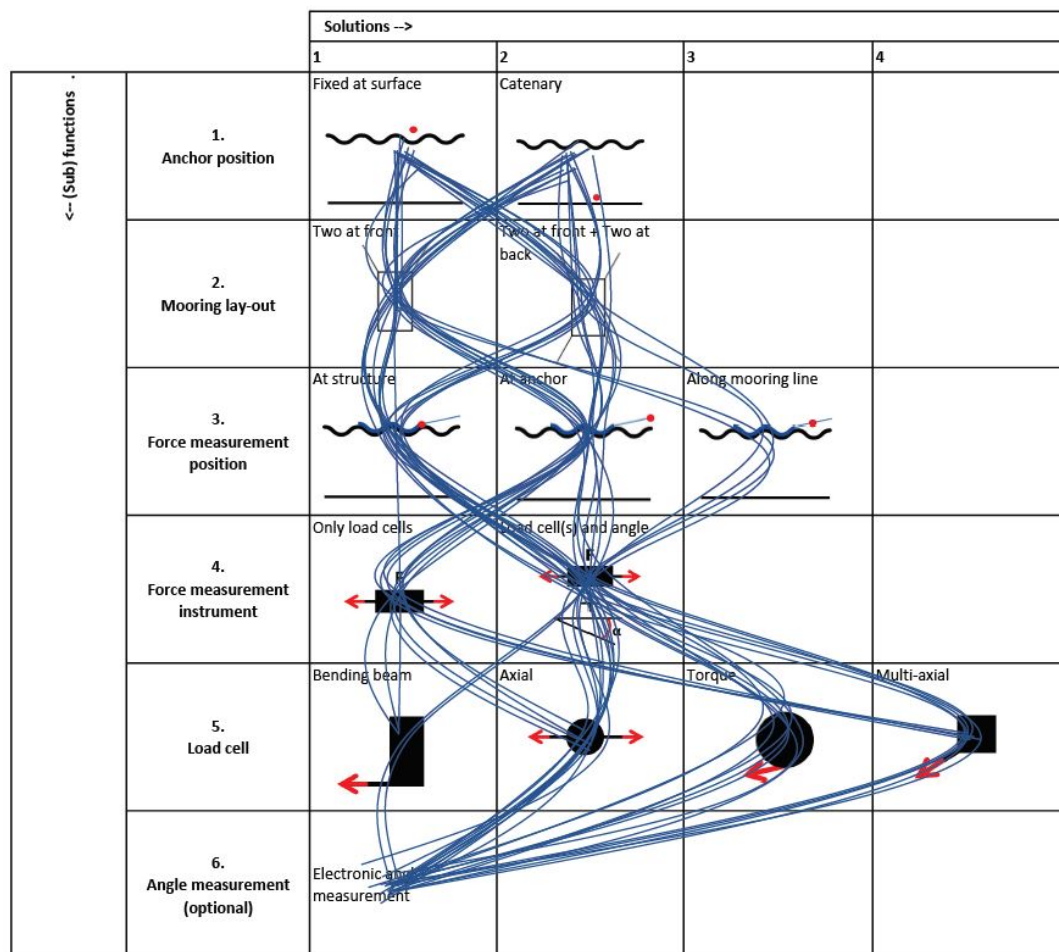


Figure A.1: Morphological chart with visualized concept determination

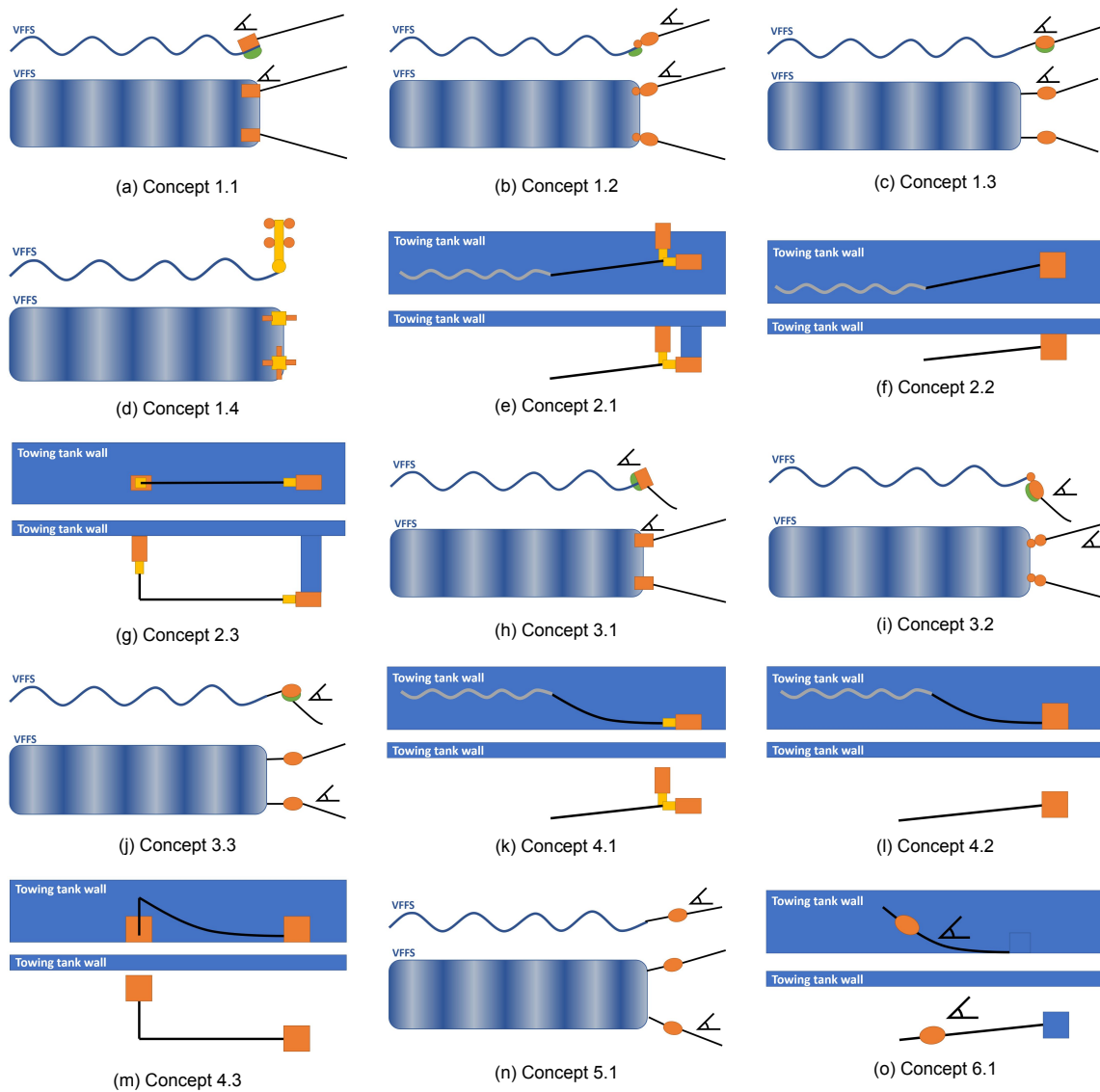


Figure A.2: Concepts created with MC, for each sub figure top: side view, bottom: top view. With blue the towing tank wall is illustrated, the orange and yellow blocks represent the measurement instruments and black represent the mooring line

## A.2. MCA

### A.2.1. Weight factors

The weight factors are determined with the mutual ratios. In table A.1, all criteria are compared with each other. If the criterion on the left column is rated more important than the criterion on the top row, the crossing cell is 1 and 0 otherwise. The comparison of the criteria are determined based on the requirements and problems of the system. Criteria that are strongly connected to a requirement are assumed to be important. This procedure results in a ranking of criteria, and with this ranking the weight factors are determined. As this ranking system depends on empirical values, a sensitivity analysis is performed later in the concept development.

Table A.1: Weight factors, determined with mutual ratios

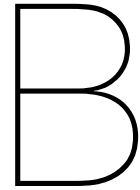
	Accuracy	External effects	Impact on structure response	Range/scalability	Impact on wave loading conditions	Usability/user friendly	Dismountable	Simplicity	Cost	Calibration	Mutual ratio	Weight factor
Accuracy	1	0	0	1	1	1	1	1	1	1	8	0.15
External effects	1	1	0	1	1	1	1	1	1	1	9	0.16
Impact on structure response	1	1	1	1	1	1	1	1	1	1	10	0.18
Range/scalability	0	0	0	1	0	1	1	1	1	1	6	0.11
Impact on wave loading conditions	0	0	0	1	1	1	1	1	1	1	7	0.13
Usability/user friendly	0	0	0	0	0	1	1	1	0	1	4	0.07
Dismountable	0	0	0	0	0	0	1	0	0	0	1	0.02
Simplicity	0	0	0	0	0	0	1	1	0	0	2	0.04
Cost	0	0	0	0	0	1	1	1	1	1	5	0.09
Calibration	0	0	0	0	0	0	1	1	0	1	3	0.05

**A.2.2. MCA graded**

Figure A.3 shows the MCA for all concepts, the grades are determined with the grading rubric.

	Accuracy	External effects	Impact on structure response	Range/scalability	Impact on wave loading conditions	Usability/user friendly	Dismountable	Simplicity	Cost	Calibration	Total score
Weight factor	0.15	0.16	0.18	0.11	0.13	0.07	0.02	0.04	0.09	0.05	
Concept 1.1	1	2	0	2	0	0	2	0	1	0	0.82
Concept 1.2	1	2	1	2	1	0	2	0	1	0	1.13
Concept 1.3	1	1	1	1	0	0	2	0	1	0	0.73
Concept 1.4	2	2	0	1	1	1	1	1	1	1	1.13
Concept 2.1	2	1	2	2	0	1	2	1	2	1	1.42
Concept 2.2	2	1	2	1	0	2	2	2	1	2	1.38
Concept 2.3	1	1	2	2	0	1	2	1	2	0	1.22
Concept 3.1	1	2	0	2	0	0	2	0	1	0	0.82
Concept 3.2	1	2	1	2	1	0	2	0	1	0	1.13
Concept 3.3	1	1	1	1	0	0	2	0	1	0	0.73
Concept 4.1	2	0	1	2	2	1	2	1	2	1	1.34
Concept 4.2	2	0	1	2	2	1	2	2	1	1	1.29
Concept 4.3	1	0	1	2	2	0	2	0	0	0	0.85
Concept 5.1	1	1	1	2	1	0	2	0	1	0	0.97
Concept 6.1	1	1	1	2	1	0	2	0	1	0	0.97

Figure A.3: Complete MCA, all concepts graded for the criteria



## Calibration example

<b>Sensor properties</b>							
	Sensitivity sensitive direction	Measurable sensitivity	Total sensitivity sensitive direction	Sensitivity non-sensitive direction	Measurable sensitivity	Total sensitivity non-sensitive direction	
Sensor 1	0.95	1	0.95	0.025	0.05	0.00125	
Sensor 2	0.95	1	0.95	0.025	0.05	0.00125	
Sensor 3	0.95	1	0.95	0.025	0.05	0.00125	

<b>Full regression matrix</b>			<b>Simplified regression matrix</b>		
<b>Regression slope matrix</b>			<b>Regression slope matrix</b>		
0.95	0.00125	0.00125	0.95	0	0
0.00125	0.95	0.00125	0	0.95	0
0.00125	0.00125	0.95	0	0	0.95
<b>Inverse regression slope matrix</b>			<b>Inverse regression slope matrix</b>		
1.05	-0.0014	-0.0014	1.05	0	0
-0.0014	1.05	-0.0014	0	1.05	0
-0.0014	-0.0014	1.05	0	0	1.05

### Example measurement

Output, voltage

X-dir	Y_dir	Z-dir
1	0	0
0.5	0	0
0.2	0	0
0	1	0
0	0.5	0
0	0.2	0
0	0	1
0	0	0.5
0	0	0.2
1	1	1
0.5	0.5	0.5
1	1	0.5
1	0.5	0.1
1	0.2	0.1
1	0.1	0.1
1	1	0.1
0.1	0.1	0.1

Input, weight, full regression matrix

X-dir	Y-dir	Z-dir
1.05	-0.0014	0.00
0.53	0.00	0.00
0.21	0.00	0.00
0.00	1.05	0.00
0.00	0.53	0.00
0.00	0.21	0.00
0.00	0.00	1.05
0.00	0.00	0.53
0.00	0.00	0.21
1.05	1.05	1.05
0.52	0.52	0.52
1.05	1.05	0.52
1.05	0.52	0.10
1.05	0.21	0.10
1.05	0.10	0.10
1.05	1.05	0.10
0.10	0.10	0.10

Input, weight, simplified regression matrix

X-dir	Y-dir	Z-dir
1.05	0.00	0.00
0.53	0.00	0.00
0.21	0.00	0.00
0.00	1.05	0.00
0.00	0.53	0.00
0.00	0.21	0.00
0.00	0.00	1.05
0.00	0.00	0.53
0.00	0.00	0.21
1.05	1.05	1.05
0.53	0.53	0.53
1.05	1.05	0.53
1.05	0.53	0.11
1.05	0.21	0.11
1.05	0.11	0.11
1.05	1.05	0.11
0.11	0.11	0.11

**Difference [%] = (full regr - simplified regr)/full regr**

X-dir	Y-dir	Z-dir
<b>0.00</b>	<b>100.00</b>	<b>100.00</b>
<b>0.00</b>	<b>100.00</b>	<b>100.00</b>
<b>0.00</b>	<b>100.00</b>	<b>100.00</b>
<b>100.00</b>	<b>0.00</b>	<b>100.00</b>
<b>100.00</b>	<b>0.00</b>	<b>100.00</b>
<b>100.00</b>	<b>0.00</b>	<b>100.00</b>
<b>100.00</b>	<b>100.00</b>	<b>100.00</b>
<b>100.00</b>	<b>100.00</b>	<b>100.00</b>
<b>100.00</b>	<b>100.00</b>	<b>100.00</b>
<b>-0.26</b>	<b>-0.26</b>	<b>-0.26</b>
<b>-0.26</b>	<b>-0.26</b>	<b>-0.26</b>
<b>-0.20</b>	<b>-0.20</b>	<b>-0.53</b>
<b>-0.08</b>	<b>-0.29</b>	<b>-2.01</b>
<b>-0.04</b>	<b>-0.73</b>	<b>-1.60</b>
<b>-0.03</b>	<b>-1.47</b>	<b>-1.47</b>
<b>-0.14</b>	<b>-0.14</b>	<b>-2.70</b>
<b>-0.26</b>	<b>-0.26</b>	<b>-0.26</b>

C

Test setup details

## C.1. Sensor frame drawings

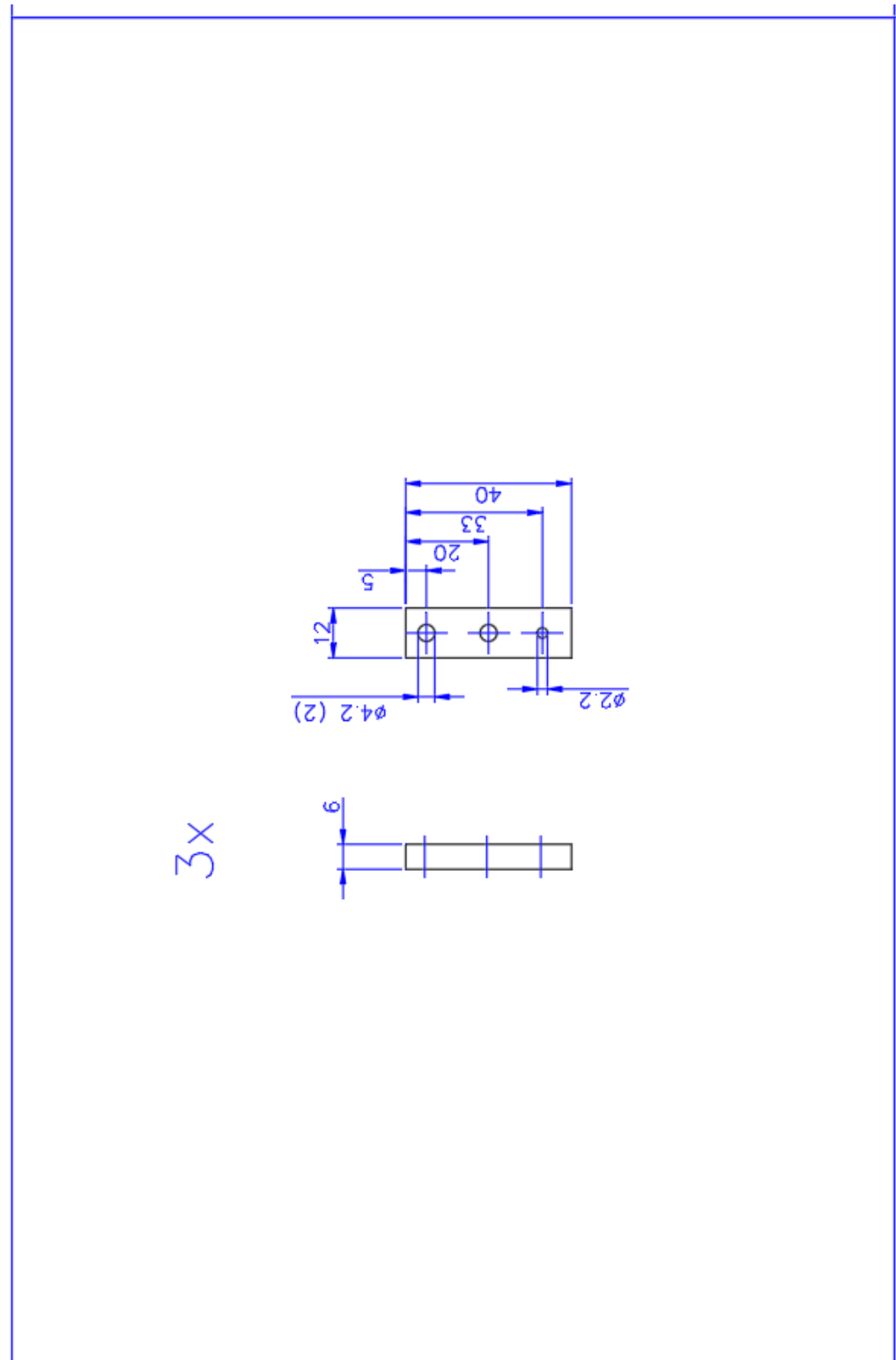


Figure C.1: Extension plate

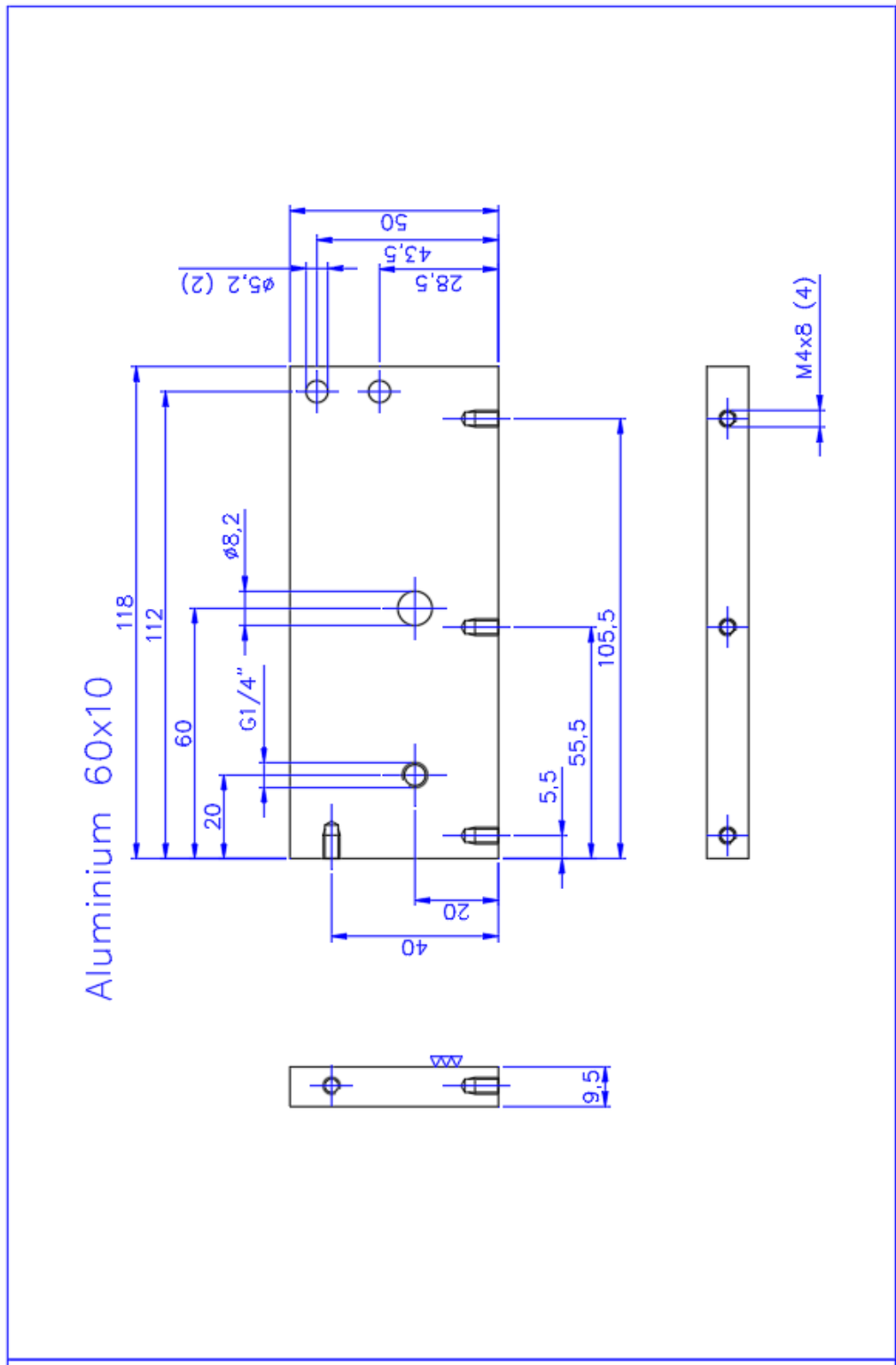


Figure C.2: Sensor frame plate 1

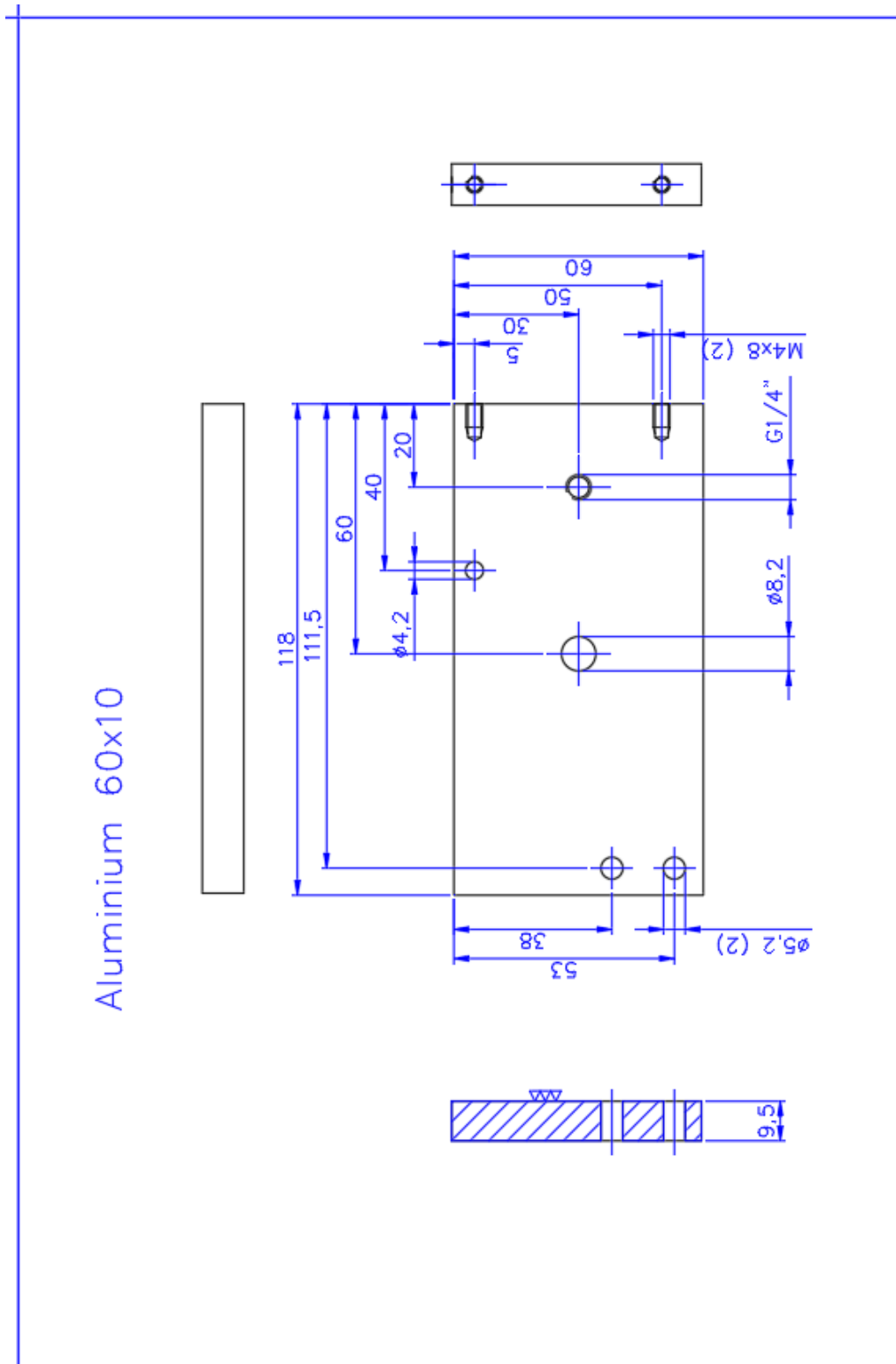


Figure C.3: Sensor frame plate 2

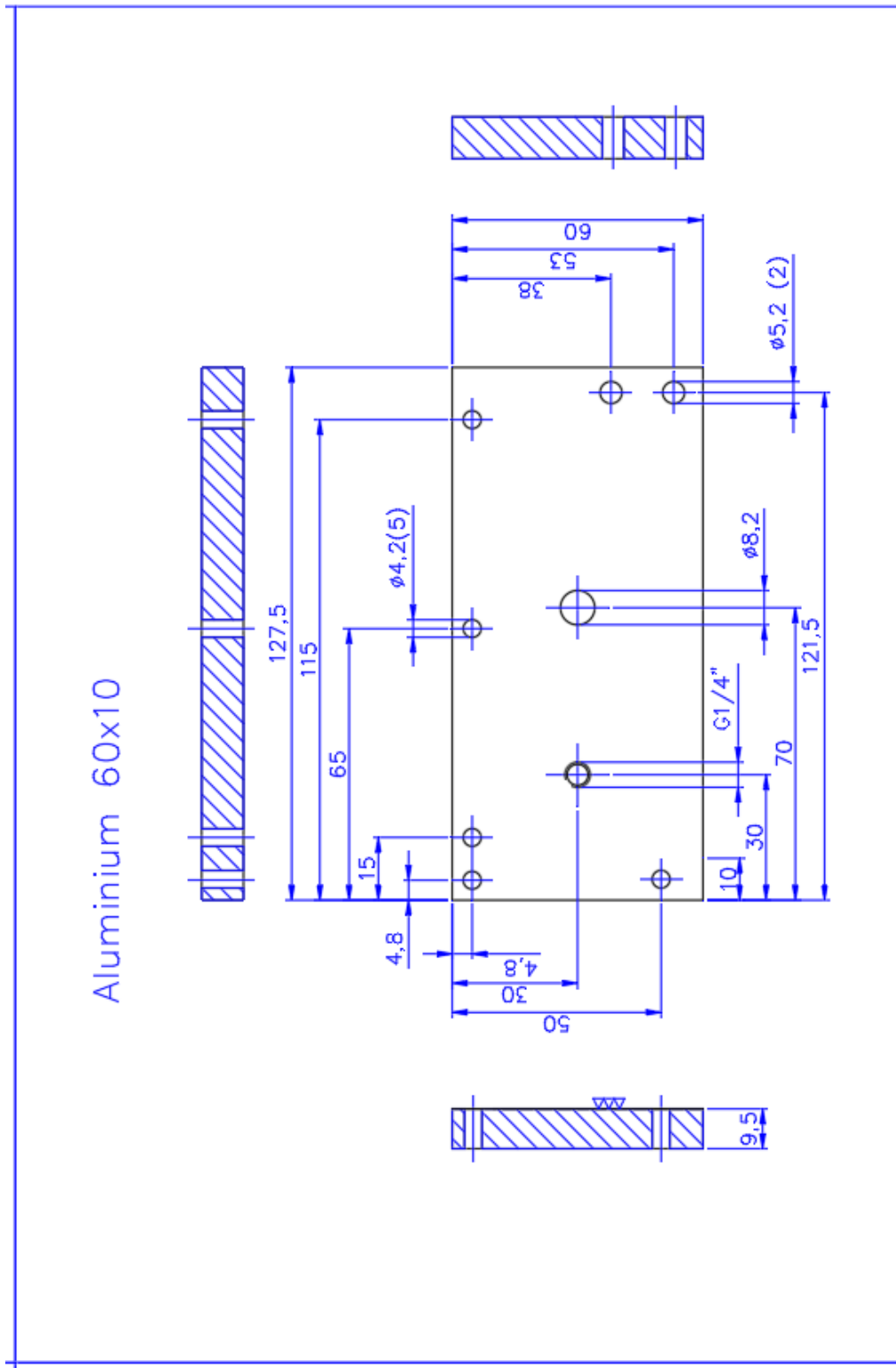
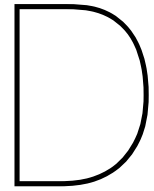
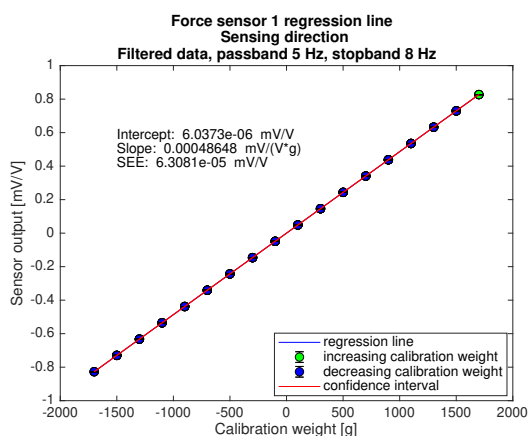


Figure C.4: Sensor frame plate 3

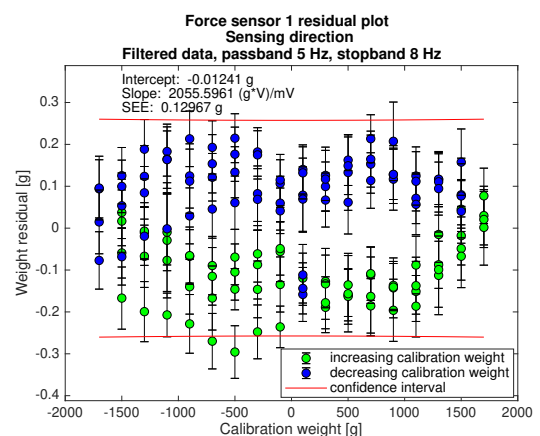


# Results

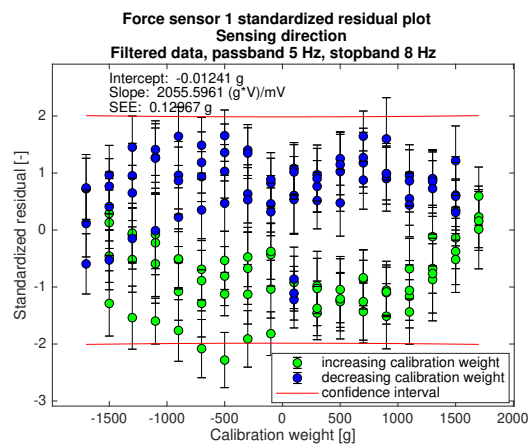
## D.1. Regression analysis single sensor 1



(a) Regression line for sensor 1 in M axis

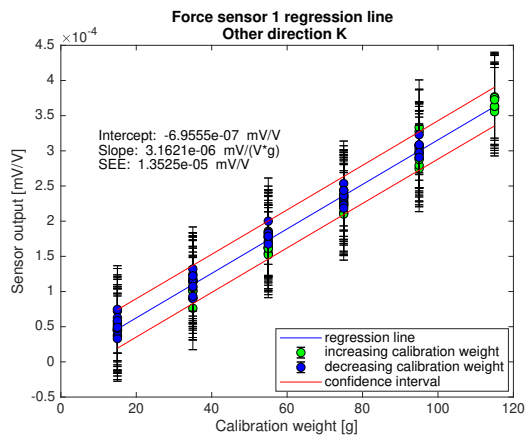


(b) Residual for sensor 1 in M axis

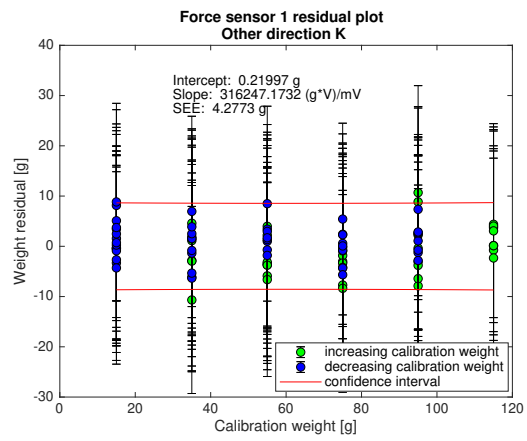


(c) Standard residual for sensor 1 in M axis

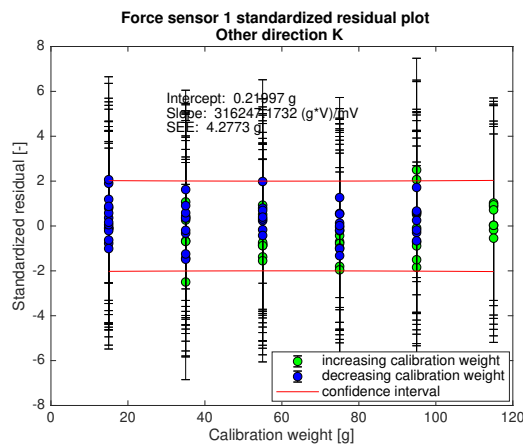
Figure D.1: Sensor regression analysis results, M axis



(a) Regression line for sensor 1 in K axis

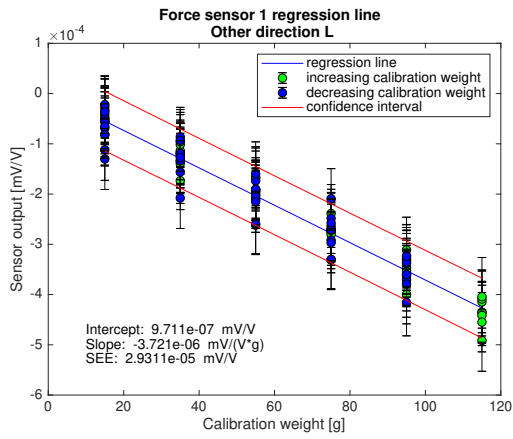


(b) Residual for sensor 1 in K axis

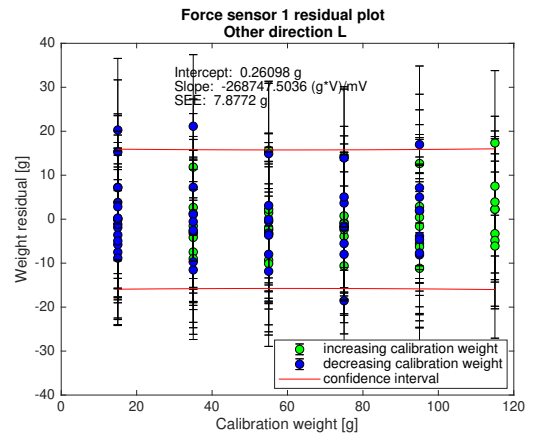


(c) Standard residual for sensor 1 in K axis

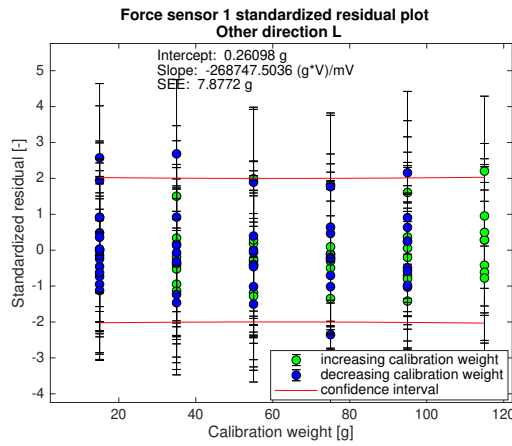
Figure D.2: Sensor regression analysis results, K axis



(a) Regression line for sensor 1 in L axis



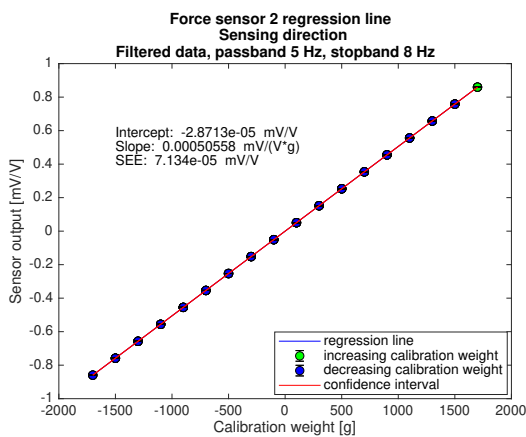
(b) Residual for sensor 1 in L axis



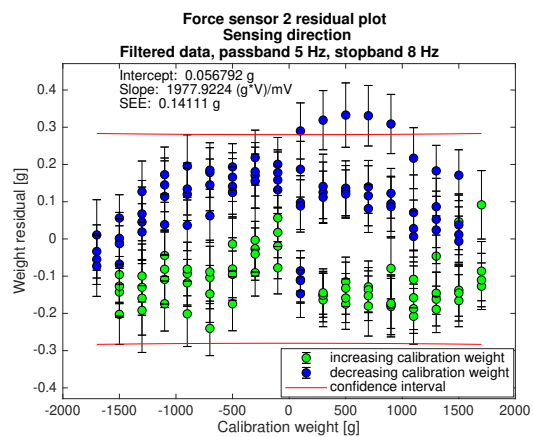
(c) Standard residual for sensor 1 in L axis

Figure D.3: Sensor regression analysis results, L axis

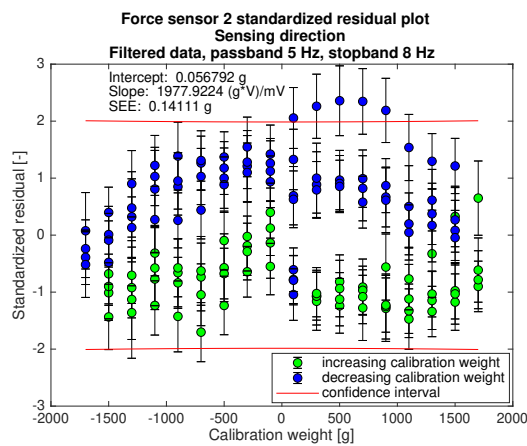
## D.2. Regression analysis single sensor 2



(a) Regression line for sensor 2 in M axis

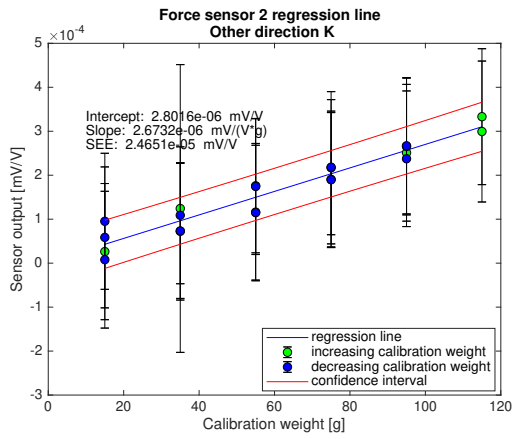


(b) Residual for sensor 2 in M axis

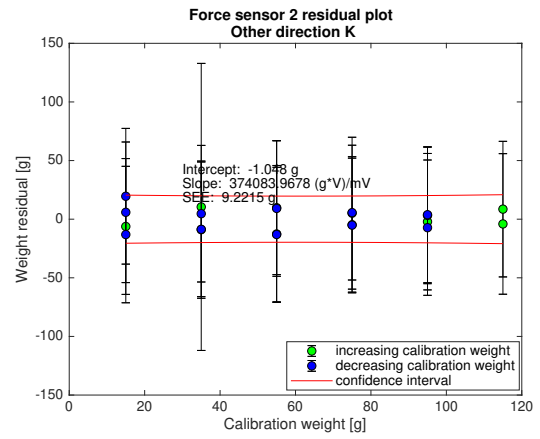


(c) Standard residual for sensor 2 in M axis

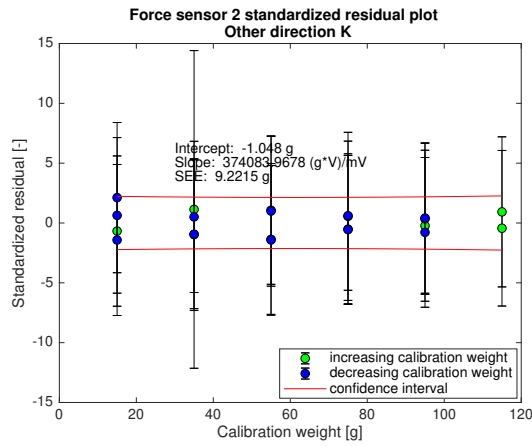
Figure D.4: Sensor regression analysis results, M axis



(a) Regression line for sensor 2 in K axis

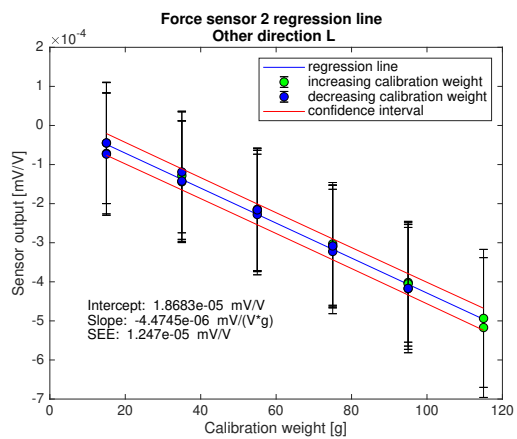


(b) Residual for sensor 2 in K axis

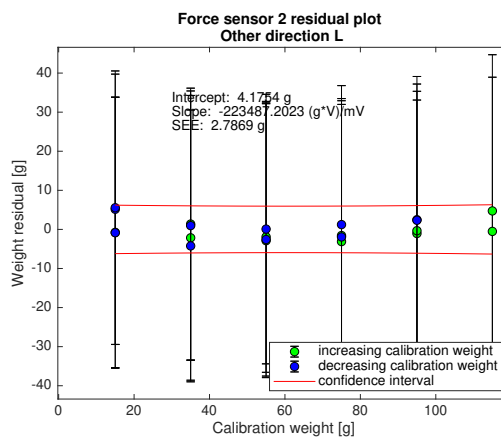


(c) Standard residual for sensor 2 in K axis

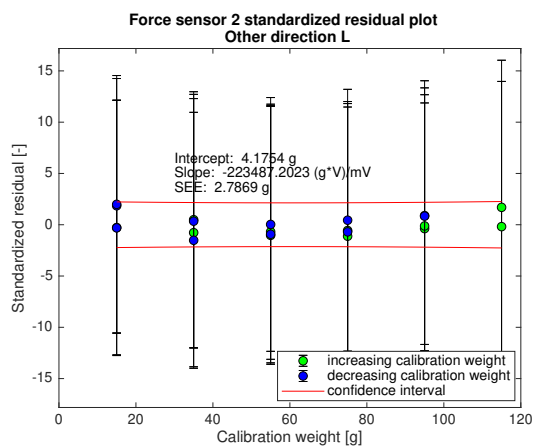
Figure D.5: Sensor regression analysis results, K axis



(a) Regression line for sensor 2 in L axis



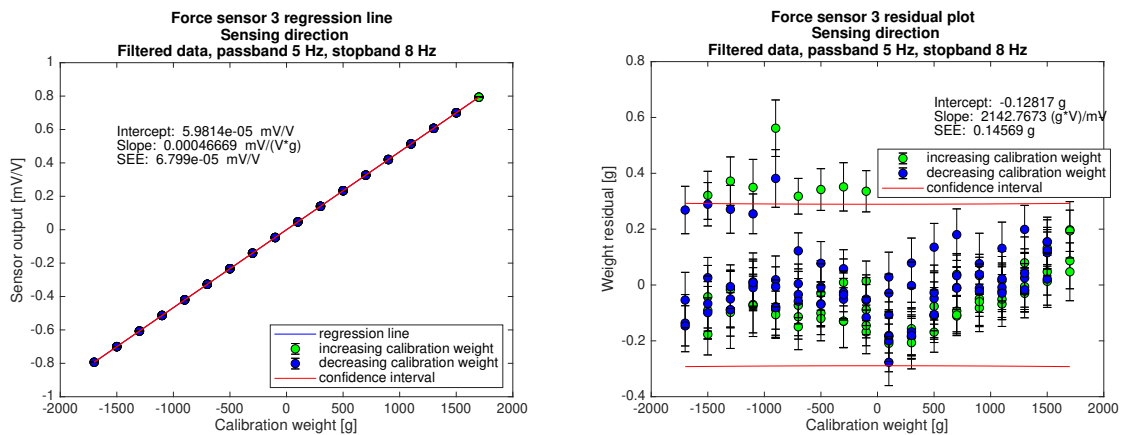
(b) Residual for sensor 2 in L axis



(c) Standard residual for sensor 2 in L axis

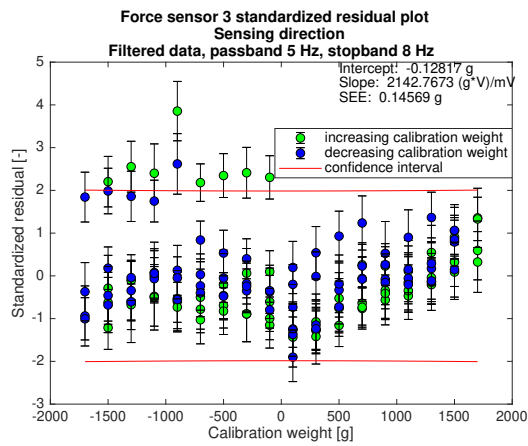
Figure D.6: Sensor regression analysis results, L axis

### D.3. Regression analysis single sensor 3



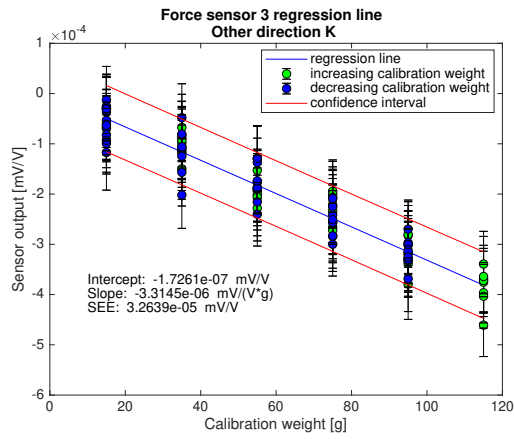
(a) Regression line for sensor 3 in M axis

(b) Residual for sensor 3 in M axis

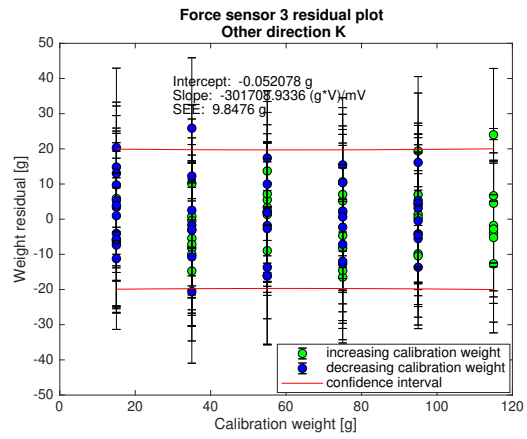


(c) Standard residual for sensor 3 in M axis

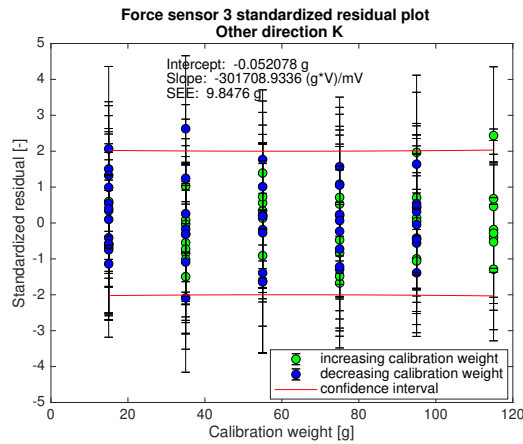
Figure D.7: Sensor regression analysis results, M axis



(a) Regression line for sensor 3 in K axis

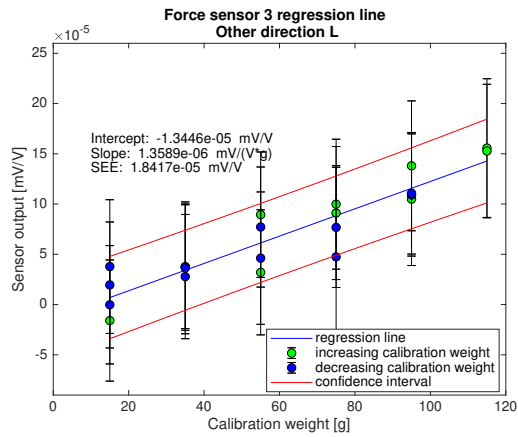


(b) Residual for sensor 3 in K axis

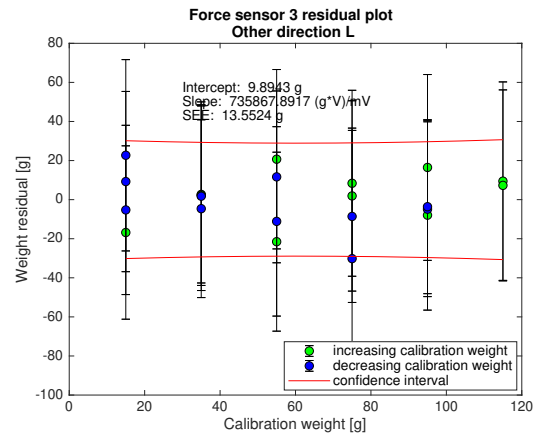


(c) Standard residual for sensor 3 in K axis

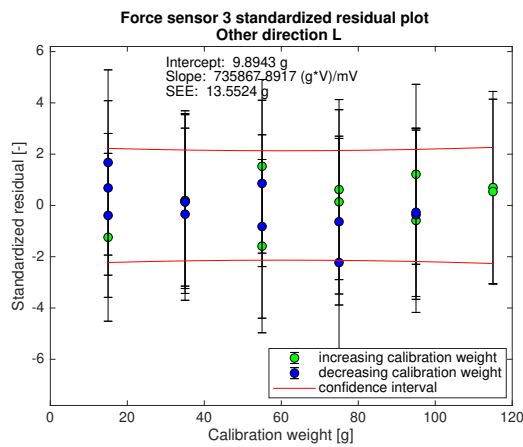
Figure D.8: Sensor regression analysis results, K axis



(a) Regression line for sensor 3 in L axis

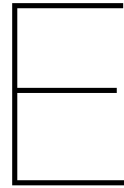


(b) Residual for sensor 3 in L axis

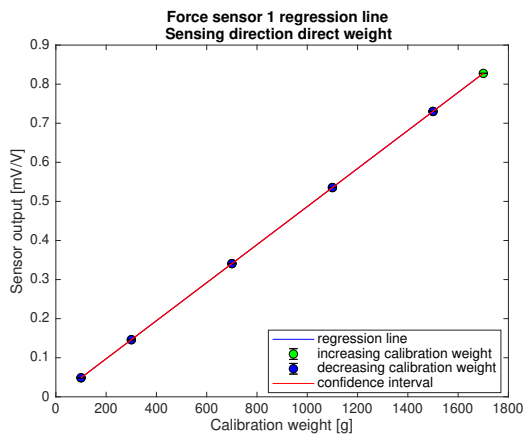


(c) Standard residual for sensor 3 in L axis

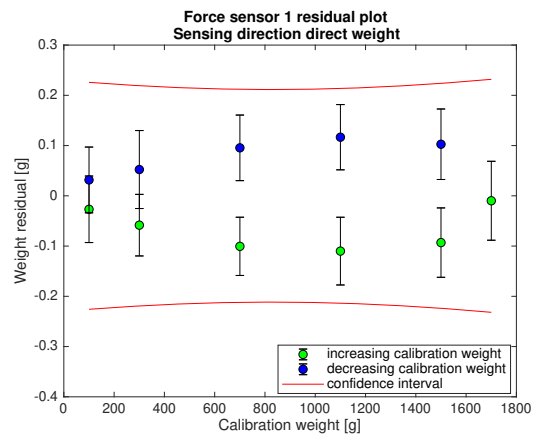
Figure D.9: Sensor regression analysis results, L axis



# Pulley system influence

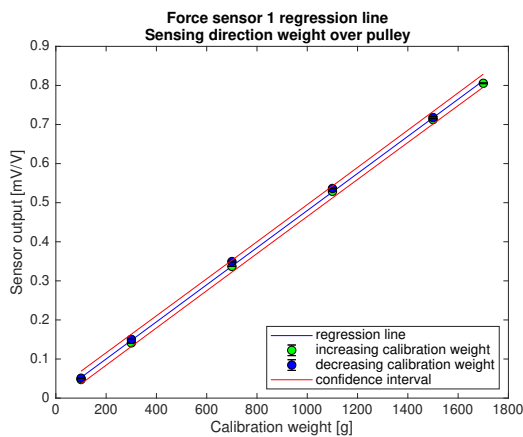


(a) Regression line, direct weight

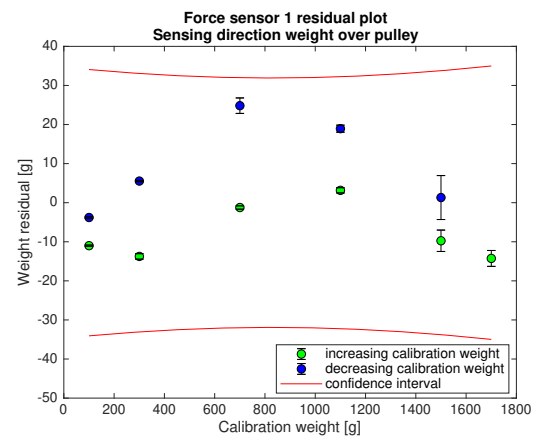


(b) Residual, direct weight

Figure E.1: Regression line and residual plot of direct weight for sensor 1

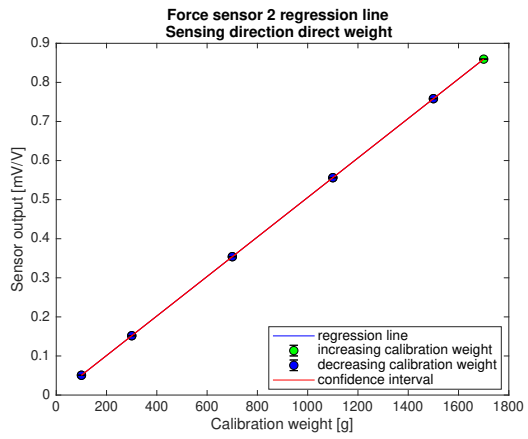


(a) Regression line, weight over pulley

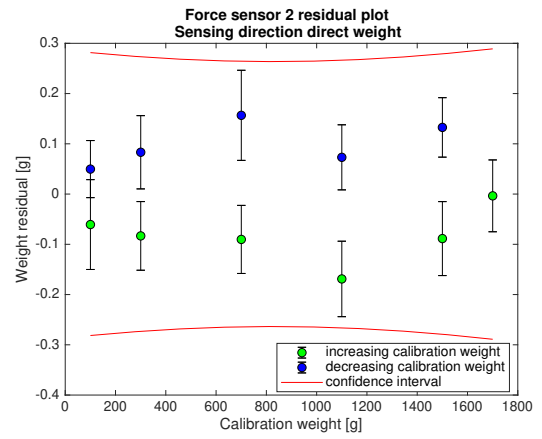


(b) Residual, weight over pulley

Figure E.2: Regression line and residual plot of weight over pulley for sensor 1

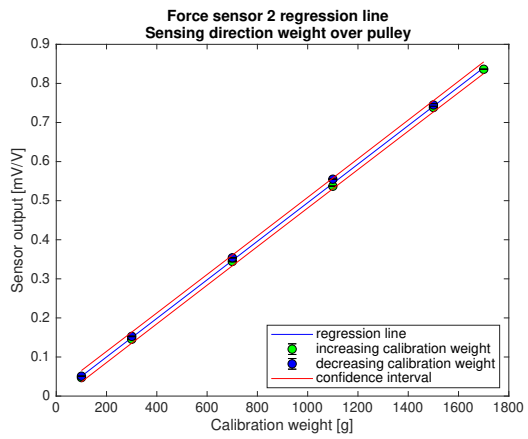


(a) Regression line, direct weight

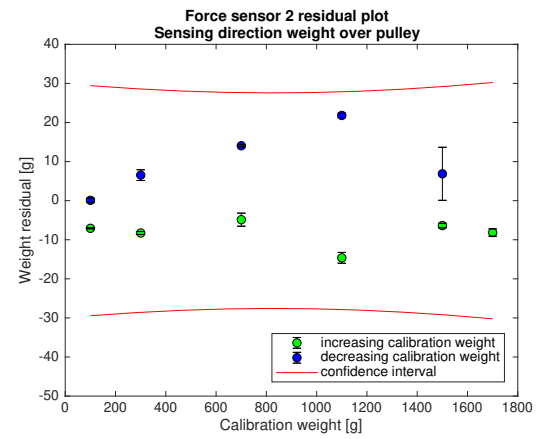


(b) Residual, direct weight

Figure E.3: Regression line and residual plot of direct weight for sensor 2

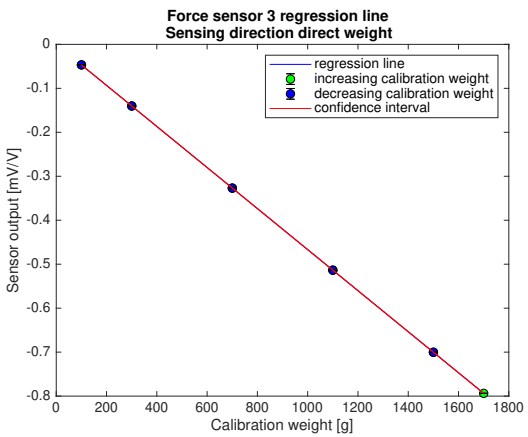


(a) Regression line, weight over pulley

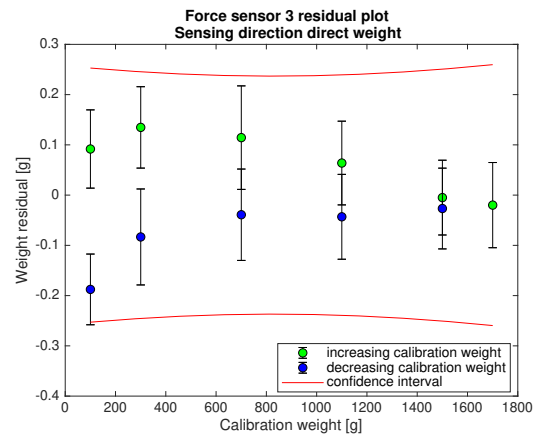


(b) Residual, weight over pulley

Figure E.4: Regression line and residual plot of weight over pulley for sensor 2

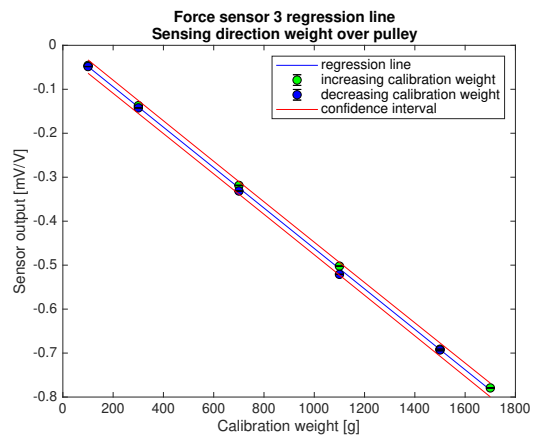


(a) Regression line, direct weight

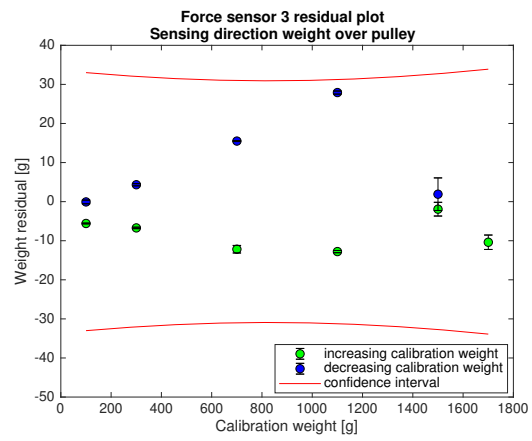


(b) Residual, direct weight

Figure E.5: Regression line and residual plot of direct weight for sensor 3



(a) Regression line, weight over pulley



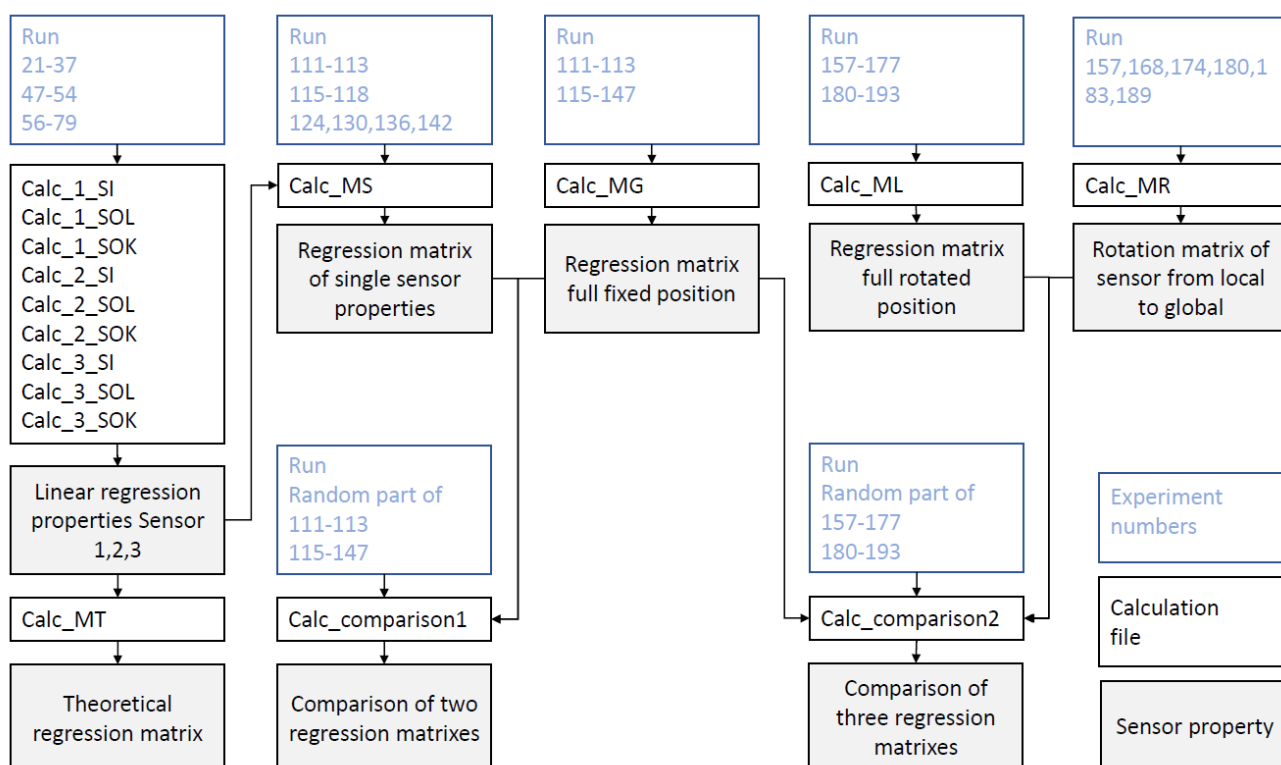
(b) Residual, weight over pulley

Figure E.6: Regression line and residual plot of weight over pulley for sensor 3

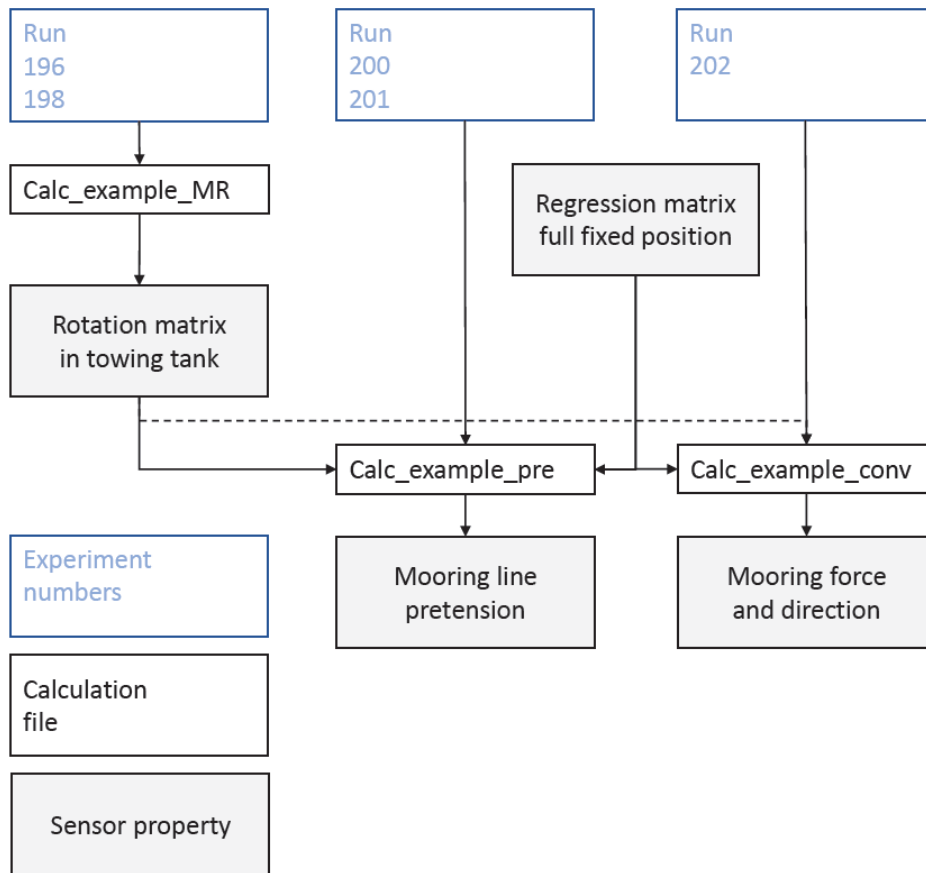
F

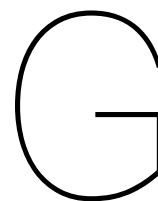
# Calculation flow diagram

## F.1. Calculation flow diagram of calibration experiments



## F.2. Calculation flow diagram of example application experiments





## Data logbook & Calibration scheme

In table G.1, the logbook is shown. For the third column 'Experiment setup' the following abbreviations are used: SI single sensor sensitive direction, SOK single sensor non-sensitive K direction, SOL single sensor non-sensitive L direction, MG sensor frame upright position, ML sensor frame rotated position. The weight order numbers in column six are elaborated in table G.2.

Table G.1: Data logbook

Run	Date	Experiment setup	Sensor	Direction	Weight order number	Additional comments
1	30-jun	SI	3	Negative	(100gr, 300gr, 700gr)	
2	30-jun	SI	3	Negative	(100gr, 300gr, 700gr)	
3	30-jun	SI	3	Positive	(100gr, 300gr, 700gr)	
4	30-jun	SI	3	Positive	(100gr, 300gr, 700gr)	
5	30-jun	SI	1	Positive	(100gr, 300gr, 700gr)	
6	30-jun	SI	1	Negative	(100gr, 300gr, 700gr)	
7	30-jun	SI	2	Positive	(100gr, 300gr, 700gr)	
8	30-jun	SI	2	Negative	(100gr, 300gr, 700gr)	
9	14-jul	MG	1,2,3		(X 259gr)	Use for first approximation of calibration matrix
10	14-jul	MG	1,2,3		(Y 257gr)	Use for first approximation of calibration matrix
11	14-jul	MG	1,2,3		(Z 259gr)	Use for first approximation of calibration matrix
12	14-jul	MG	1,2,3		(X 259gr Y 257gr)	Use for first approximation of calibration matrix, Gewichten apart erop gelegd en eraf
13	14-jul	MG	1,2,3		(X 259gr Z 259gr)	Use for first approximation of calibration matrix
14	14-jul	MG	1,2,3		(Y 257gr Z 259gr)	Use for first approximation of calibration matrix
15	14-jul	MG	1,2,3		(Y 1680gr)	Niet het gewicht eraf gehaald aan het einde

16	14-jul	MG	1,2,3		(X 1680gr)	
17	14-jul	MG	1,2,3		(Z 1680gr)	
18	14-jul	MG	1,2,3		(X 259gr Y 257gr Z 259gr)	
19	14-jul	SOL	3		2	test of out of plane setup
20	15-jul	None	1,2,3			Sensors with only extension plate connected, 1, 2 arrow down, 3 arrow up
21	15-jul	SI	1	Positive	1	Let op hoog frequente trilling- gen vooral halverwege max- imale gewicht
22	15-jul	SI	1	Positive	1	Positive, arrow pointing downward
23	15-jul	SI	1	Positive	1	
24	15-jul	SI	1	Positive	1	
25	15-jul	SI	1	Negative	1	Negative, arrow pointing up- ward
26	15-jul	SI	1	Negative	1	Gekke trilling bij 250 sec
27	15-jul	SI	1	Negative	1	
28	15-jul	SI	1	Negative	1	
29	15-jul	SI	2	Positive	1	
30	15-jul	SI	2	Positive	1	
31	15-jul	SI	2	Positive	1	
32	15-jul	SI	2	Positive	1	
33	15-jul	SI	2	Negative	1	Mislukt
34	15-jul	SI	2	Negative	1	
35	15-jul	SI	2	Negative	1	
36	15-jul	SI	2	Negative	1	
37	15-jul	SI	2	Negative	1	
38	16-jul	None	1,2,3			Sensors with only extension plate connected, 1, 2 arrow down, 3 arrow up
39	16-jul	SI	3	Positive	1	
40	16-jul	SI	3	Positive	1	
41	16-jul	SI	3	Positive	1	
42	16-jul	SI	3	Positive	1	
43	16-jul	SI	3	Negative	1	
44	16-jul	SI	3	Negative	1	
45	16-jul	SI	3	Negative	1	
46	16-jul	SI	3	Negative	1	
47	16-jul	SOL	1		2	
48	16-jul	SOL	1		3	
49	20-jul	SOL	1		2	
50	20-jul	SOL	1		2	
51	20-jul	SOL	1		2	
52	20-jul	SOL	1		2	
53	20-jul	SOL	1		2	
54	20-jul	SOL	1		2	15 als tweede 11 15 12 13 14
55	20-jul	SOL	1		2	Not good
56	20-jul	SOL	1		2	
57	20-jul	SOK	1		2	
58	20-jul	SOK	1		2	
59	20-jul	SOK	1		2	
60	20-jul	SOK	1		2	
61	20-jul	SOK	1		2	
62	20-jul	SOK	1		2	

63	20-jul	SOK	1		2	
64	20-jul	SOK	1		2	
65	20-jul	SOL	3		2	Not much voltage drop
66	20-jul	SOL	3		2	Not much voltage drop
67	20-jul	SOK	3		2	
68	20-jul	SOK	3		2	
69	20-jul	SOK	3		2	
70	20-jul	SOK	3		2	
71	20-jul	SOK	3		2	
72	20-jul	SOK	3		2	
73	20-jul	SOK	3		2	Mislukt
74	20-jul	SOK	3		2	
75	20-jul	SOK	3		2	
76	20-jul	SOL	2		2	
77	20-jul	SOL	2		2	
78	20-jul	SOK	2		2	
79	20-jul	SOK	2		2	
80	21-jul	MG	1,2,3		11	
81	21-jul	MG	1,2,3		14	
82	21-jul	MG	1,2,3		32	
83	21-jul	MG	1,2,3		29	
84	21-jul	ML	1,2,3			Niks aangesloten
85	21-jul	ML	1,2,3			Globale x richting eerst blauw 1 daarna geel 1-5
86	21-jul	ML	1,2,3			Globale z richting eerst blauw 1 daarna geel 1-5
87	21-jul	ML	1,2,3			Mislukt
88	21-jul	ML	1,2,3		7	
89	21-jul	ML	1,2,3			Globale x richting eerst geel 1 daarna blauw 1-5
90	21-jul	ML	1,2,3			Globale x richting eerst geel 1 daarna blauw 1-5
91	21-jul	ML	1,2,3			Globale z richting eerst geel 1 daarna blauw 1-5
92	21-jul	ML	1,2,3		7	
93	21-jul	ML	1,2,3		21	
94	21-jul	ML	1,2,3		28	
95	21-jul	ML	1,2,3		25	
96	28-jul	None	1,2,3			Sensors with only extension plate connected, 1, 2 arrow down, 3 arrow up
97	28-jul	SI (in com- bined frame)	1	Positive	4	Experiment for checking of sensibility of sensor and pul- ley losses, sensor vertical cable directly to weight
98	28-jul	SI (in com- bined frame)	1	Positive	4	Experiment for checking pul- ley losses, sensor horizontal cable over pulley
99	28-jul	SI (in com- bined frame)	2	Positive	4	Experiment for checking pul- ley losses, sensor horizontal cable directly to weight
100	28-jul	SI (in com- bined frame)	3	Negative	4	Experiment for checking pul- ley losses, sensor horizontal cable directly to weight

101	28-jul	SI (in combined frame)	2	Positive	4	Experiment for checking pulley losses, sensor horizontal cable over pulley Experiment for checking pulley losses, sensor horizontal cable over pulley Staaftjes van de sensoren zijn niet strak aangedraaid " " " " " "
102	28-jul	SI (in combined frame)	3	Negative	4	
103	28-jul	MG	1,2,3		(First 1-5 than 6-9 X-dir)	
104	28-jul	MG	1,2,3		(First 1-5 than 6-9 Y-dir)	
105	28-jul	MG	1,2,3		(First 1-5 than 6-9 Z-dir)	
106	28-jul	MG	1,2,3		(First 1-5 than 6-9 X-dir)	
107	28-jul	MG	1,2,3		(First 1-5 than 6-9 Y-dir)	
108	28-jul	MG	1,2,3		(First 1-5 than 6-9 Z-dir)	
109	29-jul	None	1,2,3			
110	30-jul	MG	1,2,3			
111	30-jul	MG	1,2,3		4	x 3x 240 gewichten
112	30-jul	MG	1,2,3		5	
113	30-jul	MG	1,2,3		6	
114	30-jul	MG	1,2,3			
115	30-jul	MG	1,2,3		7	
116	30-jul	MG	1,2,3		8	
117	30-jul	MG	1,2,3		9	
118	30-jul	MG	1,2,3		10	
119	30-jul	MG	1,2,3		11	
120	30-jul	MG	1,2,3		12	
121	30-jul	MG	1,2,3		13	
122	30-jul	MG	1,2,3		14	
123	30-jul	MG	1,2,3		15	
124	30-jul	MG	1,2,3		16	
125	30-jul	MG	1,2,3		17	
126	30-jul	MG	1,2,3		18	
127	30-jul	MG	1,2,3		19	
128	30-jul	MG	1,2,3		20	
129	30-jul	MG	1,2,3		21	
130	30-jul	MG	1,2,3		22	
131	30-jul	MG	1,2,3		23	
132	30-jul	MG	1,2,3		24	
133	30-jul	MG	1,2,3		25	
134	30-jul	MG	1,2,3		26	
135	30-jul	MG	1,2,3		27	
136	30-jul	MG	1,2,3		28	
137	30-jul	MG	1,2,3		29	
138	30-jul	MG	1,2,3		30	
139	30-jul	MG	1,2,3		31	
140	30-jul	MG	1,2,3		32	
141	30-jul	MG	1,2,3		33	
142	30-jul	MG	1,2,3		34	
143	30-jul	MG	1,2,3		35	

144	30-jul	MG	1,2,3	36	
145	30-jul	MG	1,2,3	37	
146	30-jul	MG	1,2,3	38	
147	30-jul	MG	1,2,3	39	
148	30-jul	MG	1,2,3		Sensors in the frame positioned in the global axis system
149	2-aug	MG	1,2,3		Sensors in the frame positioned in the global axis system, Constructions going on at the roof the building, therefore some experiments contain some more disturbance this day
150	2-aug	ML	1,2,3		Sensors with camera bal head but fixed in global axis system
151	2-aug	ML	1,2,3		Sensors with camera bal head fixed in local axis sytem, rotated
152	2-aug	ML	1,2,3	4	
153	2-aug	ML	1,2,3	5	
154	2-aug	ML	1,2,3	6	
155	2-aug	ML	1,2,3	7	
156	3-aug	ML	1,2,3		Mislukt
157	3-aug	ML	1,2,3	4	
158	3-aug	ML	1,2,3	5	
159	3-aug	ML	1,2,3	6	
160	3-aug	ML	1,2,3	7	
161	3-aug	ML	1,2,3	8	
162	3-aug	ML	1,2,3	9	
163	3-aug	ML	1,2,3	11	
164	3-aug	ML	1,2,3	12	
165	3-aug	ML	1,2,3	13	
166	3-aug	ML	1,2,3	14	
167	3-aug	ML	1,2,3	15	
168	3-aug	ML	1,2,3	16	
169	3-aug	ML	1,2,3	17	
170	3-aug	ML	1,2,3	18	
171	3-aug	ML	1,2,3	19	
172	3-aug	ML	1,2,3	20	
173	3-aug	ML	1,2,3	21	
174	3-aug	ML	1,2,3	22	
175	3-aug	ML	1,2,3	23	
176	3-aug	ML	1,2,3	24	
177	3-aug	ML	1,2,3	25	
178	3-aug	ML	1,2,3		Sensors with camera bal head fixed in local axis sytem, rotated
179	4-aug	ML	1,2,3		Sensors with camera bal head fixed in local axis sytem, rotated
180	4-aug	ML	1,2,3	10	
181	4-aug	ML	1,2,3	26	tot een na laatste
182	4-aug	ML	1,2,3	27	tot een na laatste
183	4-aug	ML	1,2,3	28	tot een na laatste

184	4-aug	ML	1,2,3	29	tot een na laatste
185	4-aug	ML	1,2,3	30	tot een na laatste
186	4-aug	ML	1,2,3	31	Tot twee na laatste
187	4-aug	ML	1,2,3	32	tot een na laatste
188	4-aug	ML	1,2,3	33	Tot twee na laatste
189	4-aug	ML	1,2,3	34	Tot twee na laatste
190	4-aug	ML	1,2,3	35	Tot twee na laatste
191	4-aug	ML	1,2,3	36	Tot twee na laatste
192	4-aug	ML	1,2,3	37	Tot drie na laatste
193	4-aug	ML	1,2,3	38	Tot drie na laatste
194	4-aug	ML	1,2,3		Sensors with camera bal head fixed in local axis sytem, rotated
195	5-aug	ML	1,2,3		Sensor in the towing tank, first zero measurement before the sensor is positioned
196	5-aug	ML	1,2,3	(Weight y blue 1,2,3)	Sensor configuration for the global y direction with blue weight 1,2,3 hanging in the water
197	5-aug	ML	1,2,3	(Weight y blue 1,2,3)	Sensor configuration for the global y direction with blue weight 1,2,3 hanging in the water, sleepwagen rijdt dus even wachten met meting
198	5-aug	ML	1,2,3	(Weight z yellow 1,2,3)	Sensor configuration for the z direction with yellow weight 1,2,3 hanging in the water
199	5-aug	ML	1,2,3	(Weight z yellow 1,2,3)	Sensor configuration for the z direction with yellow weight 1,2,3 hanging in the water
200	6-aug	ML	1,2,3		Sensor in the towing tank, zero measurement sensor positioned
201	6-aug	ML	1,2,3		Structure in position, zero measurement
202	6-aug	ML	1,2,3		Structure in position, in wave motions, wave maker file: W01RegWavePSt00p8767sa00p5000VI0085p0575strig0083p0575s, wave sensor file: 83608
203	6-aug	ML	1,2,3		", wave sensor file: 85531
204	6-aug	ML	1,2,3		", wave sensor file: 91755
205	6-aug	ML	1,2,3		", wave sensor file: 94627
206	6-aug	ML	1,2,3		", wave maker file: W01RegWavePSt00p7963sa00p5000VI0092p4337strig0090p4337s, wave sensor file: 101112
207	6-aug	ML	1,2,3		Structure in position, zero measurement
208	6-aug	ML	1,2,3		Sensor in the towing tank, zero measurement sensor positioned

209	6-aug	ML	1,2,3	(Weight y blue 1,2,3)	Sensor configuration for the global y direction with blue weight 1,2,3 hanging in the water
210	6-aug	ML	1,2,3	(Weight y blue 1,2,3)	Sensor configuration for the global y direction with blue weight 1,2,3 hanging in the water
211	6-aug	ML	1,2,3	(Weight z yellow 1,2,3)	Sensor configuration for the z direction with yellow weight 1,2,3 hanging in the water
212	6-aug	ML	1,2,3	(Weight z yellow 1,2,3)	Sensor configuration for the z direction with yellow weight 1,2,3 hanging in the water

In table G.2 the weight order scheme is shown. The weights applied on the sensor in each global direction X, Y or Z are listed. The weight numbers for the X axis are listed table 6.6, Y axis in tables 6.2 and 6.3 and Z axis in 6.7.

Table G.2: Weight order scheme

Weight order number	Weight steps	X axis	Z axis	Y axis or single axis
1	19	-	-	-,1,1-2,1-3,1-4,1-5,1-6,1-7,1-8,1-9,1-8,1-7,1-6,1-5,1-4,1-3,1-2,1,-
2	13	-	-	-,10,10-11,10-12,10-13,10-14,10-15,10-14,10-13,10-12,10-11,10,-
3	7	-	-	-,hook,1,1-2,1,hook,-
4	13	-	-	-,1,1-2,1-4,1-6,1-8,1-9,1-8,1-6,1-4,1-2,1,-
5	13	1	-	-,1,1-2,1-4,1-6,1-8,1-9,1-8,1-6,1-4,1-2,1,-
6	13	2	-	-,1,1-2,1-4,1-6,1-8,1-9,1-8,1-6,1-4,1-2,1,-
7	13	3	-	-,1,1-2,1-4,1-6,1-8,1-9,1-8,1-6,1-4,1-2,1,-
8	13	4	-	-,1,1-2,1-4,1-6,1-8,1-9,1-8,1-6,1-4,1-2,1,-
9	13	5	-	-,1,1-2,1-4,1-6,1-8,1-9,1-8,1-6,1-4,1-2,1,-
10	13	-	1	-,1,1-2,1-4,1-6,1-8,1-9,1-8,1-6,1-4,1-2,1,-
11	13	1	1	-,1,1-2,1-4,1-6,1-8,1-9,1-8,1-6,1-4,1-2,1,-
12	13	2	1	-,1,1-2,1-4,1-6,1-8,1-9,1-8,1-6,1-4,1-2,1,-
13	13	3	1	-,1,1-2,1-4,1-6,1-8,1-9,1-8,1-6,1-4,1-2,1,-
14	13	4	1	-,1,1-2,1-4,1-6,1-8,1-9,1-8,1-6,1-4,1-2,1,-
15	13	5	1	-,1,1-2,1-4,1-6,1-8,1-9,1-8,1-6,1-4,1-2,1,-
16	13	-	2	-,1,1-2,1-4,1-6,1-8,1-9,1-8,1-6,1-4,1-2,1,-
17	13	1	2	-,1,1-2,1-4,1-6,1-8,1-9,1-8,1-6,1-4,1-2,1,-
18	13	2	2	-,1,1-2,1-4,1-6,1-8,1-9,1-8,1-6,1-4,1-2,1,-
19	13	3	2	-,1,1-2,1-4,1-6,1-8,1-9,1-8,1-6,1-4,1-2,1,-
20	13	4	2	-,1,1-2,1-4,1-6,1-8,1-9,1-8,1-6,1-4,1-2,1,-
21	13	5	2	-,1,1-2,1-4,1-6,1-8,1-9,1-8,1-6,1-4,1-2,1,-
22	13	-	3	-,1,1-2,1-4,1-6,1-8,1-9,1-8,1-6,1-4,1-2,1,-
23	13	1	3	-,1,1-2,1-4,1-6,1-8,1-9,1-8,1-6,1-4,1-2,1,-
24	13	2	3	-,1,1-2,1-4,1-6,1-8,1-9,1-8,1-6,1-4,1-2,1,-
25	13	3	3	-,1,1-2,1-4,1-6,1-8,1-9,1-8,1-6,1-4,1-2,1,-
26	13	4	3	-,1,1-2,1-4,1-6,1-8,1-9,1-8,1-6,1-4,1-2,1,-
27	13	5	3	-,1,1-2,1-4,1-6,1-8,1-9,1-8,1-6,1-4,1-2,1,-
28	13	-	4	-,1,1-2,1-4,1-6,1-8,1-9,1-8,1-6,1-4,1-2,1,-
29	13	1	4	-,1,1-2,1-4,1-6,1-8,1-9,1-8,1-6,1-4,1-2,1,-
30	13	2	4	-,1,1-2,1-4,1-6,1-8,1-9,1-8,1-6,1-4,1-2,1,-
31	13	3	4	-,1,1-2,1-4,1-6,1-8,1-9,1-8,1-6,1-4,1-2,1,-
32	13	4	4	-,1,1-2,1-4,1-6,1-8,1-9,1-8,1-6,1-4,1-2,1,-
33	13	5	4	-,1,1-2,1-4,1-6,1-8,1-9,1-8,1-6,1-4,1-2,1,-

---

34	13	-	5	-,1,1-2,1-4,1-6,1-8,1-9,1-8,1-6,1-4,1-2,1,-
35	13	1	5	-,1,1-2,1-4,1-6,1-8,1-9,1-8,1-6,1-4,1-2,1,-
36	13	2	5	-,1,1-2,1-4,1-6,1-8,1-9,1-8,1-6,1-4,1-2,1,-
37	13	3	5	-,1,1-2,1-4,1-6,1-8,1-9,1-8,1-6,1-4,1-2,1,-
38	13	4	5	-,1,1-2,1-4,1-6,1-8,1-9,1-8,1-6,1-4,1-2,1,-
39	13	5	5	-,1,1-2,1-4,1-6,1-8,1-9,1-8,1-6,1-4,1-2,1,-